The Potential of LC-IRMS: Carbon stable isotope analysis of amino acids in a host-parasite system and a proof-of-principle study for $\delta^{15}N$ measurements of nitrate

Dissertation

zur Erlangung des akademischen Grades eines

Doktors der Naturwissenschaften

– Dr. rer. nat. –

vorgelegt von

Tobias Hesse

geboren in Moers

Fakultät für Chemie

der

Universität Duisburg-Essen

2022

Die vorliegende Arbeit wurde im Zeitraum von Januar 2018 bis Dezember 2021 im Arbeitskreis für Instrumentelle Analytische Chemie von Prof. Dr. Torsten C. Schmidt in der Fakultät für Chemie der Universität Duisburg-Essen durchgeführt.

Tag der Disputation: 06.02.2023

Gutachter:	Prof. Dr. Torsten C. Schmidt
	Prof. Dr. Bernd Sures
Vorsitzender:	Jun.-Prof. Dr. J. Voskuhl

DOI: 10.17185/duepublico/78289
URN: urn:nbn:de:hbz:465-20230424-090807-8

Table of contents

Summary

Stable isotope analysis is an established technique and used in scientific branches like geology, meteorology, archaeology, food authenticity and ecology. Different instruments have been developed and although the measurement of stable isotope signatures by LC-IRMS is not the most widely used method, it still bears major advantages over other more common instrumentations and is frequently used for $\delta^{13}C$ analysis of carbohydrates, amino acids and compounds of environmental interest.

This is demonstrated by compound specific isotope analysis of individual amino acids in a controlled feeding/infection experiment using a parasitic cestode (*Schistocephalus solidus*), its second intermediate host (three-spined stickleback, *Gasterosteus aculeatus*) and protein-rich fish diets to advance our understanding of trophic fractionation and nutrient transfer. The system was able to accurately measure the carbon stable isotope signature of thirteen individual amino acids with little sample preparation over an extensive sampling period. While trophic fractionation of amino acids in sticklebacks was low due to isotope routing on high protein diets, it was possible to see different trends in $\delta^{13}C$ values over time in liver and muscle tissue, induced by a subtle carbon isotope shift of dietary sources between sampling days. Biosynthesis of non-essential amino acids in the liver was indicated from very small amounts of dietary lipids and highlight the strength of this technique combined with multivariate data analysis. A similar approach was used to show increased $\Delta\delta^{13}C_{AA}$ values of infected compared to uninfected sticklebacks on the same diet, indicating that the metabolic burden on host organisms induced by parasitic infection is reflected in the carbon isotope signature of amino acids through extensive catabolism, likely to fuel an ongoing immune response and to sustain parasitic growth. Compound specific isotope analysis has been highlighted as a powerful tool to study host-parasite interactions and precise measurements of carbon isotope signatures from small amounts of different sample materials enabled resource allocation in the parasite *S. solidus*, which pointed towards nutrients being assimilated from host liver tissue. The parasite accumulates large amounts of glycogen for maturation, and it was further possible to measure the carbon isotope signature of glucose from parasite tissues with little sample preparation and chromatographic separation. Biosynthesis of parasitic glucose from alanine, asparagine and glutamine was indicated by constant fractionation of -2 to -3 ‰ from enzymatic reactions, while possible conversion of

threonine and serine to glycine for one-carbon metabolism and parasitic growth calls for further research using isotopically enriched materials to get more detailed information and quantify the nutrient transfer.

To advance the field of LC-IRMS and show its potential for future applications, a modified interface for $\delta^{15}N$ analysis of nitrate was developed and tested in a first proof-of-principle study. Reduction of nitrate to measurable N_2 gas was facilitated with $V(III)Cl_3$ and elemental copper using established techniques, while already reported improvements for the LC-IRMS interface were implemented to increase precision and lifetime of the ion source. The system was able to measure $\delta^{15}N$ values from 10 µL injections of nitrate standards and reference materials with a concentration of 50 mgL^{-1} N and with a precision better than 1.4 ‰, while the linearity between $\delta^{15}N$ values was sufficient for measurements on natural abundance levels. The biggest occurring problems were high nitrogen background signals from the mobile phase coupled with isotope shifts and non-linear signal intensities from standards with different concentrations. However, it was already possible to apply this new technique to samples from an isotope enrichment experiment in a small river, where ^{15}N-enriched ammonium chloride was administered over time to isotopically mark the surrounding environment through natural nitrification processes. In contrast to our expectations, no increase in the $\delta^{15}N$ signature of nitrate was measured from downstream water samples during the first two weeks. However, the $\delta^{15}N$ values of unknown nitrogen species eluting early during the injection peak were highly enriched in ^{15}N. This could possibly be attributed to nitrite, although measurement errors due to the early stage of the interface cannot be completely disregarded. Further research and developments are overall necessary, but the system already shows promising results and could not only enable fast and reliable isotope analysis of nitrate for anthropogenic source allocation, but also increase the scope of LC-IRMS in the future by enabling $\delta^{15}N$ analysis of organic compounds.

Zusammenfassung

Die stabile Isotopenanalyse ist eine etablierte Technik und wird häufig in wissenschaftlichen Bereichen wie der Geologie, Meteorologie, Archäologie, Lebensmittelechtheit und Ökologie benutzt. Unterschiedliche Instrumente wurden dazu entwickelt und obwohl die Messung von stabilen Isotopenverhältnissen mittels LC-IRMS nicht die am weitesten verbreitete Methode ist, so hat sie dennoch wesentliche Vorteile gegenüber anderen, verbreiteteren Instrumenten und wird häufig für die $\delta^{13}C$ Analyse von Kohlenhydraten, Aminosäuren und umweltrelevanten Komponenten benutzt.

Dies wird durch die komponentenspezifische Isotopenanalyse von individuellen Aminosäuren in einem kontrollierten Fütterungs- und Infektionsexperiment mit einer parasitären Zestode (*Schistocephalus solidus*), ihrem zweiten vorrübergehenden Wirt (drei-stachliger Stichling, *Gasterosteus aculeatus*) und proteinreicher Fischnahrung demonstriert, um unser Verständnis der trophischen Isotopenfraktionierung und dem Nährstofftransfer zu verbessern. Das System war in der Lage, die stabile Isotopensignatur von Kohlenstoff von insgesamt dreizehn Aminosäuren mit geringer Probenvorbereitung und über einen umfangreichen Probenzeitraum genau zu bestimmen. Obwohl die trophische Fraktionierung der Aminosäuren im Stichling aufgrund von Isotopenrouting bei Nahrung mit hohem Proteinanteil sehr gering ausfiel, war es möglich unterschiedliche zeitliche Trends in den $\delta^{13}C$-Werten in Leber- und Muskelgewebe zu sehen, welche durch geringe Unterschiede der Kohlenstoffisotopensignatur in der Fischnahrung induziert wurden. Die Biosynthese von nicht essenziellen Aminosäuren in der Leber wurde von sehr kleinen Mengen an Lipiden in der Nahrung angedeutet und hebt die Stärke dieser Technik in Kombination mit einer multivariaten Datenanalyse hervor. Ein ähnlicher Ansatz wurde genutzt, um höhere $\Delta\delta^{13}C$ Werte von infizierten im Vergleich zu nicht infizierten Stichlingen auf derselben Diät zu zeigen, was auf eine höhere Belastung des Stoffwechsels von Wirten durch die Infektion mit Parasiten deutet und sich in der Kohlenstoffisotopensignatur der Aminosäuren durch umfangreichen Abbau widerspiegelt, womöglich um eine anhaltende Immunreaktion und das Wachstum des Parasiten zu gewährleisten. Die komponentenspezifische Isotopenanalyse wurde bereits als nützliches Werkzeug zur Untersuchung der Interaktionen zwischen Wirt und Parasit hervorgehoben, und präzise Messungen der Kohlenstoffisotopensignaturen von geringen Mengen an Probenmaterialien ermöglichten es, die Nährstoffquelle des Parasiten

S. solidus innerhalb des Wirtes zu bestimmen. Diese deutete auf die Assimilation von Ressourcen aus dem Lebergewebe des Wirtes oder deren Metabolite hin, und der Parasit ist folglich in der Lage große Mengen an Glykogen anzureichern, welches er für das Heranwachsen benötigt. Die Kohlenstoffisotopensignatur der Glukose konnte zusätzlich mit einer einfachen Probenvorbereitung und chromatografischen Trennung gemessen werden. Glukose im Parasiten könnte in großen Mengen durch Biosynthese aus Alanin, Asparagin und Glutamin produziert werden, da die Kohlenstoffisotopensignatur der Glukose zu diesen Aminosäuren über die Zeit sehr konstant zu -2 bis -3 ‰ niedriger war, was der Idee von enzymatischen Reaktionen entspricht, die häufig gegenüber den schwereren Isotopen diskriminieren. Zusätzlich wurde eine mögliche Umwandlung von Threonin and Serin zu Glycin durch Isotopenfraktionierung sichtbar, was insgesamt zu weiteren Studien mit isotopisch angereicherten Materialien anregt, um mehr detaillierte Informationen zu erhalten und eine Quantifizierung des Nährstofftransfers zwischen Wirt and Parasit zu ermöglichen.

Um das Feld der LC-IRMS zu erweitern, wurde ein modifiziertes Interface zur Analyse von $\delta^{15}N$ Werten aus Nitrat entwickelt und in einer ersten Proof-of-Principle Studie getestet. Die Reduzierung von Nitrat zu messbarem N_2 wurde mit $V(III)Cl_3$ und elementarem Kupfer anhand etablierter Techniken verwirklicht, wobei bereits veröffentlichte Verbesserungen für die LC-IRMS zusätzlich implementiert wurden, um die Präzision und Langlebigkeit der Ionenquelle zu erhöhen. Es war möglich die $\delta^{15}N$ Werte aus 10 µL Injektionen von 50 mgL^{-1} N Nitratstandards und Referenzmaterialien mit einer Präzision besser als 1.4 ‰ zu bestimmen, wobei die Linearität zwischen den $\delta^{15}N$ Werten ausreichend gegeben war, um Messungen mit natürlichen Isotopenverhältnissen zu ermöglichen. Die größten auftretenden Probleme waren hohe Hintergrundwerte an Stickstoff aus der mobilen Phase und nicht-lineare Signalstärken von Standards mit unterschiedlichen Konzentrationen an Nitrat. Trotzdem war es bereits möglich diese neue Technik auf Proben von einem Anreicherungsexperiment anzuwenden, wo ^{15}N-angereichertes Ammoniumchlorid in einen Fluss eingebracht wurde, um die Umgebung durch natürliche Nitrifizierungsprozesse isotopisch zu markieren. Entgegen unserer Erwartung konnte allerdings innerhalb der ersten zwei Wochen kein Anstieg der $\delta^{15}N$ Werte von Nitrat in Wasserproben flussabwärts gemessen werden. Zugleich waren die $\delta^{15}N$ Werte von unbekannten Stickstoffspezies, die früh im Chromatogramm mit dem Injektionspeak eluierten, stark an ^{15}N angereichert. Dies könnte möglicherweise auf

angereichtes Nitrit zurückzuführen sein, wobei Messfehler aufgrund des frühen Entwicklungsstadiums des Interfaces nicht ausschließbar sind. Weitere Experimente und Entwicklungen sind demnach notwendig, wobei das System schon jetzt vielversprechende Ergebnisse liefert und eine schnelle und zuverlässige Isotopenanalyse von Nitrat zur Bestimmung von anthropogenen Quellen ermöglichen kann. Zusätzlich sind weitere Anwendungsmöglichkeiten wie die $\delta^{15}N$ Analyse von organischen Substanzen in Zukunft denkbar, was den Anwendungsbereich der LC-IRMS stark erweitern würde.

Chapter 1: Introduction

Stable isotope analysis (SIA) is a unique tool in analytical chemistry that offers new perspectives on scientific questions. Classical techniques focus on the identification and quantification of compounds, whereas SIA measures the ratio of a heavy to light isotope from a specific element and expresses this ratio in relation to a reference material. Chemical reactions or phase transfer often discriminate against either the heavy or the light isotope, changing the isotope ratio and causing isotopic fractionation. In SIA, differences in the isotopic signature are precisely measured and give insights into the history and origin of a substance or material, which are valuable information in many scientific fields such as meteorology, ecology, doping control, food authenticity, geochemistry, and archaeology [1]. The differences in the isotope signatures observed in nature are very small, e.g., the ratio of $^{13}C/^{12}C$ of biogenic methane ranges between 0.0103 and 0.0106, whereas marine carbonates typically have a $^{13}C/^{12}C$ ratio around 0.0112 [1]. Measuring these small differences is analytically challenging and requires specialized equipment. A core instrument is the isotope ratio mass spectrometer (IRMS), which can be coupled to a variety of interfaces or chromatographic systems, depending on the required technique. Bulk stable isotope analysis (BSIA) measures the isotope signature of whole sample materials such as hair, muscle or plant leaves and is often realized by an elemental analyzer (EA) coupled to an IRMS. The isotope signature of a variety of elements (C, N, S, H, O) are frequently measured in BSIA and the EA-IRMS system is certainly the most commonly used instrument in SIA, offering high precision measurements in a short time period. However, additional information can be gained by measuring the isotope signature of single compounds rather than bulk material, which is therefore labelled compound specific isotope analysis (CSIA) and was first achieved by combining gas chromatography with an IRMS (GC-IRMS) [2, 3] and more recently for liquid chromatography (LC-IRMS) [4, 5]. In both approaches, analytes are separated on a chromatographic column from other sample materials and individually converted to the analyte gas (e.g., CO_2 or N_2) before entering the IRMS. GC-IRMS enables the measurement of carbon, nitrogen, hydrogen and oxygen isotope signatures from individual compounds, whereas LC-IRMS is currently only commercially available for carbon.

1.1 Stable isotope analysis

The term isotope was first coined by Dr Margaret Todd on a dinner party in 1913, where Fredrick Soddy, a student of Ernest Rutherford and future noble prize winner in chemistry, introduced the concept of isotopes. The name comes from the Greek words “isos” and “topos”, which means “in the same place” and accounts for the chemically identical nature of isotopes, which occupy the same place in the periodic table of the elements. The modern definition describes isotopes as nuclei (${}^{N+Z}_{Z}E$) with the same number of protons (Z), but differing numbers of neutrons (N) in their core [6]. Isotopes are therefore of the same element (E) and undergo similar chemical and physical reactions but have different mass numbers (A = N + Z). Isotopes should not be confused with Isobars, which are nuclei with the same mass number A but differing amounts of protons (Z) and are therefore not of the same element. The theoretical number of possible nuclei is huge, with recent estimates going up to 7000 but most of them decay rapidly and are therefore not encountered in nature [7]. The number of stable nuclides amount to 252, distributed over 80 of the 118 known elements. If a nuclide is considered stable depends on whether its half-time ($t_{1/2}$) can be measured or not, which is currently around 10 billion years. The 80 elements with at least one stable isotope are part of the first 82 elements in the periodic table, with the two exceptions technetium and promethium. This shows a common trend where the heavier an element is, the more likely it is to decompose and elements with higher Z or N than ${}^{209}_{83}Bi$ decay spontaneously. The nuclides in molecules can have a variety of different isotopic compositions based on the number of isotope substitutions. Water, e.g., has nine different possible isotope composition, if only the stables isotope of hydrogen and oxygen are accounted for ($^{1}H^{1}H^{16}O$, $^{1}H^{1}H^{17}O$, $^{1}H^{1}H^{18}O$, $^{1}H^{2}H^{16}O$, $^{1}H^{2}H^{17}O$, $^{1}H^{2}H^{18}O$, $^{2}H^{2}H^{16}O$, $^{2}H^{2}H^{17}O$, $^{2}H^{2}H^{18}O$). These molecular entities are called isotopologues and their abundance can be calculated by multiplying the abundance of each isotope and accounting for molecule symmetry of e.g., $^{1}H^{2}H^{16}O$ and $^{2}H^{1}H^{16}O$. Molecules with the same number of isotopes, which only differ in their positions, are called isotopomers and can be further divided into constitutional isomers and isotopic stereoisomers. Important elements in environmental SIA are carbon, nitrogen, oxygen and hydrogen and usually have an isotope ratio which heavily favours the lighter isotope, whereas the heavier isotope is much less abundant (**Table 1.1**). E.g., the isotopic global mean composition for carbon in our environment is 98.89 % ^{12}C and only 1.1 % ^{13}C, but there are small differences based on the origin or the chemical and physical history of the

material. There are various ways to assert the natural abundance of a specified isotope of an element, as it is found in nature. The abundance of isotopes of a specific element (E) with a given mass number (A) from a compound (c) can be expressed as the isotope-amount fraction $x({}^{A}E)_c$ and represents the total number of an isotope $N({}^{A}E)_c$ divided by total number of atoms from that element in a compound $\sum_{i=1}^{k} N(E)_{c_i}$:

$$x({}^{A}E)_c = \frac{N({}^{A}E)_c}{\sum_{i=1}^{k} N({}^{A}E)_{c_i}} \qquad \text{(Eq. 1.1)}$$

The total number of an atom (isotope) $N({}^{A}E)_c$ can be replaced with the amount $n({}^{A}E)_c$ by division with the Avogadro constant N_A and the equation can be reduced for elements with only two isotopes:

$$x_c({}^{h}E) = \frac{n({}^{h}E)_c}{n({}^{l}E)_c + n({}^{h}E)_c} \qquad \text{(Eq. 1.2)}$$

The new superscripts *l* and *h* denote the lighter and heavier isotope, respectively, and the isotope-amount fraction is a dimensionless quantity. Another way to denote isotope abundance of an element in a specific compound is the isotope ratio $R({}^{h}E/{}^{l}E)_c$, which is defined by:

$$R({}^{h}E/{}^{l}E)_c = \frac{N({}^{h}E)_c}{N({}^{l}E)_c} \qquad \text{(Eq. 1.3)}$$

It is common practice to denote the isotope ratio in a way where the heavier and less abundant isotope of an element is given in the denominator and the lighter and more abundant isotope is given in the numerator. The isotope ratio is therefore typically described as the ratio of heavy to light isotope and can be abbreviated to ${}^{h}R_c$. For elements with two stable isotopes, a connection between the isotope-amount fraction and the isotope ratio can be made:

$$x_c({}^{h}E) = \frac{R({}^{h}E/{}^{l}E)_c}{1 + R({}^{h}E/{}^{l}E)_c} \qquad \text{(Eq. 1.4)}$$

Expressing isotope abundance as isotope amount fractions or isotope ratios, however, is not the common way to report data in SIA, as differences can be very small and confusing when digits after several decimals are of interest. Furthermore, the absolute isotope ratio of a compound is hard to measure individually, even with modern equipment. The problem is that isotope measurements need to be very precise to differentiate between isotope signatures on natural abundance level and the instruments used to achieve the

high levels of precision lack the ability to accurately determine the true isotope composition of a sample. In other words, the instrumental trueness is sacrificed in order to achieve the necessary precision for the values to be useful. Isotope data is therefore typically measured and reported against a certified reference material with known exact isotope abundance, which is distributed around laboratories and measured to assign relative isotope ratios of sample materials. To account for this, the δ-scale was introduced by Harold Urey in the late 1940s and used for the first time in a publication in 1950 [8]. On this scale, the relative difference of an isotope ratio $R({}^{h}E/{}^{l}E)_{c}$ of an element in a sample material compared to the isotope ratio of a reference material $R({}^{h}E/{}^{l}E)_{ref}$ is given by:

$$\delta^{h}E_{c,ref} = \frac{R({}^{h}E/{}^{l}E)_{c} - R({}^{h}E/{}^{l}E)_{ref}}{R({}^{h}E/{}^{l}E)_{ref}} = \frac{R({}^{h}E/{}^{l}E)_{c}}{R({}^{h}E/{}^{l}E)_{ref}} - 1 \qquad \text{(Eq. 1.5)}$$

Values on the δ-scale are given in parts per thousand or per mil (‰) and represent the relative difference of the isotope ratio from a sample to a reference material. E.g., a δ^{13}C-value of +23.1 ‰ in a plant material means that the carbon isotope ratio $R({}^{13}C/{}^{12}C)_{plant}$ is 2.31 % higher in comparison to the used reference material $R({}^{13}C/{}^{12}C)_{ref}$. The accepted international reference material for carbon is Vienna Pee Dee Belemnite (VPDB), which is a fossil marine carbonate and has a carbon isotope ratio $R({}^{13}C/{}^{12}C)_{VPDB} = 0.0111802$. The carbon isotope ratio of the plant material can be calculated by rearranging Eq. 1.5 and corresponds to $R({}^{13}C/{}^{12}C)_{plant} = 0.0114385$. Comparing the two ratios shows the small differences that isotope ratios on natural abundance levels can have and demonstrates the usefulness of the δ^{13}C-scale to report and share those data, as long as the same reference materials and scale anchors are used. However, the relationship between the isotope-amount fraction or isotope ratio to the δ-scale is non-linear and can only be approximated as linear on natural abundance levels. Hence, care has to be taken when dealing with isotopically enriched sample materials or hydrogen isotope ratios, since differences in the isotope abundance of these samples or elements are often outside of the approximated linear range of the δ-scale and are therefore better given as isotope-amount fraction or isotope ratios [1].

Table 1.1: List of important nuclides for SIA in environmental sciences.

Element	Atomic Number (Z)	Mass Number (A)	Abundance (%)	Natural variations in isotope amount fraction
H	1	1	99.985	0.999816 – 0.999974
		2	0.015	0.000026 – 0.000184
C	6	12	98.890	0.98853 – 0.99037
		13	1.110	0.00963 – 0 01147
N	7	14	99.634	0.99579 – 0.99654
		15	0.366	0 00346 – 0.00421
O	8	16	99.762	0.99738 – 0.99776
		18	0.200	0.188 – 0.00222

1.2 Isotope fractionation

The average isotope abundance of elements found on earth was set around the time the earth was formed. One could assume that the isotopic composition of an element is therefore identical in different locations and materials found throughout the environments. However, there are small differences in the isotope abundances observed in nature, even in small and localized areas, that originate from mass-sensitive processes causing isotope fractionation, which can be attributed to equilibrium (EIE) and kinetic isotope effects (KIE). EIE are quantum mechanical phenomenon's and originate from vibrational frequencies of molecules and condensed-phases, which are sensitive to isotopic substitution and are explained by concepts of zero-point energy vibrations and partitioning functions. In general, an isotopologues with a heavier isotope vibrates at a lower frequency compared to an isotopologues with a lighter isotope and the energy required to break the bond in an isotopologues with a heavier isotope is higher. Therefore, in an equilibrium reaction, the heavier isotopes tend to accumulate in molecules with stronger bond energies and the magnitude of this isotopic fractionation is roughly proportional to the difference of bond strength between substances [9] and also proportional to the temperature with $1/T^2$. KIE can either stem from molecular or atomic translational velocities or from the sensitivity of activation energies during a reaction to form transition states. The former causes fractionation during diffusion and evaporation and can be modelled using statistical mechanics, the latter is best described with a modification of Urey's equation [10]. Isotopic fractionation is often expressed as an

isotope fractionation factor α by dividing the ratio of heavy to light isotope of an element in compound A by the ratio of heavy to light isotope of an element in compound B:

$$\alpha^{h}E_{A/B} = \frac{R({}^{h}E/{}^{l}E)_{A}}{R({}^{h}E/{}^{l}E)_{B}} \quad \text{(Eq. 1.6)}$$

A subscript of *kin* and *eq* can be used to differentiate between equilibrium and kinetic isotope fractionation factors and the direction of an equilibrium reaction has to be considered, as reversion of the reaction direction would lead to the inverse of the equilibrium fractionation factor $1/\alpha_{eq.}$ A connection between the isotope fractionation factor α and the δ-scale can be made by rearranging Eq. 1.5 and Eq. 1.6:

$$\alpha^{h}E_{A/B} = \frac{\delta^{h}E_{A} + 1}{\delta^{h}E_{B} + 1} \quad \text{(Eq. 1.7)}$$

1.3 Referencing strategies

Stable isotope measurements always have to be referenced on a universal scale and against internationally accepted materials to account for mass-sensitive and discriminating effects in single instruments, so that isotope data is comparable between samples and between different laboratories. A number of international reference materials are available for every element of interest, covering different kinds of sample materials. It is important to differentiate between a scale anchor and a reference material. A scale anchor defines the δ-scale for a certain element so that values of different laboratories or tests are directly comparable if they use the same scale. For carbon, e.g., VPDB and LSVEC are currently used as scale anchors, although the scale is often only named the "VPDB-scale". The original scale defining material was PDB, a belemnite fossil carbonate from the Pee Dee formation, which was used by Harold Urey and Heinz Lowenstam for paleo-thermometric studies [11]. The $\delta^{13}C$ value of PDB is 0 ‰ per definition, as it serves as the scale defining material and origin. The material was exhausted in the early 80s and thus, NBS-19 was introduced as a replacement [12]. NBS-19 is made of a slab of marble, which was crushed, homogenized and indirectly calibrated against PDB with a $\delta^{13}C$ value of +1.95 ‰ [13]. Thus, the origin of the scale remained and the isotope ratio of PDB still is 0 ‰, but the scale anchor was now the new NBS-19 material, and the scale was renamed VPDB. L-SVEC was later introduced as a second anchor with a $\delta^{13}C$ value of -46.6 ‰ on the VPDB scale [14] to increase the accuracy for materials which are significantly depleted in ^{13}C, such as oil. The scale should therefore

be more accurately called the "VPDB-LSVEC scale". Using scale defining materials routinely in the laboratory to reference isotope data of samples is of course not feasible and different reference materials have therefore been developed and are commercially available. These were measured and referenced against the scale defining anchor materials and it is advised to use a reference material of the same or similar kind than the analysed sample material [15]. E.g., if the target analyte is an amino acid such as glutamic acid, it is recommended to also use a reference material made of glutamic acid such as USGS 40 or USGS 41, or at least made of another amino acid. This principle is called identical treatment and aims to minimize instrumental influences such as oxidation efficiencies when dealing with different kinds of materials [15]. For nitrogen, the scale defining material is atmospheric nitrogen (AIR-N_2) and set as 0 ‰ by definition. Atmospheric nitrogen is the largest nitrogen pool on earth and involved in natural source and sink processes. As a consequence, the isotope ratio of atmospheric nitrogen is stable and does not change within levels of measurement uncertainty and it is also not exhaustible. To produce AIR-N_2 as a reference material, CO_2 and water have to be removed by cryogenic trapping and oxygen by reaction with copper oxide. Commonly used reference materials in routine measurements are ammonium and nitrate salts, urea or amino acids such as USGS 40 and 41 [16].

The process to convert measured isotope ratios into δ-values on an international defined scaled is often called normalization and different methods are described. Current IRMS are designed to measure and automatically normalize a sample gas peak to the isotope composition of a working gas in a continuous flow, which was in turn normalised to an international reference material by dual-inlet systems. The software then automatically assigns the normalized δ-value to the sample gas. This approach, however, has two major problems. First, the sample gas and the working gas should have a similar isotope composition, as the introduced error becomes larger when the difference between δ-values of sample and working gas increases. Second, working gases need to be stored in gas cylinders, which can cause isotope fractionation over time for gases with a liquid and gaseous phase, such as CO_2, inside the high-pressured cylinders and especially under temperature variations. A better way to routinely normalize analyte samples is a one-point normalization versus a reference material. Samples and reference materials are measured in close succession by identical treatment. The software of IRMS instruments still requires that every measured sample (or reference material) needs to be measured

against the working gas, which can be manually set to 0 ‰. The measured δ-value of a sample $\delta^h E_c$ can then be mathematically normalized with the measured δ-value of the reference material $\delta^h E_{m-ref}$ vs. the working gas and with the well-known true δ-value of the reference material $\delta^h E_{i-ref}$ to obtain a referenced sample δ-value $\delta^h E_{c,i-ref}$ on an international accepted scale [17, 18]:

$$\delta^h E_{c,i-ref} = \left[\frac{(\delta^h E_c + 1)(\delta^h E_{i-ref} + 1)}{(\delta^h E_{m-ref} + 1)}\right] - 1 \qquad \text{(Eq. 1.8)}$$

The one-point normalization circumvents the problem of isotope fractionation over time in the working gas, but it still suffers from increased uncertainty when measuring sample and reference materials with high differences in their isotope ratios. To compensate for higher differences of δ-values between sample and reference materials, a two-point normalization can be used where two reference materials covering a wide range of δ-values, in which the measured sample value should ideally fall within, are measured. A linear regression between measured and accepted δ-values of the two reference materials is then used to assign a normalized δ-value of a sample material [17, 18]:

$$\delta^h E_{c,i-ref} = \frac{\delta^h E_{i-ref1} - \delta^h E_{i-ref2}}{\delta^h E_{m-ref1} - \delta^h E_{m-ref2}} * (\delta^h E_c - \delta^h E_{m-ref2}) + \delta^h E_{i-ref2} \qquad \text{(Eq. 1.9)}$$

The slope of the regression is called “expansion factor” and should ideally be close to one to ensure that the systematic error within the instrument is linear within the measurement range. The y-intercept is called “additive correction factor” and represents the referenced δ-value of the working gas on the used δ-scale. Two-point normalization increases measurement accuracy compared to one-point normalization and should be used whenever possible.

1.4 Instrumentation

The core instrument of any stable isotope measurement is a specialized mass spectrometer. Measurements need to be done with high precision to resolve variations in isotope ratios on natural abundance levels down to five or six significant decimals, so although systems like quadrupole MS are able to measure isotope ratios, standard deviations achieved by these instruments are too high [19]. The type of mass spectrometer used for isotope analysis can be roughly broken down into three element classes of interest: 1) Light elements like hydrogen, carbon, nitrogen or oxygen are analysed by gas isotope ratio mass spectrometers (GIRMS, or simply IRMS), 2) heavy elements like iron, copper and cadmium are analysed by thermal ionization (TIMS) or inductively coupled plasma mass spectrometers (ICP-MS) and 3) noble gases like neon, argon and xenon are analysed by static vacuum noble gas mass spectrometers. The development of specialized mass spectrometers for isotope ratio measurements is an ongoing field of research, e.g. a unified method for the measurement of noble gases with a dynamic dual-inlet isotope ratio mass spectrometer instead of a static vacuum noble gas mass spectrometer has been recently described [20], and I will subsequently only focus on the instrumentation of IRMS and its peripherals for the analysis of light isotopes.

1.4.1 Isotope ratio mass spectrometry

Highly precise measurements of isotope ratios of light elements are achieved by sector field mass spectrometry in the gas phase and under high vacuum. In short, gas molecules are ionized and accelerated into the electromagnetic field of a mass analyser, where the ionized molecules are diverted from their original path according to their mass to charge ratio and detected in separate faraday cups (**Figure 1.1**) [21].

Since the analysis takes place in the gas phase, analyte samples need to be converted into a measurement gas which should reflect the isotope composition of the original sample material. Typical measurement gases are H_2 for hydrogen, CO_2 for carbon, N_2 for nitrogen and CO for oxygen, but other measurement gases can be utilized, e.g., NO for nitrogen. The conversion of sample materials to the measurement gas can be done either offline or online. Offline conversion of sample materials and subsequent purification is labour intensive, and the measurement gas is introduced into the IRMS via a dual-inlet system, but it also yields the highest precision achievable in IRMS and is frequently used for the measurement of reference materials and standards. Online conversion allows for the automatic conversion of target analytes to the measurement gases in an interface, which

is coupled to the IRMS by an open-split system. The precision achieved by online conversion and the open-split system is not as high as dual-inlet, but it is sufficient to resolve isotope ratios on natural abundance levels, allows for a much faster sample throughput and, most importantly, enables online chromatographic separation to be coupled to IRMS.

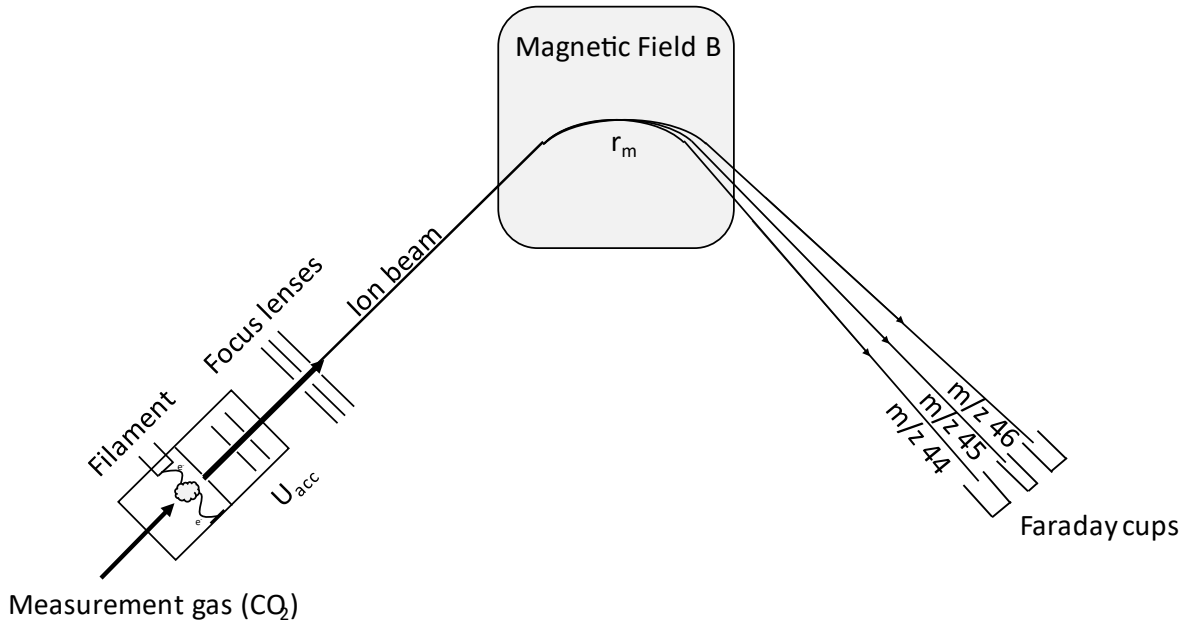

Figure 1.1: Schematic overview over an IRMS system for the measurement of carbon isotope signatures. The measurement gas (CO_2) enters the ion source, where a heated filament emits high energy electrons on a spiral path throughout the ionization chamber. Upon collision, electrons from the measurement gas are ejected and the resulting radical cations are extracted and accelerated through an acceleration voltage U_{acc}. The formed ion beam of m/z 44, 45 and 46 CO_2^+ is focused before it enters the mass analyzer, where a magnetic field B diverts the linear path of the ions according to their m/z ratio. The radial path r_m of CO_2^+ ions containing a heavier isotope is higher compared ions containing light isotopes. The separated ion beams of m/z 44, 45 and 46 are collected separately in individual faraday cups in their focal plane and the signals are amplified and used for the calculation of isotope ratios.

In this approach, the measurement or reference gas is introduced into the ion source of the IRMS in a constant stream of helium carrier gas. The setup involves a small cylindrical glass tube with one sealed and one open end, hence the name open-split. A fused silica capillary emitting a high flow of helium gas is inserted deep into the open split, flushing the whole tube with a constant stream of helium gas and preventing contamination with surrounding air. Note that this helium flow is considered to be a purge gas and not the previously mentioned carrier gas. Two other fused silica capillaries are inserted, one is connected to the high vacuum system of the IRMS and the other carrying the sample or reference gas in a helium carrier gas stream. The fused silica capillary to the IRMS

constantly introduces the helium atmosphere in the open split into the ion source due to the high vacuum it is connected to, and the sample/reference capillary can be operated with a pressure valve to be positioned over the level of the IRMS capillary (IN) or below it (OUT). Due to the flow regime in the open-split, a transient part of any analyte gas that comes from the sample/reference capillary is also introduced into the IRMS if the sample/reference capillary is in the IN position, whereas no analyte gas is introduced if the sample/reference capillary is in the OUT position. This setup allows for the continuous introduction of sample/references gases into the ion source under constant pressure conditions and with little disturbances. Ionization of the measurement gas is achieved by electron impact ionization (EI).

High energy electrons are emitted by a heated tungsten or thorium filament with a high current and forced on a spiralling course throughout the ionization chamber, which is filled with the measurement gas. The spiral course is achieved by two small magnets and improves the collision probability with a gas molecule due to an increased path length before they are either discharged on the wall of the ionization chamber or on an electron trap. If an electron hits a gas molecule, it can expel another electron from the shell if the kinetic energy of the electron is higher than the ionization energy of the gas molecule, forming a radical cation. Due to the high kinetic energy, fragmentation of analyte molecules will also appear to some extent and has to be taken into consideration. Carbon dioxide, e.g., can fragment in an EI source and form carbon monoxide, which has a mass to charge ratio of 28 and can therefore interfere in nitrogen isotope analysis, where the measurement gas is N_2. The formed radical ions are extracted from the ionization chamber, accelerated and focussed into the mass analyser by an electric field. The mass analyser consists of a drift tube with a strong electromagnet attached to the sides. Ions entering the drift tube and the electromagnetic field are diverted by a circular path radius r_m from their original path according to their mass to charge ratio m_{ion}/q_{ion}, the field density B of the electromagnetic field and the applied acceleration current U_{acc}:

$$\frac{m_{ion}}{q_{ion}} = \frac{r_m^2 B^2}{2U_{acc}} \qquad \text{(Eq. 1.10)}$$

The trajectories of isotopes of the same element are therefore different in the mass analyser and can be simultaneously detected by individual faraday cups in their focal plane. The signals are amplified by factors according to their natural abundance levels and recorded for calculation.

1.4.2 Elemental analyzer

Several interfaces have been developed and coupled to IRMS. Their main purpose is to convert sample materials online into the measurement gases of interest, remove matrix components from the carrier gas stream and to either separate the measurement gases if multiple elements should be measured in BSIA, or to preserve chromatographic separation if analytes are separated beforehand in CSIA. The kind of interfaces can be categorized into 1) EA coupled to IRMS for BSIA of e.g., carbon, nitrogen, sulphur, hydrogen or oxygen, 2) GC-IRMS for CSIA of GC amendable compounds for e.g., carbon, nitrogen, oxygen or hydrogen and 3) LC-IRMS for polar compounds and only for carbon isotope analysis.

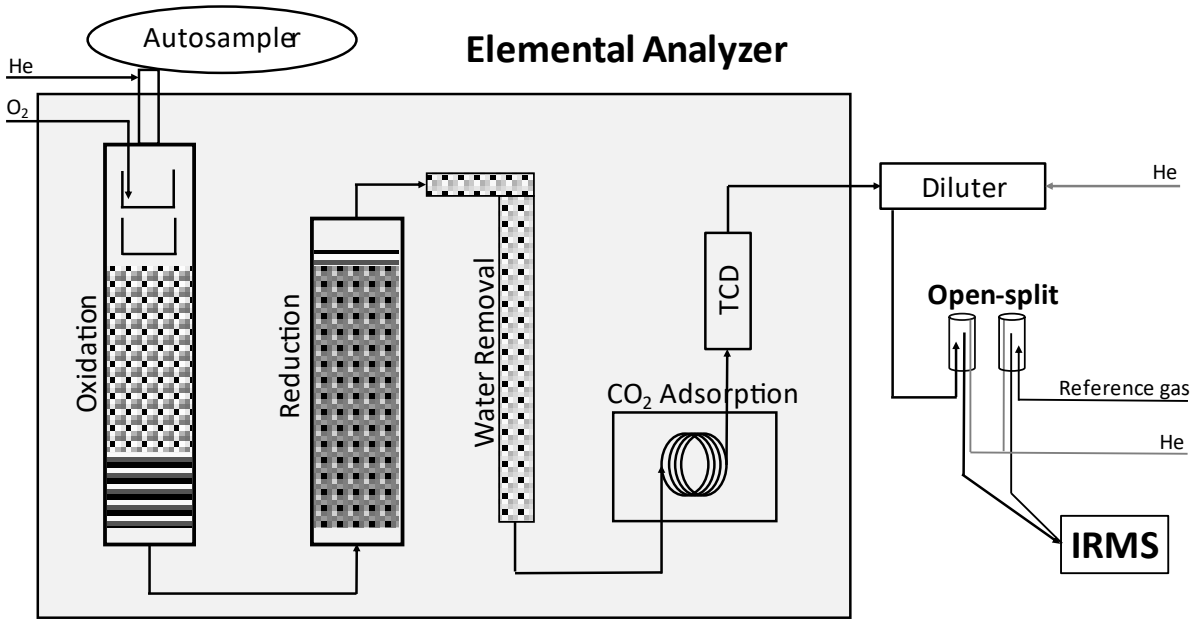

Figure 1.2: Schematic overview over a typical elemental analyzer setup for BSIA of carbon and nitrogen. Homogenized samples are weighed into small tin cups and placed in an autosampler carousel, which drops each individual cup into an ash finger inside the oxidation reactor. Oxidation takes place at 920°C with the help of an oxidation agent (e.g., copper oxide wires), while halogens are removed with silver wool. The analyte gas now consists of CO_2, N_2, NO_x and H_2O in helium carrier gas and is introduced into a reduction reactor at 600°C, where oxygen is removed and NO_x species are converted to N_2 via reduction on elemental copper wires. Residual water from the oxidation of organic material is removed in an L-shaped tube filled with a drying agent (e.g. phosphorus pentoxide P_4O_{10}) and CO_2 and N_2 are separated on a CO_2 adsorption column, which can be rapidly heated up to 110°C to desorb CO_2 after analysis of N_2 is complete. The amount of CO_2 and N_2 are determined with a thermal conductivity detector before they pass a diluter and enter the open split and subsequent IRMS system for isotope analysis.

The coupling of IRMS with an EA for BSIA is certainly the most used type of instrument. Average isotope signatures of complex sample materials like leaves, hair, muscle or other tissues [22-24] are commonly measured to determine carbon, nitrogen, hydrogen, oxygen

or sulphur isotope ratios [21, 25, 26]. Modifications are necessary to measure different elements and **Figure 1.2** depicts a schematic setup for the simultaneous determination of carbon and nitrogen isotope signatures. Samples need to be homogenized and weighed into small tin cups, which are folded tightly to remove residual air. The cups are placed into an autosampler carousel and dropped individually into an ash finger inside the oxidation reactor for catalytic conversion, which is held at 920 °C and flushed with He as carrier gas. Quantitative conversion inside the reactor takes place with the help of an oxidation agent, e.g., copper oxide wires, and the additionally introduction of oxygen directly into the ash finger. The reaction yields a mixture of CO_2, N_2, NO_x species and H_2O, while potential halogens and sulphur are removed by silver wool. The oxidation products are carried over into a reduction reactor, which is heated to 600 °C and filled with elemental copper to reduce NO_x species to elemental nitrogen and remove excess oxygen. To increase precision and avoid isobaric interferences in the ion source, water is removed inside an L-shaped tube filled with a drying agent such as phosphor pentoxide before CO_2 and N_2 are separated on a CO_2 adsorption column.

The separation of the two analyte gases is necessary since the IRMS can only measure the isotope signature of one measurement gas species at a time and needs a couple of seconds to switch between modes. After the analysis of N_2 is complete, the trapped CO_2 on the adsorption column is removed by rapid heating to 110 °C. In addition to the isotope ratios, the system is further able to determine the elemental composition of carbon and nitrogen from the sample material by measuring the amount of CO_2 and N_2 in a thermal conductivity detector (TCD) in relation to the mass of the sample material that was dropped into the oxidation reactor. The amount of CO_2 and N_2 in the gas stream is usually different by a factor of 7:1, as carbon is more abundant in organic samples than nitrogen, but the IRMS works best in a linear range of analyte gas concentrations inside the ion source. Therefore, the gas stream is diluted with additional He during measurements of CO_2 so that both analyte gases enter the ion source in similar amounts and the system parameters can be optimised to this specific concentration range. An open split system introduces the analyte gas into the ion source while also injecting reference gas peaks of either CO_2 or N_2 reference gases during measurements.

1.4.3 LC-Isolink interface

There are two different instruments commercially available to couple HPLC to IRMS for LC-IRMS applications, the LC-Isolink™ Interface from ThermoScientific and the LiquiFace Interface from Elementar. Both employ very similar techniques to convert analytes into measurable CO_2 and I will subsequently focus on the LC-Isolink™ Interface from ThermoScientific for the purpose of this thesis.

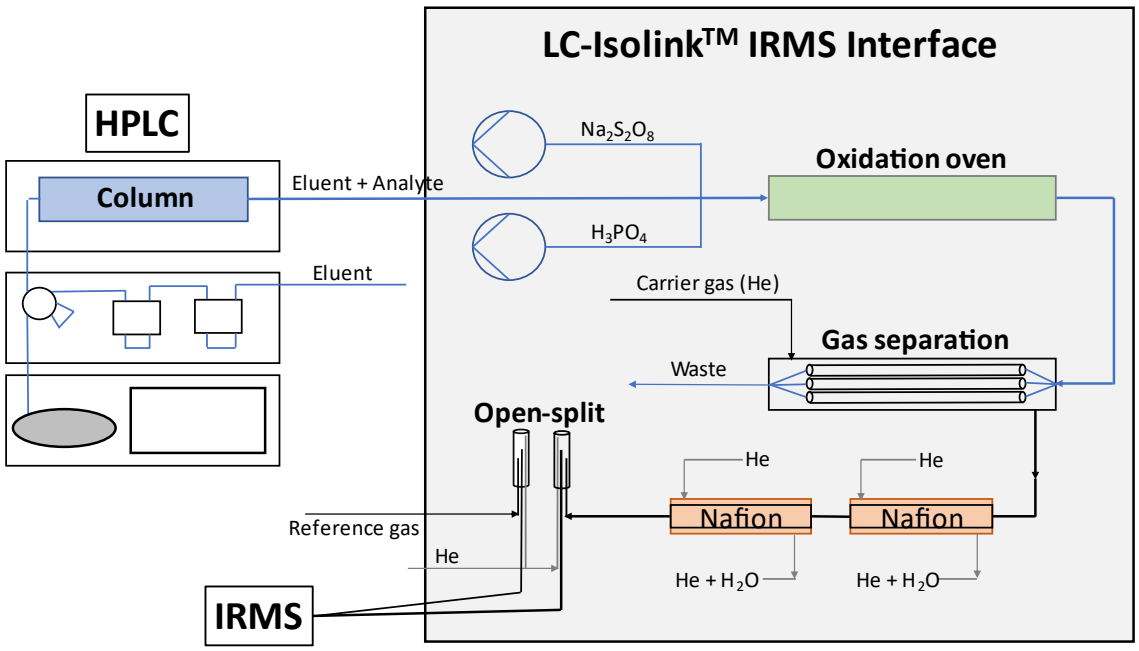

Figure 1.3: Schematic overview over an LC-Isolink IRMS interface, which is used to couple HPLC separation to an IRMS system for compound specific isotope analysis of carbon. After HPLC separation of target analytes, oxidation agents (Na_2S2O_8 and H_3PO_4) are added to the eluent stream. Oxidation and mineralization of organic molecules to CO_2 is facilitated in a heated oxidation oven at 100 °C, followed by extraction of CO_2 into the helium carrier gas flow in the gas separation unit. The carrier gas stream is subsequently dried trough two water permeable NAFION membranes before it enters an open split system connected to the high vacuum of the IRMS.

The LC-Isolink™ IRMS interface allows for the separation of analytes through high performance liquid chromatography (HPLC) and oxidizes the separated analyte molecules online to CO_2 (**Figure 1.3**) [4]. After HPLC, oxidation agents like sodium peroxodisulfate ($Na_2S_2O_8$) and phosphoric acid (H_3PO_4) are added to the mobile phase through a low volume T-piece. Analyte molecules are then oxidized wet chemically with the help of these oxidation agents at elevated temperatures around 100 °C. A small stainless-steel capillary with a volume of ~200 mm^3 is wrapped around a heating block and acts as the oxidation reactor. In the reactor, sulphate radicals are formed from the

added persulfate under acidic conditions, which unselectively oxidize any organic compound in the eluent stream to CO_2.

$$4S_2O_8^{2-} + 2CH_2O + 2H_2O \rightarrow 8SO_4^{2-} + 2CO_2 + 8H^+ \quad \text{(Eq. 1.11)}$$

Although peroxodisulfate anions are strong oxidants with a standard reduction potential of E°=2.01 V, the main oxidative species in this reaction are sulfate radicals. Sulfate radicals are formed when peroxodisulfate anions decompose under e.g., heat or UV light activation and they are highly reactive and electrophilic reagents with a standard reduction potential of E°=2.47 V.

$$S_2O_8^{2-} \xrightarrow{T,UV} 2SO_4^{\cdot -} \quad \text{(Eq. 1.12)}$$

Acidic conditions favour the decomposition of peroxodisulfate anions at elevated temperatures, but recombination of sulfate radicals still occurs and supresses the oxidation reaction [27]. Furthermore, the addition of acids also results in the production of oxygen by protonation of peroxodisulfate anions and subsequent hydrolysis to hydrogen peroxide, which decomposes at high temperatures to water and oxygen. Sulfate radicals, due to their electrophilic nature, remove electrons from organic compounds to form organic radical cations [28], but they also propagate other reactions and in particular form hydroxyl radicals under alkaline conditions [29]. Under acidic conditions, functional groups with electron donating properties, such as amino- or hydroxyl-groups, will stabilize the organic radical cation and increase the reaction rates with sulfate radicals, whereas electron-removing groups such as nitro- or carbonyl-groups will destabilize the radical cation and decrease the reaction rate. Under alkaline conditions, however, the formed hydroxyl radicals preferably add to C=C bonds or abstract hydrogen from C-H, which can be a useful alternative for organic compounds which are hard to oxidize under acidic conditions with persulfate [30]. The residence time of the analytes in the oxidation reactor is higher than 1 min, depending on the flow rate, to facilitate quantitative mineralization of all organic compounds to CO_2 and the eluent is subsequently cooled before it is introduced into a gas separation unit. The flow is split into three separate and very small fused-silica capillaries, each connected to a gas-permeable membrane with a helium stream in counter flow direction. Gaseous species such as CO_2 or O_2, which is also present in large quantities due to the mentioned protonation of peroxodisulfate anions, diffuse through the membrane into the helium carrier gas and are carried through the rest of the system. The gas-permeable membranes further allow some residual water to also enter the gas phase, which is partly removed in

two subsequent gas dryers consisting of water permeable NAFION® membranes, which are again surrounded by a counter flow of helium gas. Nonetheless, the water background is still elevated afterwards, and large quantities of oxygen and water vapour enter the open-split and ion source of the IRMS system along with the measurement gas.

1.5 Applications

The number of SIA studies have been growing in recent years. Especially CSIA has seen a steep increase in publications since the commercialization of GC- and LC-IRMS interfaces. The range of applications are numerous, including food authenticity, forensics, archaeology, doping control, ecology and environmental sciences, but even scientific questions on a much bigger scope, like formation and development of our solar system, are within the reach of SIA [1]. The principle of CSIA often relies on kinetic isotope effects occurring during chemical or biological reactions discriminating against either the heavy or lighter isotope, leading to isotope fractionation. The most prominent example for carbon isotope compositions of organic matter would be the photosynthetic pathways that plants use to fix carbon from carbon dioxide into carbohydrates [31, 32]. Fixing carbon requires diffusion of atmospheric CO_2 into the stomata of plant leaves, which discriminates against the heavier ^{13}C and leads to isotope fractionation between the educt (CO_2) and product (organic carbon). Atmospheric carbon dioxide typically has a $\delta^{13}C$ value of approximately -8.2 ‰ around the globe, but after photosynthesis the $\delta^{13}C$ values of organic plant matter is significantly lower, depending on the kind of photosynthetic pathway the plant is utilizing. Comparing isotope signatures of compounds from different samples can then give insights into the origin and history of a substance or if it was adulterated in any way.

I will subsequently focus on applications which are important for the topic of this thesis, namely compound specific carbon isotope analysis via LC-IRMS, classified by compounds of interests. Note that since many researchers use GC-IRMS, the following applications are not by any means representative of the whole scope of carbon CSIA.

1.5.1 Carbohydrates

A method for measuring carbon isotope signatures of carbohydrates (glucose, fructose and sucrose) was first developed for honey samples[33]. The aim was to differentiate between natural honey samples and those who were adulterated by sugar addition.

Glucose, fructose and sucrose show a strong correlation in their individual $\delta^{13}C$ values in natural honey, with constant differences of $\Delta\delta^{13}C$ values between individual sugars. Limits for $\Delta\delta^{13}C$ values have been established, ranging from 0.0 ± 0.3‰ between fructose and glucose, 1.2 ± 0.4‰ between fructose and sucrose and 1.3 ± 0.4‰ between glucose and fructose. The addition of other sugars (e.g., corn syrup) changes the $\delta^{13}C$ values and results in $\Delta\delta^{13}C$ outside the set ranges, which can be detected down to percentages of 10% adulterants. An improved detection of adulterated honey samples was achieved by sugar and protein compounds with a combination of EA- and LC-IRMS two years later [34]. These methods were recently used to determine the authenticity of pure honey samples of various geographical and botanical origins [35], as well as honey samples originating from Chinese [36] and Lebanese regions [37]. However, it was also shown recently that the previously established limits for $\Delta\delta^{13}C$ values are not always suitable for identification of original honey samples in every region over the world, as 70% of original honey samples collected throughout China could not pass the $\delta^{13}C$-LC-IRMS-test [38]. Adulteration of beverages can also be detected by carbon isotope analysis of carbohydrates via LC-IRMS, as shown by $\delta^{13}C$ values of glucose, fructose, glycerol and ethanol in wine sample [39], organic acids, glucose and fructose in lemon juice [40] and ethanol and glucose in sake [41]. Pre-screening of alcoholic beverages can be done via flow-injection with no chromatographic separation, similar to bulk carbon stable isotope analysis, as a fast and decisive criterion for more sophisticated analysis via CSIA of carbohydrates [42]. Measuring carbon stable isotope signatures of glucose has been further applied to studies of glucose metabolism using isotopically enriched glucose in human plasma samples [43], which was extended shortly after to galactose as another labelled carbohydrate [44]. It was demonstrated that galactose was converted to glucose in the human body during physical exercise and was therefore available for energy metabolism.

1.5.2 Amino acids

The analysis of $\delta^{13}C$ values from individual amino acids is certainly the most used application in LC-IRMS. The first study was already published one year after the commercialization of the instrument in 2005 and used a two-dimensional chromatography to separate 15 underivatized amino acids with a precision of under 0.3‰ [45]. A simpler method was published one year later, employing a mixed-mode chromatography column with cation-exchange and reverse phase interactions and a pH

gradient with 100 % water and 0.2 % sulfuric acid as eluents. Separation was achieved for 15 amino acids and standard deviations of 0.18 ‰ are reported (n = 6). A similar mixed mode chromatography was used in 2009 in conjunction with three mobile phases to separate and measure 14 individual amino acids with an optimal performance between 80 and 660 ng of carbon on column [46]. Although the resolution between individual amino acids was improved, baseline separation of 14 individual amino acids only works if cysteine (Cys) is absent in the samples, which can be problematic for the analysis of hair samples. Otherwise, Cys and methionine (Met) will coelute. Baseline separation of leucine (Leu)and isoleucine (Iso) was not achieved with either method. The analysis of amino acids via LC-IRMS is an ideal alternative to GC-IRMS, since derivatization of amino acids prior to analysis, which usually alters the carbon isotope signatures of target analytes, is not required. A study in 2008 compared the determination of $\delta^{13}C$ values from valine (Val) in complex samples between LC- and GC-IRMS and found that results between both methods were statistically not different on natural and enriched abundance levels [47]. High precision ^{13}C measurements of Val can therefore be done without a derivatisation step. Another study comparing LC- and GC-IRMS for the carbon stable isotope analysis of amino acids was published in 2011 [48]. Although GC-IRMS requires less sample amount, LC-IRMS enables $\delta^{13}C$ measurements of a wider range of amino acids with less analytical error and values closer to those determined individually on an elemental analyzer.

The measurement of $\delta^{13}C$ values of individual amino acids via LC-IRMS has been used in palaeodietary and palaeoecological studies. Raghaven et al. investigated if amino acids from hair protein can be used as a proxy in palaeodietary reconstruction similar to bone collagen, which would validate archaeological CSIA of hair samples [49]. Although a small offset in $\delta^{13}C$ values was observed, they propose that hair samples might be a suitable alternative and complementary source of palaeodietary information in combination with bone collagen, if a constant difference in the carbon isotope signature due to amino acid metabolism and composition is considered. The amino acid carbon isotope signature in different plant tissues was investigated by Lynch et al. and showed that especially leaf and seed protein amino acids have significant differences in their $\delta^{13}C$ values of threonine (Thr), aspartic acid and serine (Ser), which should be considered and utilized in archaeological studies [50]. The resolution of palaeodietary reconstruction through amino acid $\delta^{13}C$ analysis was improved by measuring 0.5 cm segments of hair samples employing the three-phase LC-IRMS method [51]. It was shown that some archaic hunter-

gatherers in the Atacama Desert between 1500 and 4800 years ago relied mostly on aquatic food sources, whereas inhabitants of a nearby valley showed seasonal patterns in their consumption of terrestrial food sources. A follow up study in the same region used amino acid $\delta^{13}C$ analysis of hair keratin and tendon collagen from mummified individuals to increase the temporal resolution in dietary reconstruction, especially throughout the last period of their life [52]. Phe, Val and Leu were used to identify predominantly terrestrial or marine food sources and tendon collagen was used to characterise the final year of the individuals' diet. CSIA of carbon from amino acids can even go beyond questions on region-of-origin or dietary intake and give insights into biometrics. Multivariate analysis shows that there are non-dietary factors like age and body mass index that influence the $\delta^{13}C$ values of individual amino acids [53] and especially Thr showed significantly different $\delta^{13}C$ values in obese subjects compared to other groups. In addition to age and body mass index, sex and alcohol consumption might also be predictable to a certain degree using multivariate analysis of $\delta^{13}C$ values of amino acids [54], but further refinements and larger sampling pools would be necessary.

In addition to dietary reconstruction, LC-IRMS analysis on amino acids has been used in ecological and nutritional studies to investigate amino acid metabolism in diet-consumer relationships. The $\delta^{13}C$ values of rainbow trout's on three different diets were investigated and similar trends for some amino acids are reported [55]. While phenylalanine (Phe) showed very little trophic fractionation overall, arginine (Arg), lysine (Lys), tyrosine (Tyr) and proline (Pro) showed strong depletion in their $\delta^{13}C$ values whereas glycine (Gly), alanine (Ala), asparagine (Asp) and Ser showed the opposite trend of strong isotopic ^{13}C enrichment. Another study on rainbow trout investigated the effect of dietary non-essential and conditionally-essential amino acid composition on the consumer $\delta^{13}C$ values and found strong relationships for Ala, Arg, Gly, histidine (His), Phe and Tyr [56]. Chick blood of four different penguin species were investigated in another study and showed a correlation between $\delta^{13}C$ values of amino acids and the latitude of the penguins foraging locations [57]. Phe was suggested as the most appropriate amino acid to track the isotopic baseline and determine the foraging habitat. A combination of ecology and forensic applications was made by Matos et al., who measured the carbon isotope signature of amino acids from larvae, pupae and adult stages of blowflies raised on different carrion food sources [56]. They were able to correctly classify flies raised on

either raw pork muscle, beef muscle or chicken liver using canonical discriminant analysis of amino acid $\delta^{13}C$ values.

The fractional synthesis rate of glutathione for paediatric studies could be measured after infusion of ^{13}C labelled glycine from 200 µL blood samples, employing a similar method described for the analysis of underivatized amino acids [58]. The observed precision and accuracy were sufficient to calculate synthesis rates of glutathione from its oxidized dimeric form glutathione disulfide and the low sample volume allows for studies even in infants with little sample preparation. The analysis of Gly and glutathione disulfide was initially done separate with two individual methods, but a follow up study managed to measure both analytes in a single run using LC-IRMS [59], opening up a variety of kinetic studies and reducing costs.

1.5.3 Environmental compounds

In environmental applications, a variety of herbicides, organic matters and other compounds could be measured. Herbicides were of special interest because their polarity make them a perfect fit for LC-IRMS. The herbicides bentazone and MCPA were successfully measured with two methods on both GC- and LC-IRMS systems [60], although the LC-IRMS system provided lower standard deviations due to the missing derivatization. Methods for measuring $\delta^{13}C$ values of glyphosate and its metabolite aminomethylphosphonic acid by cation-exchange or reverse phase separation [61] and for desphenylchloridazon, a major degradation product of chloridazon [62], followed and can be used in conjunction with solid-phase extraction to increase sensitivity [63] or, in case of glyphosate and aminomethylphosphonic acid, in natural surface waters and freeze-drying as pre-concentration [64]. Halogenated compounds were investigated via LC-IRMS and showed good oxidation efficiencies for e.g. mono- and dichlorinated compounds, but higher halogenated aliphatics might not be sufficiently oxidized [65]. Halogenated benzoic acids were sufficiently separated from non-halogenated benzoates and the in vivo transformation pathways of these environmental pollutants could therefore be investigated [66]. Employing anion chromatography, Martin et al. developed a method for measuring $\delta^{13}C$ values of polyphosphonates, which are associated with environmental problems such as eutrophication and heavy metal remobilization due to an increasingly industrial use and could distinguish between sorption and degradation processes to a concentration decrease of amino-tris-(methylenephosphonate).

Isotope fractionation during biodegradation and direct photolysis were investigated for the antibiotic sulfamethoxazole and its metabolite 3-amino-5-methylisoxazole [67]. It was possible to differentiate between biotic and abiotic degradation processes due to different carbon isotope enrichment factors of -0.6 ± 0.1 ‰ (biodegradation), -2.0 ± 0.1 ‰ (photolysis at pH 7.4) and -3.0 ± 0.2 ‰ (photolysis at pH 5). Significant isotope fractionation was also detected for the initial steps of microbial degradation of phenol and cresol under aerobic or anoxic conditions, and results suggest that the degradation pathway in the environment can be detected by CSIA [68].

The bulk carbon isotope signature of organic matter in stream and soil waters can be measured by flow injection analysis from aqueous samples of up to 100 µL and a concentration range between 1 – 10 mgL^{-1} C [69]. Samples need to be acidified and purged under vacuum to remove dissolved CO_2 and avoid background interferences. A modified LC-IRMS system was able to measure the amount and $\delta^{13}C$ values of dissolved organic matter with a particle size below 1 µm [70]. Differences in $\delta^{13}C$ values were found for soil solution samples with C3 and C4 vegetations with little sample preparation and high sample throughput. Digestion of calcite with phosphoric acid and removal of dissolved CO_2 under vacuum enables $\delta^{13}C$ analysis of organic matter from speleothem stalagmites [71] as a paleoenvironmental proxy. The combination of inorganic and organic geochemical techniques can then distinguish between soil condition and vegetation parameters through stable carbon isotope records [72]. Classifying dissolved organic carbon in size classes and separation through size exclusion chromatography coupled to LC-IRMS was achieved to determine soil and plant contributions to organic matter in C3 and C4 vegetations [73].

1.5.4 Other compounds

More applications have been published on miscellaneous compounds from different food matrices. The simultaneous determination of glycerol and ethanol from wine samples to differentiate between natural and adulterated wine was demonstrated on 35 Spanish wine samples [74]. The $\delta^{13}C$ values of both analytes were measured in a single run with no isolation of ethanol and glycerol prior to analysis. Extraction of vanillin from chocolate products and determination of $\delta^{13}C$ values was further able to discriminate between natural and synthetic vanillin sources [75]. A similar approach was further able differentiate between corn- and wood-based xylitol from chewing gums[76] and between natural and synthetic caffeine from Chinese tea [77].

1.6 Recent developments

Since the introduction of the LC-IRMS interfaces, methods were developed to analyse compounds which were specifically hard to measure with GC-IRMS systems. These include primarily water soluble and non-volatile substances like sugars, amino acids and alcohols, which are not compatible to GC-IRMS without derivatization, but also substances of environmental interest like glyphosate, AMPA and phosphonates. A study from 2011 [48] compared the determination of $\delta^{13}C$ values from amino acids via LC- and GC-IRMS. They found that LC-IRMS allows for a wider range of amino acid analysis and less analytical error due to the omitted sample derivatization. One could therefore assume that the go-to instrument for amino acid carbon isotope analysis would be the LC-IRMS, but recent studies still favour GC-IRMS. A literature search on Scopus (date: 13.06.2022) with the terms “amino acid”, “LC-IRMS” and “carbon” will lead to 32 found research articles in the time between 2010 and 2022, while doing the same search with the term “GC-IRMS” instead leads to 92 research articles in the same time period. The explanation for this discrepancy might be rather simple: 1) the LC-IRMS system is subject to increased maintenance due to filament lifetime from the introduction of huge oxygen loads into the ion source, 2) chromatographic separation is restricted and allows for less flexibility in the number of compound classes that can be analysed, and 3) the system only allows for the analysis of carbon isotope signatures. In comparison, GC-IRMS requires less maintenance, has a wider range of compounds that can be analysed (although sample preparation is labour intensive) and most importantly, carbon and nitrogen isotope signatures can be determined with the same setup and the system can further be modified to measure hydrogen and oxygen isotope signatures. However, there have been recent developments to mitigate these disadvantages and improve the scope of LC-IRMS. A paper from 2007 [78] introduces first modifications of the interface to increase precision and mitigate maintenance in the ion source. They employ heated copper reactors at 600 °C after the NAFION membranes in the gas phase to remove excess oxygen and prevent oxidation of the filament inside the ion source. This greatly increases the lifetime of the filament and removes the necessity to frequently open the IRMS for maintenance. Since the copper inside the reactor is quickly used up, two reactors are used in parallel, and one reactor is always regenerated with a stream of 3 vol% hydrogen in helium while the other is in use. An additional water trap with a dry-ice acetone slush further eliminates excess water from the gas flow, which stems from the gas separation unit and cannot completely be removed by the two following NAFION membranes. This decreases isobaric

interferences from protonated analyte molecules in the ion source and increases the precision of the instrument. Another study from 2018 introduces position specific $\delta^{13}C$ analysis of amino acid carboxylic groups [79]. The oxidation agents in this approach are replaced with ninhydrin to release CO_2 from carboxylic groups, adding another dimension to the characterisation of amino acids. Standard deviations below ±0.1 ‰ are reported and this method promises to enable more refined studies on carbon cycling and metabolism, which was demonstrated one year later in a follow up study on mammalian keratin samples [80]. Recently, a coupling of LC-IRMS to high resolution mass spectrometry (HRMS) has been achieved, enabling the simultaneous analysis of carbon isotope ratios while at the same time allowing for structural analysis of compounds or identification of unknown or coeluting species [81]. The coupling was realized with an online post-column splitter, and the applicability was demonstrated by confirming contamination of the USGS41 (and also to a smaller amount USGS41a) reference materials with pyroglutamic acid.

The afore mentioned improvements and modifications demonstrate that, despite the initially commercialized interface bears many shortcomings, there are still ways to enhance the scope and applicability of the instrument. A very recent review highlights the limitations and applications , but also states that there are critical issues that need to be addressed in order to give new perspectives to the field or stable isotope analysis [82].

Chapter 2: Aims and scope

CSIA gained a lot of momentum during the last decade due to instrumental advances. Most studies in this area employ a GC-IRMS instrument because it can be used to analyse the isotope ratios of different elements and from a broad spectrum of analytes. CSIA by LC-IRMS has more limitations regarding the amenable elements and a more challenging chromatographic separation and is therefore less frequently used. The aim of this work is outlined into two sections (**Figure 2.1**). First, the usefulness of CSIA via LC-IRMS to investigate ecological and metabolic questions is demonstrated. Despite its shortcomings, the use of LC-IRMS can be advantageous for analytes such as amino acids and carbohydrates, which are not available for GC-IRMS systems without derivatization if the element of interest is only carbon. Second, a modified interface for the measurement of stable nitrogen isotope signatures from nitrate is developed and tested to advance the field of LC-IRMS, which could be used for fast and reliable tracking of nitrogen sources in surface waters. This is done in a first proof-of-principle study and an isotope enrichment experiment and could serve as a first step to enable nitrogen isotope analysis of organic compounds via LC-IRMS.

In chapter 3, the carbon isotope signatures of individual amino acids were measured to gain insights into fractionation and nutrient transfer between diets and consumer in a controlled feeding experiment. Advantages of CSIA compared to classical BSIA were shown by calculating trophic fractionation of individual compounds and comparing NEAAs and EAAs because of their different metabolic classification. The simplified sample preparation and measurement of amino acids via LC-IRMS compared to GC-IRMS should be advantageous for prolonged and accurate measurements over extensive time periods. Measuring individual AAs further allows for multivariate data analysis, which can be used to show common trends or even small differences in isotope signatures and fractionation between NEAAs and EAAs. A lot of research in this area is still field-based and few studies were conducted under controlled feeding conditions to enhance our fundamental understanding of isotope fractionation. Chapter 4 shows that CSIA via LC-IRMS is not only a powerful technique to investigate common predator-prey relationships but is also especially useful in complex host-parasite systems. Parasites are recognized as important parts of our ecosystem and were often neglected because they are difficult to observe and small in size. The high amounts of glucose in the parasite makes LC-IRMS an ideal technique to study host-parasite interactions by CSIA of carbohydrates in addition to

amino acids. Small amounts of different samples were measured from host muscle, liver and parasite tissues to study nutrient conversion and sources, which was done for the first time by CSIA of carbon.

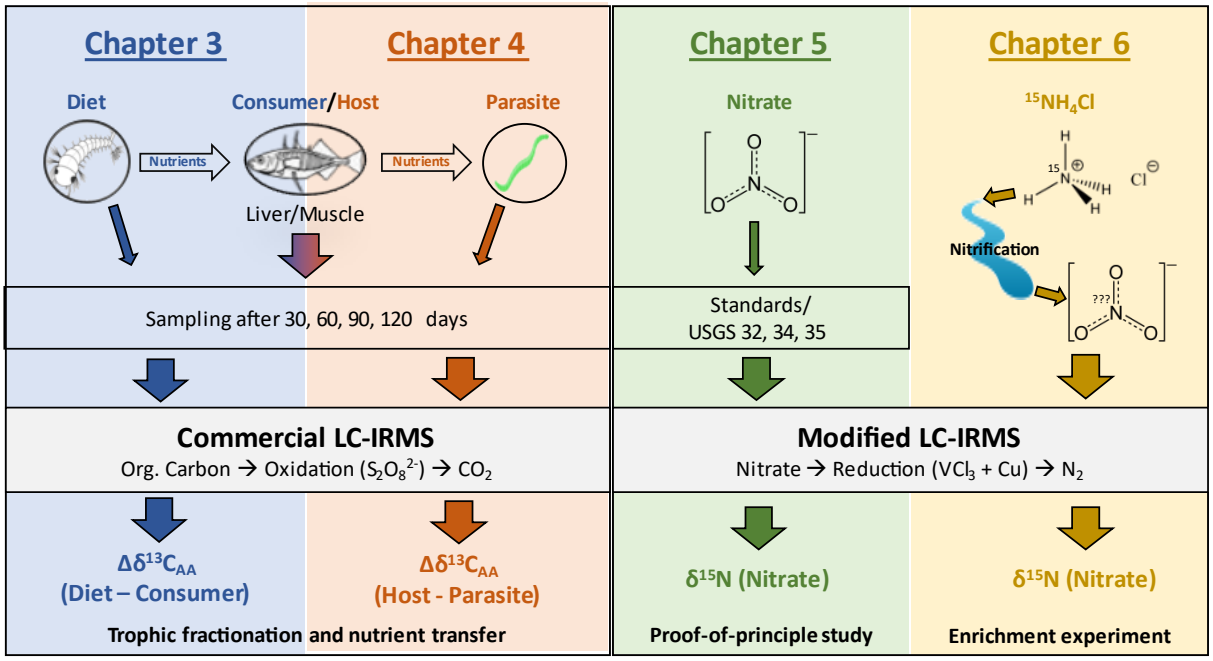

Figure 2.1: Graphical illustration of the work presented in this thesis. Chapter 3 and 4 will demonstrate the usefulness of CSIA via LC-IRMS by measuring carbon isotope signatures of amino acids in a diet-consumer and host-parasite system. Samples were drawn from a controlled feeding experiment over the course of 120 days, with the aim to investigate trophic fractionation and nutrient transfer in complex predator-prey relationships. Chapter 5 presents first results from a modified interface to enable stable nitrogen isotope analysis of nitrate in a proof-of-principle approach. Chapter 6 uses the modified interface to measure real samples from an isotope enrichment experiment, where ^{15}N-labeled ammonium chloride was introduced into a small lake.

In chapter 5, a modified interface was developed and tested in a proof-of-principle concept for the measurement of nitrogen isotope signatures of nitrate from water samples. The limitation of LC-IRMS applications to only carbon stable isotopes analysis is probably the most significant drawback of the system to date, and it seems natural to expand the horizon of amenable elements to make the system a more attractive option for isotope analysis. In addition, already reported improvements for the interface will be incorporated to increase precision and longevity. First results are presented for standards and reference materials, while emerging problems are identified with possible solutions and optimization. Chapter 6 uses the modified interface to measure real water samples taken from an isotope enrichment experiment, where ^{15}N-labelled ammonium chloride was introduced into a small river and samples were taken on a weekly basis. Natural nitrification processes by microbes should convert the ^{15}N-enriched ammonium into

nitrate, which would lead to significantly increased $\delta^{15}N$ values of nitrate downstream from the administration point. The design of the experiment by using isotopically enriched materials is an ideal proving ground for the new interface since the precision of measurements might not be as high compared to the analysis of carbon isotope signatures and also not sufficient in this early state for studies on natural abundance levels.

The modified interface not only advances the scope of LC-IRMS, but also could be considered as a steppingstone towards a new interface for nitrogen isotope measurements of organic compounds. The analysis of carbon and nitrogen isotope signatures from individual compounds like amino acids is often combined in many research fields and currently only possible by GC-IRMS. Enabling nitrogen isotope analysis of polar compounds in addition to carbon without derivatization will further expand the applications of isotope analysis in general and close the gap between LC- and GC-IRMS.

Chapter 3: Insights into amino acid fractionation and incorporation by compound-specific carbon isotope analysis of three-spined sticklebacks

Authors:

Tobias Hesse[1], Milen Nachev[2,3], Shaista Khaliq[1], Maik A. Jochmann*[,1,3], Frederik Franke[4,6], Jörn P. Scharsack[4,5], Joachim Kurtz[4], Bernd Sures[2,3], Torsten C. Schmidt[1,3]

Affiliations:

1. Instrumental Analytical Chemistry, University of Duisburg-Essen, Universitätsstr. 5, 45141 Essen, Germany
2. Aquatic Ecology, University of Duisburg-Essen, Universitätsstr. 5, 45141 Essen, Germany
3. Centre for Water and Environmental Research, University of Duisburg-Essen, Universitätsstr. 5, 45141 Essen, Germany
4. Institute for Evolution & Biodiversity, University of Münster, Hüfferstr. 1, 48149 Münster, Germany
5. Present address: Thünen Institute of Fisheries Ecology, Herwigstr. 31, 27572 Bremerhaven, Germany
6. Present address: Bavarian State Institute of Forestry, Hans-Carl-von-Carlowitz-Platz 1, 85354 Freising, Germany

Adapted with permission from: T. Hesse, M. Nachev, S. Khaliq, M. A. Jochmann, F. Franke, J. P. Scharsack, J. Kurtz, B. Sures, T. C. Schmidt, *Insights into amino acid fractionation and incorporation by compound-specific carbon isotope analysis of three-spined sticklebacks, Scientific Reports, 2022, 12 (1)*, DOI 10.1038/s41598-022-15704-7

3.1 Abstract

Interpretation of stable isotope data is of upmost importance in ecology to build sound models for the study of animal diets, migration patterns and physiology. However, our understanding of stable isotope fractionation and incorporation into consumer tissues is still limited. We therefore measured the $\delta^{13}C$ values of individual amino acids over time from muscle and liver tissue of three-spined sticklebacks (*Gasterosteus aculeatus*) on a high protein diet. The $\delta^{13}C$ values of amino acids in the liver quickly responded to small shifts of under ±2.0 ‰ in dietary stable isotope compositions on 30-day intervals. We found on average no trophic fractionation in pooled essential (muscle, liver) and non-essential (muscle) amino acids. Negative $\Delta\delta^{13}C$ values of -0.7 ± 1.3 ‰ were observed for pooled non-essential (liver) amino acids and might indicate biosynthesis from small amounts of dietary lipids. Trophic fractionation of individual amino acids is reported and discussed, including unusual $\Delta\delta^{13}C$ values of over +4.9 ± 1.4 ‰ for histidine. Arginine and lysine showed the lowest trophic fractionation on individual sampling days and might be useful proxies for dietary sources on short time scales. We suggest further investigations using isotopically enriched materials to facilitate the correct interpretation of ecological field data.

3.2 Introduction

Stable isotope analysis (SIA) of carbon is a powerful tool in ecological studies to investigate resource utilization, foraging behavior and migration patterns of animals [83-85]. The underlying principle is that the carbon stable isotope composition ($\delta^{13}C$) of diets is mostly retained by consumers, with only small amounts of trophic fractionation occurring during incorporation and metabolism of nutrients. In bulk stable isotope analysis (BSIA), trophic fractionation therefore only increases the $\delta^{13}C$ values of consumers by 0 – 1 ‰ [86, 87] and the carbon stable isotope signature of an individual is mostly depending on the isotope composition of primary producers. This enables tracking of nutrients from the base of food webs to higher trophic level predators. However, there can be deviations from this pattern depending on species, analyzed tissue and diet composition [88, 89]. A more recent approach, compound specific stable isotope analysis (CSIA), was enabled by analyzing individual compounds rather than bulk tissues. Where BSIA of carbon typically shows little fractionation between diet and consumer, individual constituents such as amino acids (AA) can have higher fractionation, depending on which compounds they are routed from and the nutrient composition of diets [85, 90-94].

AAs can be divided into essential amino acids (EAA) and non-essential amino acids (NEAA, **Table 3.1**). EAAs cannot be synthesized by higher organisms and therefore need to be taken up directly from dietary sources, leading to no or very little trophic fractionation as they are traversing the food chain mostly unchanged from primary producers to top predators [85, 95-97]. NEAAs on the other hand can be synthesized *de novo* in higher organisms and therefore originate either from dietary protein and/or other macronutrients, such as lipids and carbohydrates. Whether these compounds are directly routed or synthesized *de novo* is depending on dietary nutrient composition, e.g. consumers fed with high protein contents tend to also directly incorporate NEAAs in order to preserve energy [93, 95, 98, 99], whereas biosynthesis of NEAAs from lipids leads to lower $\delta^{13}C$ values because lipids are depleted in ^{13}C compared to proteins or carbohydrates [100, 101]. However, the classification of AAs into essential and non-essential is not always clear, as nutrient requirements of some NEAAs, e.g. glutamic acid (Glx) and proline (Pro), can outmatch an organism's ability to synthesize these compounds, rendering them temporarily or conditionally essential [102]. Another special case would be tyrosine (Tyr), which can be synthesized *de novo* in higher organisms but

is directly derived from phenylalanine (Phe), which is an EAA. The carbon isotope signature of Tyr therefore typically falls into the same range as Phe [94], although it should be considered non-essential.

Table 3.1: Classification of analyzed AAs in fish. Abbreviations are given in brackets. Adapted from Falco et al. (2020) [103].

	Glucogenic	**Glucogenic/Ketogenic**	**Ketogenic**
Essential	Arginine (Arg) Histidine (His) Threonine (Thr)	Phenylalanine (Phe)	Lysine (Lys)
Nonessential	Alanine (Ala) Asparagine/Aspartate (Asx) Glutamine/Glutamate (Glx) Glycine (Gly) Proline (Pro) Serine (Ser)	Tyrosine (Tyr)	

One shortcoming of most ecological studies using stable isotopes is that they typically only consider whole body or muscle tissue [104], as these are easy to access. The turnover and incorporation rate in muscle tissue is rather low and more affected by consumer physiology and growth phases during which protein synthesis and deposition occurs [105, 106]. The stable isotope signature of muscle tissue therefore reflects the long-term dietary intake and remains conservative towards small or only seasonal changes in dietary $\delta^{13}C$ values. The liver, on the other hand, responds more quickly to small or seasonal dietary changes, as its regulatory activities require continuous protein turnover [105-109]. In addition, the liver plays an important role in the metabolism and biosynthesis of AAs [102, 110, 111], which makes it an ideal tissue for studying these processes. Another shortcoming of most studies using stable isotopes is that they are field based, hence there was an initial call for more laboratory studies in 1997 [112] to understand the fundamental principles of isotopic incorporation, trophic discrimination and isotope routing. Although the number of laboratory-based studies has increased since then, the call was renewed in 2009 [113] to facilitate correct interpretation of field data. Few controlled feeding experiments so far examined the carbon isotope fractionation of individual AAs between diet and fish consumers, with varying magnitudes and directions

of trophic fractionation reported [92-95, 99]. McMahon et al. (2010) found ^{13}C-depleted isotope signatures of Gly between Common Mummichogs (*Fundulus heteroclitus*) and one of their diets, whereas Rogers et al. (2019) found significantly ^{13}C-enriched Gly stable isotope signatures of Chinook Salmon (*Oncorhynchus tshawytscha*) reared on the same diet. This example demonstrates that clear differences in individual AA trophic fractionations can occur among fish species.

The three-spined stickleback (*Gasterosteus aculeatus*) is a well-studied model fish in ecology, evolutionary biology, and parasitology [114, 115], yet no carbon stable isotope analysis of AAs has been done to this date. The only studies reported so far are field-based and using BSIA to investigate sex, armor, phenotypes, genetics, and host-parasite relationships [116-119]. We conducted a laboratory-based feeding experiment, where three-spined sticklebacks were reared on a protein rich diet with low amounts of lipids (60 % protein, 5 % lipids) over the course of four months. To contribute to our understanding of isotope incorporation, discrimination, and routing, we measured the carbon isotope signature of individual AAs from muscle, liver and dietary samples taken on 30-day intervals by Liquid Chromatography Isotope Ratio Mass Spectrometry (LC-IRMS). Previous BSIA of dietary samples (data not published) revealed a minor carbon isotope shift from -15.8 ‰ after 30 days to -17.0 ‰ after 60 days, -18.1 ‰ after 90 days and -16.9 ‰ after 120 days, which is likely transferred to fish tissue to varying degrees depending on tissue type. Based on our current knowledge of isotope incorporation, fractionation, and the high protein contents in fish diets, we expect that both EAA and NEAA in muscle and liver tissue of sticklebacks will be mainly routed from dietary sources and therefore show little trophic fractionation. Furthermore, if the dietary stable isotope shift over time from BSIA is also measurable using CSIA of individual AAs, we expect that the high protein turnover of liver tissue will also result in a significant isotope shift between sampling days in contrast to muscle tissue. Lastly, the small amounts of other macronutrients than dietary protein might not be enough to result in significantly different $\delta^{13}C$ values between liver and dietary samples but using multivariate analysis might indicate patterns of fractionation due to biosynthesis or metabolism of NEAAs. This is the first time that carbon isotope signatures of AAs were measured for three-spined sticklebacks on a time series and in a controlled feeding experiment. Our goals were to investigate $\delta^{13}C$ values of AAs from liver and muscle tissue, especially in response to changing dietary $\delta^{13}C$ values over time and to find differences in $\delta^{13}C$ patterns between

tissues. Furthermore, we expect that NEAAs and EAAs will show similar and small trophic fractionation in $\Delta\delta^{13}C$ values in general, since fish are fed on high protein contents. Our results will therefore help to validate common assumptions in CSIA-AA, but also show limitations and new possibilities in ecology to interpret the carbon stable isotope signatures of AAs from different tissue types and time intervals.

3.3 Results

3.3.1 AA $\delta^{13}C$ changes between sampling days

One-way ANOVA for each AA with sampling days as independent variable and $\delta^{13}C$ values as dependent variable of dietary samples revealed a significant isotope shift over time for all AAs except His (DF = 3, 8; $p < 0.01$; **Table 3.3**). A trend can be seen where the carbon stable isotope signature of each dietary AA decreased between 30 and 60 days as well as 60 and 90 days, followed by an increase in $\delta^{13}C$ values between 90 and 120 days (**Figure 3.4**), although the shift was not always significant between consecutive sampling days (30 – 60, 60 – 90, 90 – 120 days). The highest differences between -2.4 and -4.2 ‰ were observed between 30 and 90 days. Isotope signatures of AAs in the liver were significantly different over time for Ala ($F_{3,8} = 6.8$, $p = 0.004$), Asx ($F_{3,8} = 9.2$, $p = 0.001$), Arg ($F_{3,8} = 13.7$, $p < 0.001$), Lys ($F_{3,8} = 18.4$, $p < 0.001$), Phe ($F_{3,8} = 8.9$, $p = 0.001$) and Tyr ($F_{3,8} = 20.8$, $p < 0.001$). Most of these differences were also observed between 30 and 90 days, with the addition of Glx between those specific sampling days and decreasing $\delta^{13}C$ values between -2.1 and -3.0 ‰. Although not all AAs in the liver revealed a significant isotope shift, the trend of decreasing $\delta^{13}C$ values from 30 to 60 days and from 60 to 90 days followed by an increase from 90 to 120 days was still comparable to dietary samples. No significant differences between sampling days were observed for muscle tissue for any AA.

3.3.2 Trophic fractionation of NEAAs, EAAs and individual AAs among liver and muscle

We investigated trophic fractionation between NEAAs and EAAs over the complete sampling period. Two-way ANOVA on $\Delta\delta^{13}C$ values of pooled NEAAs and EAAs (NEAA/EAAs and tissue as fixed factor, **Table 3.5**) revealed no significant difference in trophic fractionation between NEAAs and EAAs ($F_{1, 435} = 5.6$, $p = 0.019$, $\alpha = 0.01$) among all samples, but there was a significant interaction between factors ($F_{1, 435} = 9.4$, $p = 0.002$). The interaction was caused by negative $\Delta\delta^{13}C$ values of -0.7 ± 1.3 ‰ for NEAAs in liver tissue compared to $\Delta\delta^{13}C$ values of -0.1 ± 1.1 ‰, 0.0 ± 1.4 ‰ and 0.0 ± 1.1 ‰ for EAAs in

liver and both NEAAs and EAAs in muscle, respectively, resulting in significant differences in trophic fractionation around ±0.7 – 0.8 ‰ between those samples (Tukey-tests, **Table 3.4**). Differences in trophic fractionation between EAAs in the liver and NEAAs and EAAs in muscle were not observed.

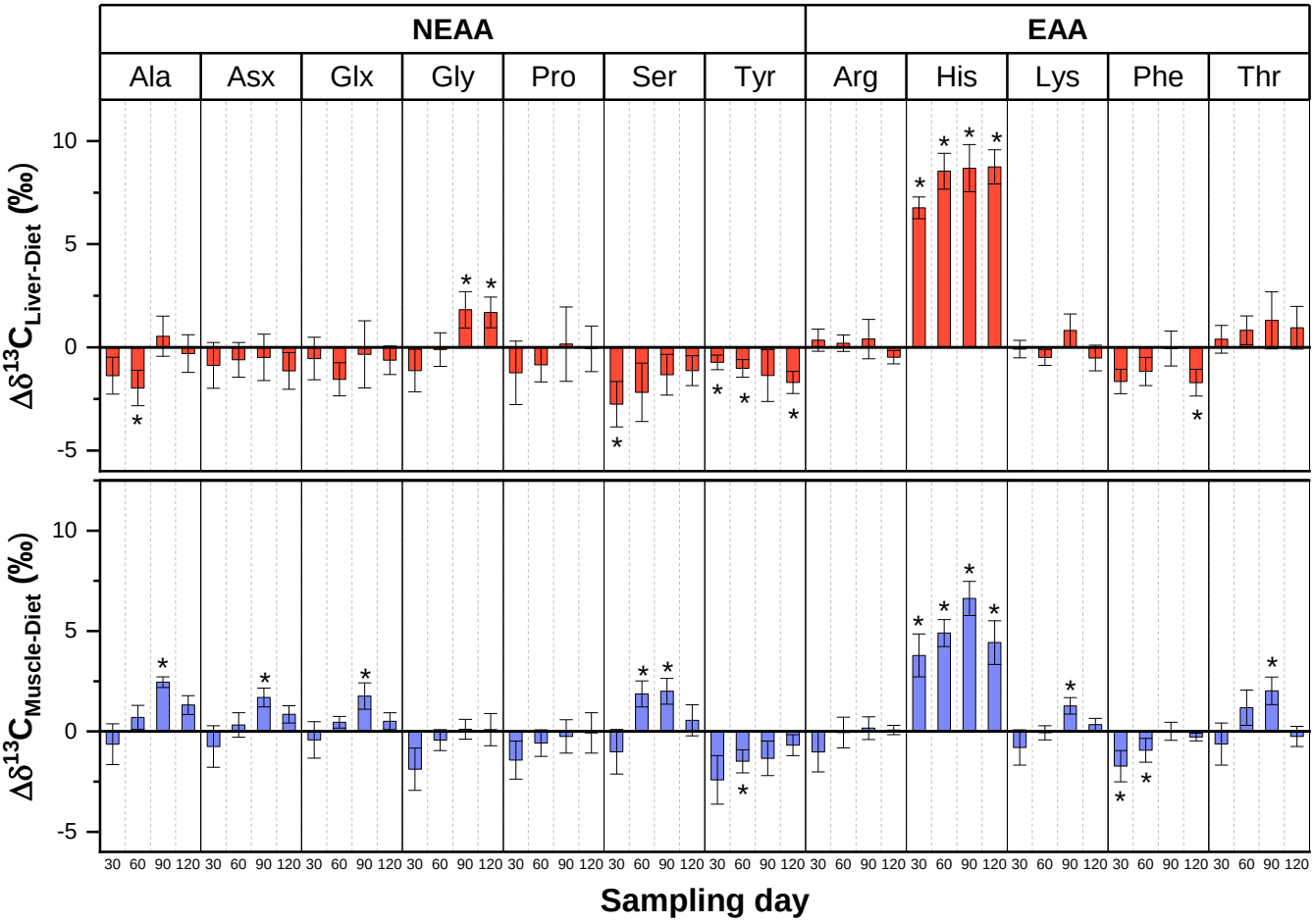

Figure 3.1: Carbon stable isotope signatures of AAs show low trophic fractionation between fish liver/muscle and dietary samples except for His. Trophic fractionation between stickleback and dietary samples was estimated by calculating Δδ13C values ± SD (error bars, n = 5) for liver ( ) and muscle ( ) samples. Asterisks over Δδ13C values indicate significant differences from two-sided t-tests against 0 ($p < 0.01$, Table S3). Δδ13C values are generally below ± 2‰ for all AAs in muscle and liver samples except for His. The frequently significant Δδ13C values in muscle samples on day 90 are caused by the low protein turnover and therefore minor decrease of δ13C values in muscle samples compared to the significant δ13C decrease in dietary samples. Arg and Lys have the lowest trophic fractionation overall.

$\Delta\delta^{13}C$ values of individual AAs between fish tissues and diets were calculated over the complete sampling period and on each sampling day (**Figure 3.1**). Significant differences were tested with two-sided t-tests for each value (N = 20 for the complete sampling period, N = 5 on each sampling day) and with a confidence level of 0.01. Significant negative $\Delta\delta^{13}C$ values over the complete sampling period were measured for Asx (-0.8 ±

1.0 ‰), Glx (-0.8 ± 1.1 ‰), Ser (-1.8 ± 1.2 ‰), Tyr (-1.2 ± 0.8 ‰) and Phe (-1.1 ± 0.9 ‰) in liver tissue and for Tyr (-1.5 ± 1.0 ‰) and Phe (-0.7 ± 0.9 ‰) in muscle tissue, whereas positive $\Delta\delta^{13}C$ values were measured for Ala in muscle (1.0 ± 1.3 ‰), Thr in liver (0.9 ± 1.0 ‰) and His in both tissues (8.2 ± 1.2 ‰ and 4.9 ± 1.4 ‰, respectively). In some of the mentioned cases, average $\Delta\delta^{13}C$ values are lower than the measured SD, but due to the larger sampling size (N = 20 over the complete sampling period) the resulting p-values were still below the significance level of 0.01.

The highest $\Delta\delta^{13}C$ values on individual sampling days in liver tissue were measured for His (6.8 ± 0.5 ‰ on day 30, 8.5 ± 0.9 ‰ on day 60, 8.7 ± 1.1 ‰ on day 90 and 8.7 ± 0.8 ‰ on day 120), for Gly on day 90 (1.8 ± 0.9 ‰) and day 120 (1.7 ± 0.7 ‰) and for both Tyr (-0.7 ± 0.4 ‰ on day 30, -1.0 ± 0.4 ‰ on day 60 and -1.7 ± 0.5 ‰ on day 120) and Phe (-1.7 ± 0.6 ‰ on both day 30 and 120). Significant $\Delta\delta^{13}C$ values were measured in muscle tissue on day 90 for Ala (2.5 ± 0.3 ‰), Asx (1.7 ± 0.5 ‰), Glx (1.8 ± 0.7 ‰), Ser (2.0 ± 0.6 ‰), His (6.6 ± 0.9 ‰), Lys (1.3 ± 0.4 ‰) and Thr (2.0 ± 0.7 ‰). Pro, Arg and Lys had the smallest average $\Delta\delta^{13}C$ values in both muscle and liver tissue around ± 0.1 to 0.2 ‰ (Arg, Lys) and around -0.5 ‰ (Pro). Except for Lys in muscle on day 90, no significant fractionation on individual sampling days were measured for those three AAs. The most significant isotope fractionation was observed for His between diet and both liver and muscle. Since peak areas of His were low compared to the earlier and closely eluding Lys (**Figure 3.3**), we tested different background algorithms (individual, dynamic and manual) in the Isodat 2.0 software to check if the differences between His $\delta^{13}C$ values could be explained by interferences and coelution of the more abundant Lys. Regardless of the used peak integration and background detection procedure, a strong isotope fractionation of His between dietary and liver/muscle was always observed.

3.3.3 Patterns of AA $\delta^{13}C$ values among tissues

Since differences in $\delta^{13}C$ values between fish and dietary samples might be low in response to the used high protein diets, we performed ANOVA simultaneous component analysis (ASCA) to investigate patterns of AA $\delta^{13}C$ values in a multivariate approach. Sample scores of liver tissue were separated from muscle and dietary samples on the first principal component of factor 1 (Tissue, **Figure 3.2**), which contributed 22.4 % to the total variance. NEAAs were the main driver of separation with loadings above 0.3 for Ala, Asx, Glx and Ser, whereas Gly was the only NEAA with a negative loading of below -0.2 (**Figure 3.2**). Ser had the overall highest loading of 0.7 on PC1. All EAAs and Pro had

loadings of below ± 0.2 and therefore little to no effect on PC1 separation. Individual scorings of liver samples were negative on PC1, whereas muscle and dietary samples had almost exclusively positive scorings. PC2 showed slight separation between fish tissue and diets and was mostly loaded with the EAAs Phe, Thr as well as the NEAAs Pro and Tyr **(Figure 3.2**).

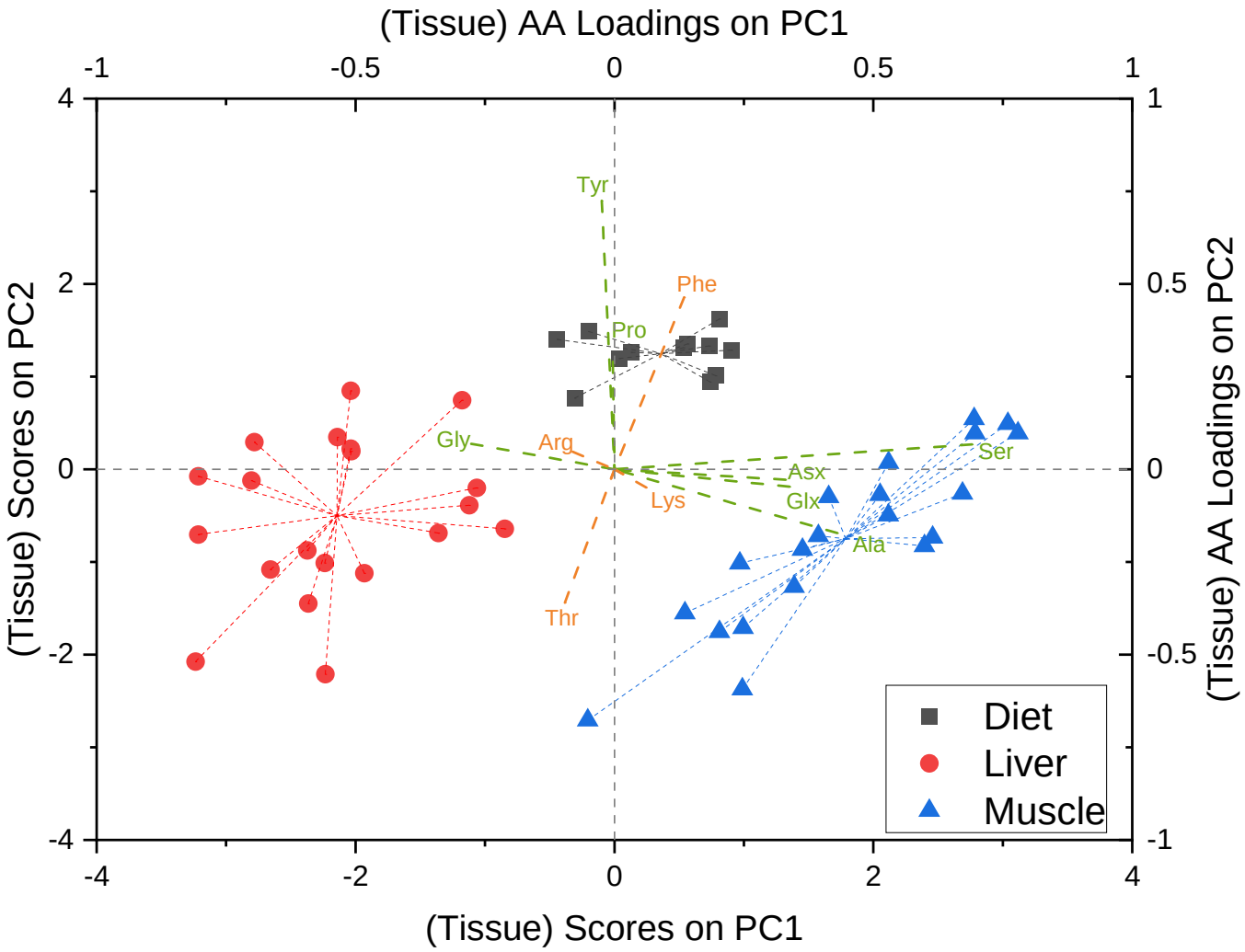

Figure 3.2: Multivariate analysis of δ13C values shows distinct δ13C patterns of NEAAs in liver samples compared to dietary and muscle samples. Biplot of sample scores from ASCA for factor 1 (tissue) separates between liver (●) and muscle (▲) or dietary (■) samples on PC1. Scores of liver samples on PC1 are negative in contrast to positive scores of muscle samples or scores around 0 for dietary samples. NEAA loadings (▬) on PC1 are positive for Ala, Ser, Asx and Glx and negative for Gly, whereas EAAs (▬) and Pro have no impact on PC1. AA loadings on PC2 are positive for Pro, Phe and Tyr and negative for Thr.

Arg and Lys were the only AAs which had no impact on separation between tissues for both PCs. Factor 2 (sampling days) of the ANOVA simultaneous component analysis had an effect of 35.5 % on system variance and PC1 accounted for 93.5 % of variance on factor 2. AA loadings on PC1 were exclusively positive between 0.15 and 0.4. Sample scores

centered around 4 for samples taken after 30 days, 0 for samples after 60 days, -3 for samples after 90 days and -1 for samples after 120 days, but clear separation of samples was not achieved in a score plot.

3.4 Discussion

The cause for the stable isotope shifts of dietary AAs over time in our study remains unknown, but the observed trend of all AAs having a similar shift over time indicates that different batch materials of mosquito larvae might have been used throughout the experiment. The change of $\delta^{13}C$ values in muscle tissue between any given sampling day was within -1.8 and +1.2 ‰, but these shifts were statistically not significant and overshadowed by natural variations between individuals. This supports the idea that AAs from muscle tissue are a more conservative indicator of long-term dietary intake in fish, similar to what was previously described for BSIA [105, 106]. Liver tissue, on the other hand, showed significant isotopic differences over time, indicating that the high nutrient turnover rate of the liver is reflected in its AA carbon stable isotope signature and even short-term changes are visible. The range of $\delta^{13}C$ values in the liver was between -3.3 and +1.4 ‰ and EAAs showed the most significant differences (one-way ANOVA, $p \leq 0.001$), which indicates high turnover for these compounds because they must be rooted from dietary sources. Only Ala and Asx showed significant differences over time from NEAAs in liver tissue. Both AAs are important energy substrates in fish and precursors for gluconeogenesis [120], which is the metabolic pathway in the liver to synthesize glucose from other carbon substrates. Fish therefore have a high Ala and Asx demand in liver tissue, which might outmatch the fish's ability to sufficiently synthesize these compounds and lead to an increased incorporation or turnover from dietary sources. According to our results, liver carbon isotope signatures of Ala, Asx, Arg and Lys might be useful proxies to track consumer diets of small teleost fish on protein rich diets and on time scales of at least 30-day intervals. This information could possibly be expanded to non-protein rich diets for Arg and Lys, due to the necessity of eukaryotes to directly incorporate these nutrients from dietary source, regardless of their composition [95]. The change in liver $\delta^{13}C$ values were most notable between samples from day 30 and 90 and not consistently between consecutive sampling days, which can be attributed to the rather small changes in dietary $\delta^{13}C$ values of only ±1 to 2 ‰ between sampling days, which are also partly overshadowed by natural variations and measurement uncertainties. The isotopic half-life of muscle and organ tissue from ectotherms can be estimated according to their body

mass [121]. The average body mass of sticklebacks on sampling days was 1.28 ± 0.35 g (N = 20), which would translate to a half-life of approximately 27 days for muscle and 12 days for liver tissue. This estimation supports the observed significant change of $\delta^{13}C$ values over time in liver samples and the only slightly decreasing $\delta^{13}C$ in muscle tissue. The differences in dietary AA $\delta^{13}C$ values were not consistent between sampling days, which further limits our ability to compare the different trends observed in muscle and liver tissue. However, the most consistent isotope shift was observed during the first 90 days of the experiment with two consecutive negative changes in dietary AA $\delta^{13}C$ values. These changes are also reflected during that period in liver tissue, which highlights the potential of CSIA to differentiate between even small differences of dietary intake. Although we did not quantify the exact cellular turnover rate of individual AAs in stickleback tissues, knowing an estimated timeline for evaluating the diet of an animal is useful for ecological studies investigating migration or seasonal changes of food sources. It has been shown that choosing different tissue types in individuals enables researchers to explore temporal and spatial resource use of animals and it is critical to consider incorporation rates of isotope signatures into these tissues [122, 123]. Most studies so far on isotopic incorporation and turnover rates are still based on BSIA [124-126] and enhancing our knowledge to specific compounds in different tissues can provide powerful opportunities to study the physiology of migrating animals, which are hard to capture multiple times. In addition, the analysis of AA isotope signatures of these animals from tissues with different incorporation rates can help to illuminate temporal variations and identify endogenous vs. exogenous resources, without the need of multiple sampling points.

The initial amino acid isotope signature of mosquito larvae used for feeding shows typical patterns also seen in other studies, where Gly and Ser are the most ^{13}C-enriched AAs and EAAs are isotopically ^{13}C-depleted in comparison to NEAAs [49, 85, 90-95, 97, 99, 127]. NEAAs can be synthesized *de novo* in higher organisms, leading to isotopic fractionation during metabolism and nutrient flow from primary producers to top predators in a given food web [99]. It is known that the carbon stable isotope composition of NEAA in higher organisms is therefore flexible and varies according to dietary protein and lipid intake. A study from McMahon et al. (2010) [95] fed common mummichogs on four isotopically distinct diets with different protein and lipid compositions and measured the carbon stable isotope signature of individual AAs from muscle tissue. In two high protein diets

based on clam and squid, they found $\Delta\delta^{13}C$ values between -4 and -7 ‰ for Ala, Ser and Gly, whereas trophic fractionation was lower for other NEAAs and absent for EAAs. The protein and lipid contents in both diets were 70 % and 18 %, respectively. Another study from Newsome et al. (2014) [128] fed rodents diets of different protein and lipid contents with distinct isotope signatures and found that NEAA $\delta^{13}C$ values in muscle tissue shifted more towards dietary lipids with lower protein/lipid ratios, whereas a protein and lipid content of 40 and 5 % resulted in NEAA $\delta^{13}C$ close to the protein source. Our study used commercially available dried mosquito larvae with a protein/lipid content of 60 % and 5 %, respectively, and therefore represents a diet with a higher protein to lipid ratio than previous studies. Our results show low isotope fractionations for NEAAs and EAAs between diets and fish tissue and support the idea of isotope routing when animals are fed protein rich diets, which is energetically favorable compared to *de novo* synthesis. High isotope fractionations of ±5 ‰ of some NEAAs between diet and consumer, as described by other studies [93, 95], did not occur in our case, probably due to the low abundance of other macronutrients. Fractionation between muscle and dietary samples was visible for Ala, Asx, Glx, Ser, His, Lys and Thr especially on day 90, but these differences are a direct result of muscle tissue not responding to the shifting stable isotope signatures in diets and not due to trophic fractionation. The highest difference in dietary $\delta^{13}C$ values over time were observed between day 30 and 90 of the feeding experiment. Since muscle tissue has a low turnover rate and is a more conservative indicator of long-term dietary intake, the lack of response to the short-term isotopic shifts in dietary samples results in higher differences between muscle and dietary samples on day 90. Small but significant $\Delta\delta^{13}C$ values were observed between liver and dietary samples for Asx, Glx, Ser and Tyr over the whole sampling period and occasionally for Ala and Gly on individual sampling days. The trophic fractionation of Ser in the liver was striking and consistently between -1 and -2 ‰ and Gly was the only NEAA who showed an opposite trend of positive $\Delta\delta^{13}C$ values on day 90 and 120. Catabolic pathways for Ser involve deamination to pyruvate, transamination with pyruvate to form hydroxy pyruvate and alanine and formation of Gly with tetrahydrofolate [129]. Additionally, participation of Gly into gluconeogenesis requires the conversion of Gly to Ser by serine hydroxy methyltransferase and both AAs participate further in sulfur and one-carbon metabolism [102]. The liver plays a major role in energy and amino acid metabolism by regulating and controlling gluconeogenesis as well as synthesizing many of the NEAAs [111]. Synthesis of NEAA carbon backbones can occur from either glycolytic

intermediates for Gly, Ser and Ala or from Krebs cycle intermediates for Asx and Glx [130]. It is, however, hard to estimate the contribution of isotopic fractionation for each of these pathways, not only because intrinsic fractionation and mass flow are unknown, but also because metabolic pathways are often intertwined and hard to separate in living organisms at natural abundance level. Enzymatic reactions and catabolism of nutrients are usually associated with discrimination against the heavier isotopes, in this case ^{13}C, leading to depleted signatures in the product, while the educt of the reaction becomes isotopically ^{13}C-enriched [131]. The small enrichment of Gly observed in liver could therefore be indicative of extensive conversion of Gly to other compounds, with Ser being one possibility and resulting in more noticeable negative $\Delta\delta^{13}C$ values. It is, however, a far stretch at this point to account the small isotopic differences in Ser and Gly to specific metabolic or enzymatic reactions, especially since metabolism of Gly and Ser involve several different pathways. Future research and controlled feeding experiments could focus on using isotopically labeled substitutes to track individual metabolic pathways, such as the conversion of Gly and Ser. Pro was the only NEAA in liver tissue showing no trophic fractionation at all over the sampling period, which points more to a behavior like an EAA being routed by diets. As mentioned in the introduction, Pro can be synthesized in higher organisms, but the classification as a NEAA is sometimes misleading as metabolic requirements might heavily outmatch *de novo* synthesis. Our results indicate that fish fed on high protein content incorporate Pro mostly from dietary sources leading to no or very little fractionation in both liver and muscle tissue. Arg and Lys were EAAs with very low fractionation overall, strongly following the trend of dietary isotope signatures even in muscle tissue over short time periods. Arg is highly abundant in fish protein and tissue fluid [102], serving as a precursor for the synthesis of proteins, nitric oxide, urea, Pro, Glx and creatine [132]. Arg is of special interest here because it is not often reported in the literature, since most studies apply GC-IRMS for measurement of carbon isotope signatures of AAs, which requires derivatization and results in the loss of Arg [48, 133]. Because of the high abundance, demand and turnover of dietary Arg in fish leading to very little fractionation even in muscle tissue over a short-term dietary isotope shift, it could serve as another proxy in addition to Phe, Leu, Ile and Lys [92-95] to track carbon sources from primary producers in muscle or liver tissue. Identifying EAAs with very low fractionation patterns is pivotal for ecological studies using isotope fingerprinting to better constrain the source of end-member signatures and study the

carbon flow in terrestrial and oceanic environments [85, 90, 91, 95-97, 99]. Phe and His were the only EAAs showing consistently different isotope signatures between diet and fish tissue, which is surprising since they need to be directly taken up and rooted from dietary sources. Phe can be converted to Tyr and the depleted isotopic signature of Tyr compared to diets could therefore also be explained by enzymatic fractionation discriminating against the heavy carbon isotopes. Although EAAs cannot be synthesized by eukaryotes, the fundamental assumption that these constituents must be solely sourced from dietary protein resulting in low isotope fractionation of ~0 ‰ has not always been met. There are studies suggesting that gut microbes can contribute to the homeostasis of EAAs in animals by *de novo* synthesis, which of course complicates their use as stable and robust proxies for isotope fingerprinting [99, 134-137]. The contribution of microorganisms in the gut of sticklebacks to the EAAs homeostasis could explain the observed difference of Phe and Tyr isotope signatures in fish muscle and liver tissue compared to diets and highlights the importance to experimentally explore the variation of EAA isotope fractionation by gut microbiome. According to our results, Arg and Lys might therefore be better suited in sticklebacks and possibly other teleost species to estimate their carbon flow and allocate resource consumption, if the contribution of gut symbionts is of no interest. His showed overall the highest fractionation among the analyzed AA. We investigated possible influences of the closely eluding and much more abundant Lys on the $\delta^{13}C$ values of the less abundant His by varying peak integration and background detection methods in the ISODAT 2.0 software but found no indication that the high fractionation patterns were caused by chromatographic interferences. Differences in the peak area ratios of Lys/His were different between tissues, but the observed trend of increasing ratios of Lys/His from dietary to liver and finally muscle tissue does not match the increasing $\delta^{13}C$ patterns from dietary to muscle and then liver tissue. Although we cannot exclude any influence of poor peak resolution between Lys and His and the different ratios on their carbon isotope signatures, we think that these influences would not result in the high fractionation patterns that we observed. This is also supported by an earlier study showing that poor peak resolution in LC-IRMS does not greatly influence the measured carbon isotope signatures, as compared to GC-IRMS [138]. The previously mentioned *de novo* synthesis and contribution of EAAs from gut microbes could of course be one explanation for the highly ^{13}C-enriched isotope signatures of His in in stickleback liver and muscle tissue. Other reasons could include the enzyme histidine decarboxylase, which is produced by bacteria and causes histamine fish poisoning [139,

140]. It has been speculated before that histidine decarboxylase might still be released from autolyzing of bacterial cells during and after freeze drying and convert histidine to histamine [141]. Enzymatic reactions are known to cause isotopic fractionation, which usually discriminates against the heavier isotope [131] and could result in enriched isotope signature of the remaining histidine in fish tissue. Interestingly, an early study investigating histamine concentrations during storage of flesh and liver tissue of mackerel under different conditions showed a higher increase of histamine concentrations in the liver [142], which would fit to the higher isotope values of histidine in stickleback liver compared to muscle tissue, if it was caused by enzymatic reactions. Testing this, however, would require histamine isotope measurements in dietary and fish samples to compare isotope signatures and was out of scope of this study. Another explanation would be that sticklebacks fed on mosquito larvae lack dietary histidine to match their metabolic requirements. We did not directly measure the protein and AA content of dietary mosquito larvae, but His has been mentioned in the literature as a more frequent limiting AA when animals are fed with insect meals [143]. His is an important amino acid for growth, tissue formation and hemoglobin synthesis in fish [144] and a lack of dietary His may lead to increased fractionation in consumer tissue due to catabolism during starvation. There is however no consensus so far on the isotopic effect of starvation or nutritional stress on consumer tissue [145] especially for single compounds, and such effects could be subject for further studies.

ASCA provided an alternative way to PCA and LDA as classical multivariate analysis and was especially useful in our case because we could incorporate the structure of our experiment into the model, with sampling days and tissue types as two separate factors [146]. This removed a lot of "noise" from the dietary isotope shift when investigating AA $\delta^{13}C$ patterns between tissue types. All NEAAs except Pro had high positive (Ala, Asx, Glx and Ser) or negative (Gly) loadings on PC1, whereas loadings of EAAs and Pro were low. Sample scores on PC1 were negative for liver samples and either 0 or positive for muscle and dietary samples, which shows that NEAAs in the liver have distinct $\delta^{13}C$ patterns. Since liver samples had exclusively negative scorings on PC1, NEAAs with positive loadings (Ala, Asx, Glx and Ser) therefore showed a pattern of ^{13}C-depletion compared to muscle and diets. As mentioned earlier, the liver plays a major role in biosynthesis of NEAAs, which is dependent on dietary content of macronutrients. Because we used a diet of high protein and relatively low lipid composition, synthesis of

NEAA from other nutrients in the liver might be limited but is still visible when combining $\delta^{13}C$ values of individual AAs in a multivariate approach. Lipids in natural samples typically have lower $\delta^{13}C$ values compared to AAs or carbohydrates [100, 101] and partial biosynthesis of NEAAs from lipids in the liver would therefore result in slightly lower $\delta^{13}C$ values. The observed low loadings of EAAs on PC1 support this assumption since they cannot be synthesized *de-novo* from other macronutrients in the liver and therefore do not show distinct $\delta^{13}C$ patterns between muscle and liver tissue. Sample scores of factor 2 (sampling days) from ASCA reflected the changing $\delta^{13}C$ values in samples induced by the dietary isotope shift, with decreasing $\delta^{13}C$ values during the first 90 days and a small increase after 120 days. Since all AA loadings on factor 2 were positive and within 0.15 to 0.4, the shift of $\delta^{13}C$ values over time was similar between individual AAs.

3.5 Conclusion

Studying the isotope signature of AAs between diet and consumer gained much attraction during the last years, yet our knowledge of the fundamental principles behind isotope incorporation and fractionation of individual substitutes is still limited. Our study shows that direct isotope routing even of NEAAs might still be the preferred way for nutrient assimilation when fish are fed with high protein diets, and there are not only differences in isotopic turnover rates between muscle and liver, but also different isotopic behaviors that individual AAs in these tissues show based on their metabolic role. However, investigating isotope fractionation of AAs on natural abundance levels might not be the best approach to study fundamental incorporation and turnover patterns, since a lot of information might be lost to natural variations and measurement uncertainty. Although the use of multivariate analysis can help to find general patterns of $\delta^{13}C$ values between tissue types, we recommend the use of ^{13}C-enriched materials in controlled feeding experiments to accurately track metabolic pathways. One good example to investigate could be the mentioned conversion of Gly and Ser or biosynthesis of NEAAs in the liver, which has the potential to greatly improve our understanding of nutrient assimilation and conversion and is long overdue for the correct analysis and interpretation of field data. On the other hand, it is promising to see that even small differences and fluctuations of isotope values, which are more realistically encountered in nature, can be investigated using CSIA of different sample materials.

3.6 Materials and methods

3.6.1 Feeding experiment

Three-spined Sticklebacks were laboratory-raised offspring and reared in twelve 14 L tanks (VewaTech, Germany) as part of a parasitic infection experiment. Water was recirculated and held at 18 °C with a 15 h light and 9 h dark cycle. Stickleback offspring were produced by *in vitro* fertilization from individuals collected from a brook in North-West Germany (52°17'33.11"N, 7°36'46.48"E), about eight months old at the beginning of the experiment and fed daily with washed red mosquito larvae (*Chironomidae*) over the course of four months. Each lab tank contained twelve individuals, which were divided into two groups. The first group consisted of 3 individuals per tank, which were exposed to an uninfected copepod as a sham-exposed control group, while the other 9 individuals per tank were exposed to an infected copepod as a parasite-exposed group. Three complete lab tanks with 36 individuals were sampled on each sampling date (30-, 60-, 90- and 120-days post exposure) and five out of the fifteen sham-exposed individuals per sampling date were randomly selected for CSIA. Sub samples of mosquito larvae were taken once a week, stored at -20 °C and pooled between 1-30, 31-60, 61-90 and 91-120 days for CSIA. Dried red mosquito larvae are commercially available and a protein rich diet for fish, with a crude protein content of up to 60 % and a crude lipid content of around 5 %. The AA profile is balanced and adequate for fish farming, although His, Lys or Try can be lacking depending on the used insect species [143, 147, 148]. Sticklebacks were starved 72 h prior sampling, anesthetized with MS 222 (Sigma-Aldrich, USA) and killed by decapitation. Liver and muscle tissue were collected without skin and bones and stored at -20 °C until further use. Sticklebacks were maintained and treated in accordance with the local animal welfare authorities and the EU Directive 2010/63/EU for animal experiments. All animal experiments described were approved by the 'State Agency for Nature, Environment and Consumer Protection' (LANUV) of North Rhine Westphalia, which includes the evaluation by an ethics committee, under the project number 87 51.04.2010.A297. The present study was carried out in compliance with the ARRIVE guidelines (https://arriveguidelines.org/).

3.6.2 Sample preparation

Hydrolysis of amino acids for LC-IRMS analysis has been described in the literature [49, 53, 127]. Approximately 5 mg of sample material were weighed into 5 mL PTFE vials

(CEM GmbH, Kamp-Lintfort, Germany) and 2.5 mL (1:500 ratio of mass to volume) of 6 M hydrochloric acid (>99 %, Alfa Aesar, Kandel, Germany) were added. The vials were closed and kept in a UT 5042 drying oven (Heraeus, Hanau, Germany) at 110 °C for 24 h. The hydrolysate was filtered (0.2 µm PTFE filter), evaporated to dryness under vacuum at 40 °C, reconstituted in 1 mL distilled water and filtered again into small 1.5 mL HPLC vials. The vials were frozen at -20 °C until LC-IRMS analysis. Glutamine and asparagine are converted to their respective acidic form during this treatment and measured together with glutamic and aspartic acid. Tryptophan and cysteine are lost during acid hydrolysis and the amount of methionine was too low to be measured accurately.

3.6.3 LC-IRMS analysis of AAs

The analysis of individual AAs was performed on a Dionex Ultimate 3000 HPLC Pump (Thermo Fisher Scientific, Bremen, Germany) coupled to an Isolink Interface and Delta V Advantage mass spectrometer (Thermo Fisher Scientific, Bremen, Germany). Separation was achieved for 13 AAs (**Figure 3.3**) with a mixed mode cation exchange column (Primesep A, 2.1 mm ID, 250 mm L, 5 µm particle size) from SIELC, which was in accordance with other studies employing the same separation technique [49, 53, 127]. The exact program is described by a study from Raghaven et al. (2010) [49] and uses a gradient from mobile phase A (100 % water, pH 7) to mobile phase B (0.3 M sulfuric acid, pH 1.5) and column temperature was held at 30 °C. To preserve the HPLC column, which is very sensitive to pH values of over 7, we adjusted the method to start with water at pH 4 as mobile phase A. Flow rate of the mobile phase was set to 260 $\mu L min^{-1}$ and oxidation agents (1.5 M orthophosphoric acid and 100 $g L^{-1}$ disodium peroxodisulfate, Merck, Darmstadt, Germany) were pumped at 25 $\mu L min^{-1}$ each. This resulted in an oxygen background of approximately 12 V on the first cup of the IRMS, which is the recommended value by the manufacturer to guarantee sufficient oxidation conditions. The experimental units were replicates of pooled dietary samples (n = 3) and biological replicates of stickleback tissues (liver and muscle, n = 5) for each of the four sampling days taken at day 30, 60, 90 and 120 and the small sample amount of obtained stickleback tissue did not allow for within-individual replicate analysis. Each hydrolyzed sample was injected in triplicate into the LC-IRMS system and outliers were determined by Grubbs Test on a confidence level of 0.95 and excluded from further analysis. We calculated mean values and SD from triplicate injections to estimate instrumental precision before referencing our data. Instrumental precision was estimated with an average SD of 0.47 ‰ for

triplicate injections of all AAs, tissues, and sampling days (n = 674). SDs of triplicate injections of all AAs from either dietary samples (0.51 ‰, n = 156), liver samples (0.50 ‰, n = 258) and muscle samples (0.41 ‰, n = 260) where almost equal over the complete sampling period. The robustness of sample preparation and hydrolysis was assessed by conducting replicate analysis (n = 3) of dietary samples, since these were the only samples providing enough material for multiple replicates. The average SD of replicate analysis was 0.36 ‰ and therefore in the same range as triplicate injections. Twelve in-house amino acid standards (Ala, Asx, Arg, Glx, Gly, His, Lys, Pro, Phe, Ser, Thr and Tyr) were purchased with a purity of >98 % (Alfa Aesar, Kandel, Germany) and measured against seven certified international AA reference materials (L-Alanine, L-Glutamic acid, USGS 64, USGS 66, L-Phenylalanine, L-Proline and L-Valine), purchased from Arndt Schimmelmann, Department of Earth and Atmospheric Sciences at Indiana University (Bloomington, IN, USA), on an Isoprime100 Elemental Analyser (Elementar Analysensysteme GmbH, Langenselbold, Germany). A mix of the in-house standards with a concentration of 100 mgL^{-1} for each amino acid was regularly measured in between sample runs and used to directly assign final isotope values on the VPDB scale. Measurements of pooled AA in-house standards were further monitored to ensure equal system and method performance throughout the prolonged measurement periods and the SD of AA standards never exceeded 0.6‰ (N = 34, 17 and 20, respectively; **Table 3.6**). This procedure ensures accurate long-term isotope data and follows the identical treatment procedure [15]. Five primary RM were measured on the LC-IRMS system before the start of a four week-long measurement (10 and 5 µL injection volumes, each in triplicate). The measured $\delta^{13}C$ values of the five RM were calibrated with the AA in-house standards and were in good agreement with the true literature values except for USGS 41, which showed conversion of glutamic acid to pyroglutamic acid and is a known problem even with the newer USGS 41a material [81]. Chromatograms were individually checked for proper background and peak detection. The automated dynamic background detection algorithm from ISODAT 2.0 software with a block width of 1000 [50] was in many cases able to accurately estimate the background signal, but manual adjustments had to be made, e.g. for closely eluding AAs or interference of matrix components.

3.6.4 Data analysis

Data analysis was done using Excel from Microsoft Office 365 ProPlus (Microsoft, Redmond, Washington, USA), Origin 2019 version 9.60 (OriginLab, Northampton,

Massachusetts, USA) and Matlab R2021a (MathWorks Inc., Natick, Massachusetts, USA) with the PLS_Toolbox suite (Eigenvector Research Inc., Manson, WA). Isotope data are reported as mean $\delta^{13}C_{AA}$ values on the VPDB scale in ‰ with its corresponding standard deviation (**Table 3.2**). Data was tested for normality with Kolmogorov-Smirnov-Test on a confidence level of 0.95, which was not violated for any given AA and sample. One-way analysis of variance (ANOVA) was used on $\delta^{13}C$ values of each tissue to test for differences of AAs between sampling days (fixed factor). Using sampling days as an independent variable in ANOVA can be problematic because it is not strictly categorial, but each of our sample represents an independent fish individual which couldn't be sampled multiple times and is therefore not a repeated measure. We further conducted ANOVA simultaneous component analysis (ASCA) as a multivariate analysis in a design of experiment approach, with sampling days and tissue types as fixed factors and $\delta^{13}C$ of each AA as multivariable. ASCA combines the principles of ANOVA and PCA [146] and allows to investigate differences in the isotope signature between tissues without the influence of the expected isotope shift over time dominating our analysis. $\delta^{13}C$ data for ASCA was used without preprocessing and the analysis performed with 1000 permutations.

$\Delta\delta^{13}C$ values of individual AAs were first calculated individually between each stickleback sample (muscle, liver) and dietary sample and then averaged over all samples on either 1) all days or 2) each sampling day (**Table 3.4**). $\Delta\delta^{13}C$ were pooled for NEAAs and EAAs to test for differences in trophic fractionation between those groups among all days. Two-sided t-tests on $\Delta\delta^{13}C$ values of individual AAs were used to test for differences in trophic fractionation against 0‰ on individual sampling days. The significance level α was set to 0.01 to compensate for the low number of biological replicates (n = 5 for fish tissue) that were analyzed, and each ANOVA analysis was accompanied by Brown-Forsythe tests (α = 0.05) to check for equality of group variances and followed up with Tukey *post hoc* tests to identify significant differences between group values. Reducing the significance level avoids false-positive results for small sample sizes, but it consequently increases false-negative results, and we are therefore only discussing the most significant differences of our data, while smaller differences might be lost.

3.7 Appendix to chapter 3

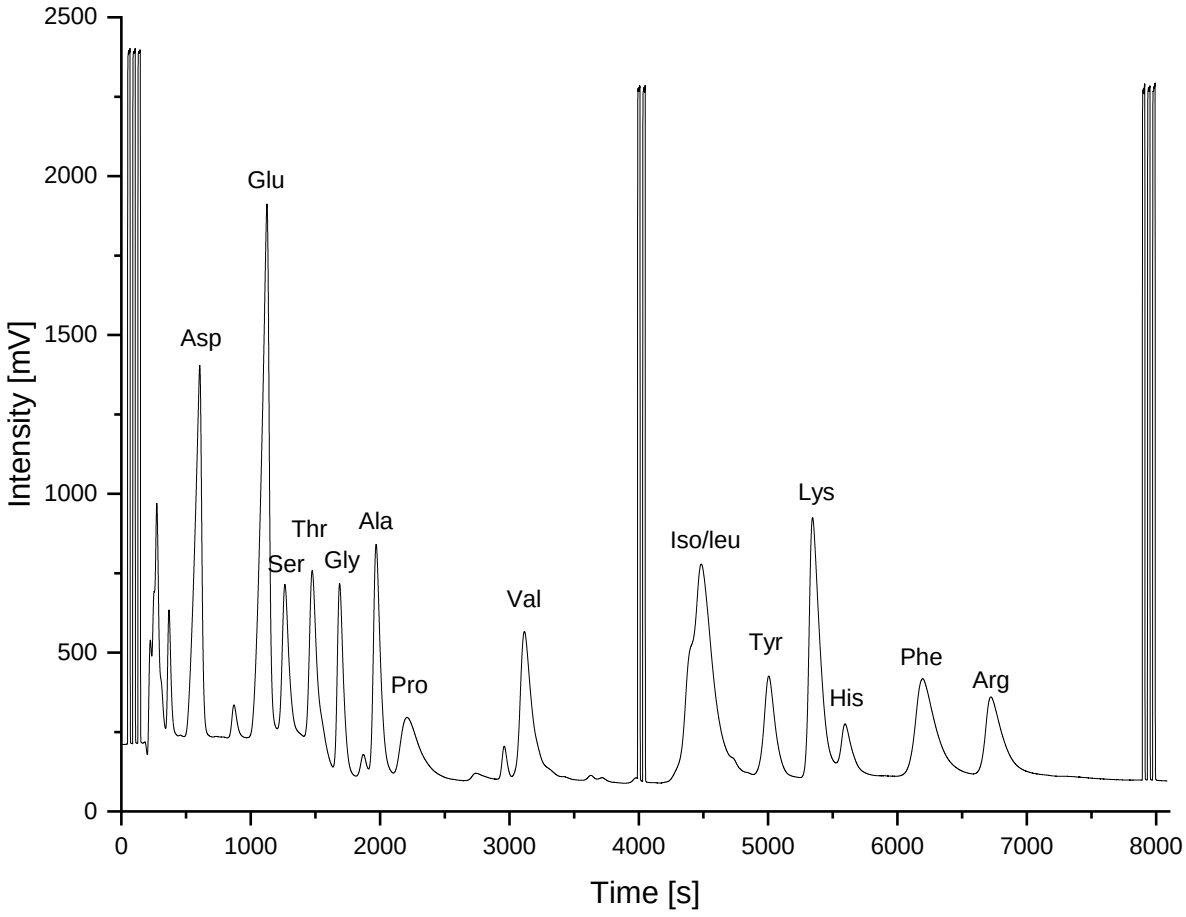

Figure 3.3: Chromatographic separation of 13 AAs from fish muscle. Val was excluded from this study because it coeluted with an unknown species in dietary samples. Met and Cys were not measurable after hydrolysis due to decomposition or low abundance.

Table 3.2: Average AA $\delta^{13}C$ values and standard deviations (SD) in ‰ for each sampling day of dietary (n = 3), liver (n = 5) and muscle (n = 5) samples.

Tiss	Sampling	Ala		Asp		Glu		Gly		Pro		Ser	
		Avg	SD	Avg	SD	Avg	SD	Avg	SD	Avg	SD	Avg	SD
Diet	30	-	0.1	-11.0	0.1	-11.4	0.6	-6.0	0.3	-12.5	0.5	-1.1	0.4
	60	-	0.4	-12.2	0.4	-12.4	0.5	-7.2	0.4	-13.9	0.3	-2.8	0.7
	90	-	0.4	-14.4	0.5	-14.1	0.3	-8.8	0.1	-14.8	0.7	-4.5	0.4
	120	-	0.3	-13.1	0.4	-12.7	0.3	-7.6	0.5	-13.9	0.3	-3.3	0.4
Liver	30	-	0.9	-11.8	1.1	-11.9	1.0	-7.1	1.0	-13.7	1.5	-3.8	1.1
	60	-	0.9	-12.8	0.8	-13.9	0.8	-7.3	0.8	-14.8	0.8	-4.9	1.4
	90	-	1.0	-14.8	1.1	-14.5	1.6	-7.0	0.9	-14.7	1.8	-5.8	1.0
	120	-	0.9	-14.2	0.9	-13.3	0.7	-5.9	0.7	-14.0	1.1	-4.4	0.7
Muscle	30	-	1.0	-11.7	1.0	-11.8	0.9	-7.9	1.1	-13.9	0.9	-2.1	1.1
	60	-	0.6	-11.9	0.6	-11.9	0.3	-7.6	0.5	-14.5	0.7	-0.9	0.6
	90	-	0.3	-12.7	0.5	-12.4	0.7	-8.7	0.5	-15.1	0.8	-2.5	0.6
	120	-	0.5	-12.2	0.4	-12.2	0.4	-7.5	0.8	-14.0	1.0	-2.7	0.8
Tiss	**Time**	**Arg**		**His**		**Lys**		**Phe**		**Thr**		**Tyr**	
		Avg	SD	Avg	SD	Avg	SD	Avg	SD	Avg	SD	Avg	SD
Diet	30	-	0.3	-15.4	0.6	-14.5	0.4	-22.1	0.1	-10.8	0.3	-19.2	0.7
	60	-	0.3	-16.3	0.3	-15.7	0.3	-23.4	0.1	-12.6	0.3	-20.4	0.5
	90	-	0.4	-17.7	0.9	-17.5	0.3	-25.0	0.5	-14.0	0.2	-21.5	0.3
	120	-	0.6	-16.4	0.7	-16.6	0.3	-24.3	0.1	-12.5	0.1	-21.5	0.0
Liver	30	-	0.5	-8.6	0.5	-14.6	0.4	-23.8	0.6	-10.4	0.7	-19.9	0.4
	60	-	0.4	-7.8	0.9	-16.2	0.4	-24.6	0.7	-11.7	0.7	-21.4	0.4
	90	-	1.0	-9.0	1.1	-16.7	0.8	-25.1	0.8	-12.6	1.4	-22.9	1.3
	120	-	0.3	-7.6	0.8	-17.2	0.6	-26.0	0.6	-11.6	1.0	-23.2	0.5
Muscle	30	-	1.0	-11.6	1.1	-15.3	0.9	-23.8	0.8	-11.4	1.0	-21.6	1.2
	60	-	0.8	-11.4	0.7	-15.7	0.3	-24.4	0.6	-11.4	0.9	-21.9	0.6
	90	-	0.6	-11.1	0.9	-16.2	0.4	-25.0	0.4	-11.9	0.7	-22.8	0.9
	120	-	0.2	-12.0	1.1	-16.3	0.3	-24.6	0.2	-12.8	0.5	-22.2	0.5

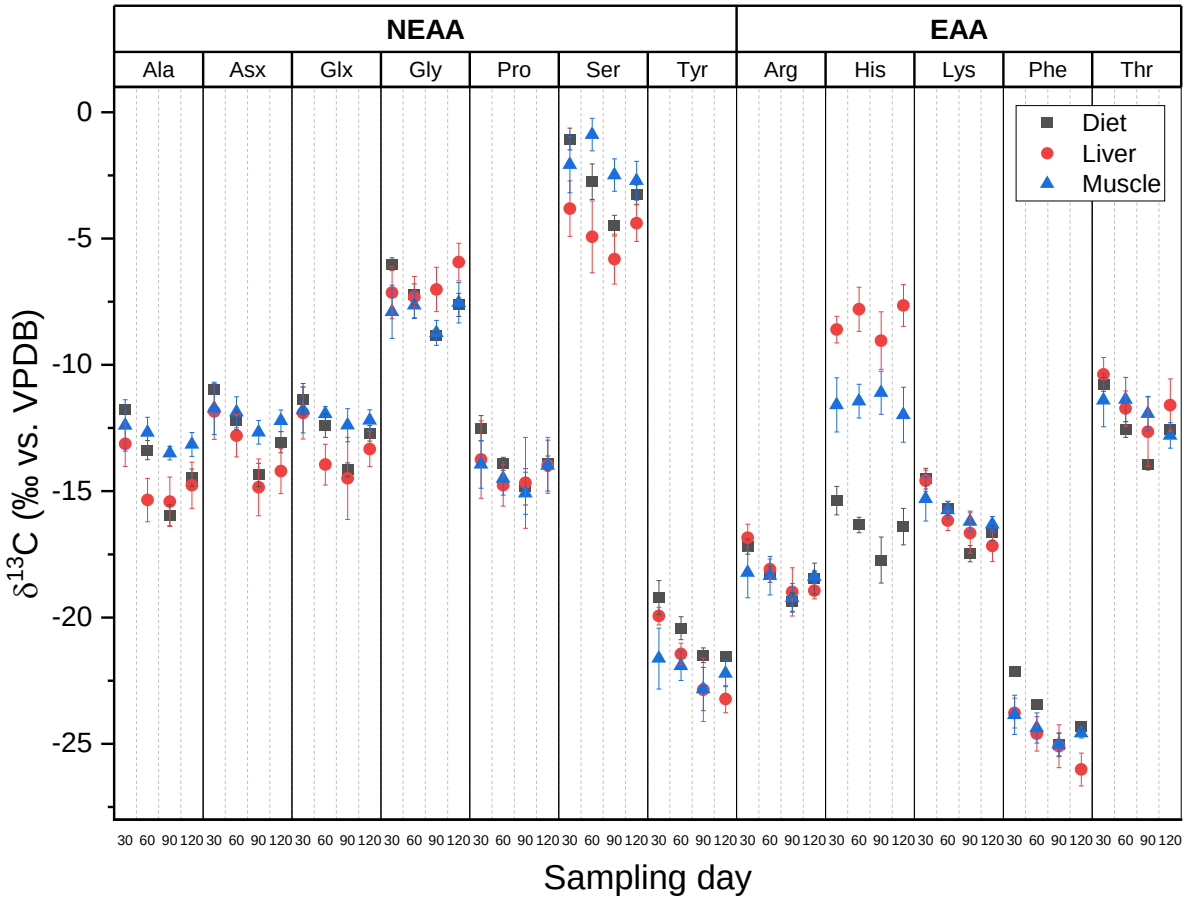

Figure 3.4: Average $\delta^{13}C$ values ± SD (error bars, n = 5) are given in ‰ after 30, 60, 90 and 120 days of the experiment for dietary, muscle and liver samples. $\delta^{13}C$ values in dietary samples are decreasing over the first 90 days of the experiment, which also causes a significant decrease in $\delta^{13}C$ values of liver samples between day 30 and 90 of the sampling period (one-way ANOVA, $p < 0.01$). The decrease in $\delta^{13}C$ values of muscle samples was not significant between any sampling date.

Table 3.3: AAs in the liver show higher variability in their carbon isotope signatures in response to dietary $\delta^{13}C$ shifts over time. F-values and average differences between $\delta^{13}C$ values (dependent variable) on each sampling day (independent variable) are given from one-way ANOVA (DF = 3, 8) and Tukey tests for each individual AA and tissue. $\Delta\delta^{13}C$ values are given in ‰ with their p-values in brackets and significant differences ($p < 0.01$) are marked italic bold. All dietary AAs except His have significantly different $\delta^{13}C$ values between sampling days, which are mostly driven by differences between 30 and 90 days. AA $\delta^{13}C$ values in the liver are significantly different for Ala, Asx, Arg, Lys, Phe and Tyr and are also mainly driven by differences between 30 and 90, with the addition of Glx between those specific days. The AA $\delta^{13}C$ values in the muscle are not significantly different between any sampling days.

Tissue	AA	F - value	$\Delta\delta^{13}C_{60-30}$	$\Delta\delta^{13}C_{90-30}$	$\Delta\delta^{13}C_{90-60}$	$\Delta\delta^{13}C_{120-30}$	$\Delta\delta^{13}C_{120-60}$	$\Delta\delta^{13}C_{120-90}$
Diet	Ala	***84.2 (0.000)***	***-1.6 (0.002)***	***-4.2 (0.000)***	***-2.6 (0.000)***	***-2.7 (0.000)***	-1.1 (0.017)	***1.5 (0.003)***
	Asx	***44.7 (0.000)***	-1.2 (0.015)	***-3.4 (0.000)***	***-2.2 (0.000)***	***-2.1 (0.001)***	-0.9 (0.082)	1.3 (0.011)
	Glx	***20.5 (0.000)***	-1.0 (0.078)	***-2.8 (0.000)***	***-1.8 (0.005)***	-1.3 (0.024)	-0.3 (0.826)	1.4 (0.016)
	Gly	***35.9 (0.000)***	-1.2 (0.011)	***-2.8 (0.000)***	***-1.6 (0.002)***	***-1.6 (0.002)***	-0.4 (0.462)	1.2 (0.010)
	Pro	***11.9 (0.003)***	-1.4 (0.029)	***-2.3 (0.002)***	-0.9 (0.170)	-1.4 (0.030)	0.0 (1.000)	0.9 (0.165)
	Ser	***24.3 (0.000)***	-1.7 (0.014)	***-3.4 (0.000)***	-1.7 (0.012)	***-2.2 (0.003)***	-0.5 (0.614)	1.2 (0.066)
	Tyr	***19.3 (0.001)***	-1.2 (0.036)	***-2.3 (0.001)***	-1.1 (0.064)	***-2.3 (0.001)***	-1.1 (0.055)	0.0 (0.999)
	Arg	***13.8 (0.002)***	-1.1 (0.051)	***-2.2 (0.001)***	-1.1 (0.049)	-1.3 (0.025)	-0.2 (0.956)	0.9 (0.100)
	His	6.4 (0.016)	-1.0 (0.348)	-2.4 (0.011)	-1.4 (0.123)	-1.0 (0.301)	-0.1 (0.999)	1.3 (0.145)
	Lys	***45.9 (0.000)***	-1.2 (0.010)	***-3.0 (0.000)***	***-1.8 (0.001)***	***-2.2 (0.000)***	-1.0 (0.027)	0.8 (0.060)
	Phe	***68.6 (0.000)***	***-1.3 (0.001)***	***-2.9 (0.000)***	***-1.6 (0.000)***	***-2.2 (0.000)***	-0.9 (0.015)	0.7 (0.035)
	Thr	***92.0 (0.000)***	***-1.8 (0.000)***	***-3.2 (0.000)***	***-1.4 (0.000)***	***-1.8 (0.000)***	0.0 (1.000)	***1.4 (0.000)***
Liver	Ala	***6.8 (0.004)***	***-2.2 (0.007)***	***-2.3 (0.005)***	-0.1 (0.999)	-1.6 (0.052)	0.6 (0.747)	0.6 (0.680)
	Asx	***9.2 (0.001)***	-1.0 (0.453)	***-3.0 (0.001)***	-2.0 (0.024)	***-2.4 (0.009)***	-1.4 (0.161)	0.6 (0.741)
	Glx	5.1 (0.011)	-2.0 (0.043)	***-2.6 (0.009)***	-0.5 (0.861)	-1.4 (0.211)	0.6 (0.813)	1.2 (0.372)
	Gly	2.6 (0.091)	-0.2 (0.989)	0.1 (0.995)	0.3 (0.947)	1.2 (0.167)	1.4 (0.097)	1.1 (0.243)
	Pro	0.7 (0.577)	-1.0 (0.650)	-0.9 (0.713)	0.1 (1.000)	-0.2 (0.993)	0.8 (0.801)	0.7 (0.853)
	Ser	3.2 (0.054)	-1.1 (0.425)	-2.0 (0.042)	-0.9 (0.611)	-0.6 (0.826)	0.5 (0.872)	1.4 (0.191)
	Tyr	***20.8 (0.000)***	-1.5 (0.024)	***-2.9 (0.000)***	-1.4 (0.035)	***-3.3 (0.000)***	***-1.8 (0.007)***	-0.4 (0.853)
	Arg	***13.7 (0.000)***	-1.2 (0.023)	***-2.1 (0.000)***	-0.9 (0.127)	***-2.1 (0.000)***	-0.8 (0.159)	0.1 (0.999)
	His	2.8 (0.077)	0.8 (0.530)	-0.4 (0.856)	-1.2 (0.189)	1.0 (0.341)	0.2 (0.994)	1.4 (0.095)
	Lys	***18.4 (0.000)***	***-1.6 (0.003)***	***-2.1 (0.000)***	-0.5 (0.559)	***-2.6 (0.000)***	-1.0 (0.065)	-0.5 (0.522)
	Phe	***8.9 (0.001)***	-0.8 (0.281)	-1.3 (0.040)	-0.5 (0.689)	***-2.2 (0.001)***	-1.4 (0.026)	-0.9 (0.201)
	Thr	4.4 (0.019)	-1.3 (0.179)	-2.3 (0.011)	-0.9 (0.478)	-1.2 (0.253)	0.1 (0.996)	1.1 (0.362)
Muscle	Ala	2.8 (0.071)	-0.3 (0.901)	-1.1 (0.070)	-0.8 (0.230)	-0.8 (0.294)	-0.5 (0.666)	0.3 (0.830)
	Asx	1.9 (0.172)	-0.2 (0.983)	-0.9 (0.167)	-0.8 (0.294)	-0.5 (0.674)	-0.3 (0.864)	0.5 (0.718)
	Glx	1.0 (0.440)	-0.2 (0.976)	-0.6 (0.431)	-0.4 (0.670)	-0.4 (0.711)	-0.3 (0.910)	0.2 (0.962)
	Gly	2.6 (0.090)	0.3 (0.944)	-0.8 (0.336)	-1.1 (0.141)	0.4 (0.872)	0.1 (0.997)	1.2 (0.098)
	Pro	1.9 (0.175)	-0.6 (0.744)	-1.1 (0.204)	-0.6 (0.719)	0.0 (1.000)	0.5 (0.792)	1.1 (0.235)
	Ser	5.0 (0.013)	1.2 (0.139)	-0.4 (0.851)	-1.6 (0.031)	-0.6 (0.611)	-1.8 (0.013)	-0.2 (0.971)
	Tyr	1.9 (0.170)	-0.3 (0.946)	-1.2 (0.145)	-0.9 (0.340)	-0.6 (0.685)	-0.3 (0.940)	0.6 (0.658)
	Arg	2.2 (0.133)	-0.1 (0.992)	-1.0 (0.146)	-0.9 (0.232)	-0.2 (0.981)	0.0 (1.000)	0.8 (0.269)
	His	0.7 (0.541)	0.1 (0.994)	0.5 (0.847)	0.3 (0.941)	-0.4 (0.911)	-0.5 (0.801)	-0.9 (0.475)
	Lys	3.7 (0.034)	-0.4 (0.573)	-0.9 (0.075)	-0.5 (0.552)	-1.0 (0.040)	-0.6 (0.369)	-0.1 (0.987)
	Phe	4.0 (0.027)	-0.5 (0.461)	-1.2 (0.017)	-0.7 (0.267)	-0.7 (0.200)	-0.2 (0.935)	0.5 (0.568)
	Thr	3.4 (0.044)	0.0 (1.000)	-0.5 (0.728)	-0.6 (0.698)	-1.4 (0.064)	-1.4 (0.058)	-0.9 (0.359)

Table 3.4: Essential and non-essential AAs are mostly rooted from dietary sources in liver and muscle tissue, with average trophic fractionation values ($\Delta\delta^{13}C$) below ± 1.2 ‰. $\Delta\delta^{13}C$ values were calculated between fish tissue (liver/muscle) and diets for all days (N = 20) and on each sampling day (N = 5). Values are given in ‰ as average $\Delta\delta^{13}C$ (SD) and bold italic numbers indicate significant differences from 0 ‰ (two-sided t-tests, α = 0.01), which were found in liver tissue for Ala, Asx, Glx, Gly, Ser, Tyr and Phe. Differences for those AAs in the liver were between -2.0 to +1.8 ‰ compared to diets and Gly was the only AA in the liver to have positive $\Delta\delta^{13}C$ values. $\Delta\delta^{13}C$ values in muscle tissue are significantly different from 0 ‰ for Ala, Asx, Glx, Ser, Lys and Thr mostly after 90 days and caused by a lack of response in muscle tissue to the dietary isotope shift. An overall exception is His, which shows high $\Delta\delta^{13}C$ values in liver (+8.2 ± 1.2 ‰) and muscle (+ 4.9 ± 1.4 ‰).

$\Delta\delta^{13}C_{Liver\text{-}Diet}$

	All Days		30 Days		60 Days		90 Days		120 Days	
Ala	-0.8	(1.3)	-1.4	(0.9)	***-2.0***	***(0.9)***	0.5	(1.0)	-0.3	(0.9)
Asx	***-0.8***	***(1.0)***	-0.9	(1.1)	-0.6	(0.8)	-0.5	(1.1)	-1.1	(0.9)
Glx	***-0.8***	***(1.1)***	-0.5	(1.0)	-1.5	(0.8)	-0.3	(1.6)	-0.6	(0.7)
Gly	0.6	(1.5)	-1.1	(1.0)	-0.1	(0.8)	***1.8***	***(0.9)***	***1.7***	***(0.7)***
Pro	-0.5	(1.4)	-1.2	(1.5)	-0.8	(0.8)	0.2	(1.8)	-0.1	(1.1)
Ser	***-1.8***	***(1.2)***	***-2.8***	***(1.1)***	-2.2	(1.4)	-1.3	(1.0)	-1.1	(0.7)
Tyr	***-1.2***	***(0.8)***	***-0.7***	***(0.4)***	***-1.0***	***(0.4)***	-1.4	(1.3)	***-1.7***	***(0.5)***
Arg	0.1	(0.7)	0.4	(0.5)	0.2	(0.4)	0.4	(1.0)	-0.5	(0.3)
His	***8.2***	***(1.2)***	***6.8***	***(0.5)***	***8.5***	***(0.9)***	***8.7***	***(1.1)***	***8.7***	***(0.8)***
Lys	-0.1	(0.8)	-0.1	(0.4)	-0.5	(0.4)	0.8	(0.8)	-0.5	(0.6)
Phe	***-1.1***	***(0.9)***	***-1.7***	***(0.6)***	-1.2	(0.7)	-0.1	(0.8)	***-1.7***	***(0.6)***
Thr	***0.9***	***(1.0)***	0.4	(0.7)	0.8	(0.7)	1.3	(1.4)	1.0	(1.0)

$\Delta\delta^{13}C_{Muscle\text{-}Diet}$

	All Days		30 Days		60 Days		90 Days		120 Days	
Ala	***1.0***	***(1.3)***	-0.6	(1.0)	0.7	(0.6)	***2.5***	***(0.3)***	***1.3***	***(0.5)***
Asx	0.5	(1.1)	-0.8	(1.0)	0.3	(0.6)	***1.7***	***(0.5)***	0.8	(0.4)
Glx	0.6	(1.0)	-0.4	(0.9)	0.5	(0.3)	***1.8***	***(0.7)***	0.5	(0.4)
Gly	-0.5	(1.1)	-1.9	(1.1)	-0.4	(0.5)	0.1	(0.5)	0.1	(0.8)
Pro	-0.6	(1.0)	-1.4	(0.9)	-0.6	(0.7)	-0.3	(0.8)	-0.1	(1.0)
Ser	0.9	(1.5)	-1.0	(1.1)	***1.9***	***(0.6)***	***2.0***	***(0.6)***	0.6	(0.8)
Tyr	***-1.5***	***(1.0)***	-2.4	(1.2)	***-1.5***	***(0.6)***	-1.3	(0.9)	-0.7	(0.5)
Arg	-0.2	(0.8)	-1.0	(1.0)	-0.1	(0.8)	0.2	(0.6)	0.1	(0.2)
His	***4.9***	***(1.4)***	***3.8***	***(1.1)***	***4.9***	***(0.7)***	***6.6***	***(0.9)***	***4.4***	***(1.1)***
Lys	0.2	(0.9)	-0.8	(0.9)	-0.1	(0.3)	***1.3***	***(0.4)***	0.3	(0.3)
Phe	***-0.7***	***(0.9)***	***-1.7***	***(0.8)***	-0.9	(0.6)	0.0	(0.4)	-0.3	(0.2)
Thr	0.6	(1.3)	-0.6	(1.0)	1.2	(0.9)	***2.0***	***(0.7)***	-0.2	(0.5)

Table 3.5: Pooled NEAAs in the liver show negative trophic fractionation values around -0.7 ‰ compared to trophic fractionation close to zero for EAAs in the liver and both NEAAs and EAAs in muscle. All AAs were divided and pooled in NEAAs and EAAs prior analysis. Two-way ANOVA was conducted on $\Delta\delta^{13}C$ with NEAA/EAAs and tissue (liver, muscle) as factor, followed by Tukey-tests. Significant differences from ANOVA and Tukey-tests ($\alpha = 0.01$) are marked in bold italic. His was excluded from the analysis because it showed high fractionation of unknown origin. No differences in trophic fractionation were found in general between NEAAs and EAAs ($F_{1, 435} = 5.6$, $p = 0.019$), but there was a significant interaction between tissues and NEAA/EAAs on $\Delta\delta^{13}C$ values ($F_{1, 435} = 9.4$, $p = 0.002$). The interaction is caused by negative $\Delta\delta^{13}C$ values (-0.7 ± 1.3 ‰) of $NEAA_{Liver}$ compared to $\Delta\delta^{13}C$ values of -0.1 ± 1.1 ‰, 0.0 ± 1.4 ‰ and 0.0 ± 1.1 ‰ in EAA_{Liver}, $NEAA_{Muscle}$ and EAA_{Muscle}, respectively.

Sample Statistics	**N**	**Avg $\Delta\delta^{13}C$**	**SD**
Liver	220	-0.5	1.3
Muscle	220	0.0	1.3
NEAA	280	-0.3	1.4
EAA	160	-0.1	1.1
$NEAA_{Liver}$	140	-0.7	1.3
EAA_{Liver}	80	-0.1	1.1
$NEAA_{Muscle}$	140	0.0	1.4
EAA_{Muscle}	80	0.0	1.1
two-way ANOVA	**DF**	**F-value**	**p-value**
Tissue	1	10.0	***0.002***
NEAA/EAA	1	5.6	0.019
Interaction	1	9.4	***0.002***
Error	435		
Tukey-Test	**$\Delta\delta^{13}C$**	**SE**	**p-value**
Muscle - Liver	0.5	0.1	***0.000***
EAA - NEAA	0.3	0.1	0.019
EAA_{Liver} - $NEAA_{Liver}$	0.7	0.2	***0.001***
$NEAA_{Muscle}$ - $NEAA_{Liver}$	0.8	0.2	***0.000***
$NEAA_{Muscle}$ - EAA_{Liver}	0.1	0.2	0.941
EAA_{Muscle} - $NEAA_{Liver}$	0.7	0.2	***0.001***
EAA_{Muscle} - EAA_{Liver}	0.0	0.2	1.000
EAA_{Muscle} - $NEAA_{Muscle}$	-0.1	0.2	0.959

Table 3.6: Measurements of RM and AA standards on the LC-IRMS to calibrate and validate sample measurements. Five international RM were measured via LC-IRMS and the measured $\delta^{13}C$ values (N = 6) were calibrated with the AA in-house standards. Differences between the calibrated and true $\delta^{13}C$ values were negligible except for USGS41, which showed conversion of Glu to pyroglutamic acid. SD of continuous AA standard measurements on the LC-IRMS during the prolonged measurement periods (N = 34, 17 and 20, respectively) were used to assure equal system and method performance.

RM	**True $\delta^{13}C$**		**Measured $\delta^{13}C$**		**Calibrated $\delta^{13}C$**		**$\Delta\delta^{13}C$**
	Avg	SD	Avg	SD	Avg	SD	
Ala	-17.93	0.02	+14.82	0.25	-17.39	0.50	0.54
USGS41	+37.63	0.05	+72.70	0.29	39.58	0.42	1.95
Gly	-40.81	0.04	-8.49	0.19	-40.73	0.39	0.08
Phe	-11.20	0.02	+22.46	0.13	-10.57	0.49	0.63
Pro	-12.47	0.01	+20.98	0.16	-12.31	0.48	0.16

AA	**Calibrated $\delta^{13}C$**		**LC-IRMS (N=34)**		**LC-IRMS (N=17)**		**LC-IRMS (N=20)**	
	Avg	SD	Avg	SD	Avg	SD	Avg	SD
Asx	-22.54	0.05	10.7	0.2	10.9	0.1	10.9	0.2
Glx	-13.97	0.04	19.2	0.3	19.5	0.2	19.6	0.3
Ser	-24.74	0.03	8.0	0.3	8.0	0.2	8.3	0.2
Thr	-42.48	0.03	20.5	0.6	20.0	0.4	21.8	0.2
Gly	-10.76	0.04	-10.2	0.3	-10.0	0.4	-10.0	0.2
Ala	-19.41	0.04	12.8	0.4	11.8	0.6	11.5	0.5
Pro	-10.38	0.03	22.9	0.5	24.5	0.6	24.6	0.5
Val	-12.21	0.04	19.3	0.3	19.4	0.3	20.2	0.4
Tyr	-22.86	0.03	10.1	0.3	10.2	0.2	10.3	0.3
Lys	-12.86	0.03	19.8	0.3	20.0	0.2	20.2	0.6
His	-15.88	0.02	16.9	0.4	17.2	0.2	17.2	0.4
Phe	-12.12	0.04	20.9	0.5	21.2	0.4	21.1	0.3
Arg	-12.29	0.03	21.1	0.4	21.4	0.4	21.2	0.3

Chapter 4: Carbon stable isotope analysis of amino acids and glucose: A new technique to study nutrient flow and conversion in host-parasite systems.

Authors:

Tobias Hesse[1], Milen Nachev[2,3], Shaista Khaliq[1], Maik A. Jochmann*[,1,3], Frederik Franke[4,6], Jörn P. Scharsack[4,5], Joachim Kurtz[4], Bernd Sures[2,3], Torsten C. Schmidt[1,3]

Affiliations:

1. Instrumental Analytical Chemistry, University of Duisburg-Essen, Universitätsstr. 5, 45141 Essen, Germany
2. Aquatic Ecology, University of Duisburg-Essen, Universitätsstr. 5, 45141 Essen, Germany
3. Centre for Water and Environmental Research, University of Duisburg-Essen, Universitätsstr. 5, 45141 Essen, Germany
4. Institute for Evolution & Biodiversity, University of Münster, Hüfferstr. 1, 48149 Münster, Germany
5. Present address: Thünen Institute of Fisheries Ecology, Herwigstr. 31, 27572 Bremerhaven, Germany
6. Present address: Bavarian State Institute of Forestry, Hans-Carl-von-Carlowitz-Platz 1, 85354 Freising, Germany

Adapted with permission from: T. Hesse, M. Nachev, S. Khaliq, M. A. Jochmann, F. Franke, J. P. Scharsack, J. Kurtz, B. Sures, T. C. Schmidt, *Carbon stable isotope analysis of amino acids and glucose: A new technique to study nutrient flow and conversion in host-parasite systems,* Submitted to Scientific Reports, 2022.

4.1 Abstract

As knowledge about the ecological importance of parasites is increasing in recent years, stable isotope analysis emerged as a powerful tool for investigating host-parasite relationships. Limitations in typical bulk stable isotope approaches regarding nutrient sources and conversion from host to parasite can be overcome by analyzing the stable isotope signatures of individual compounds. We measured the carbon isotope composition of thirteen individual amino acids and glucose in the cestode *Schistocephalus solidus* and in liver and muscle tissues of its second intermediate host, the three-spined stickleback (*Gasterosteus aculeatus*), over the course of 90 days in a controlled infection experiment. Linear regressions of $\delta^{13}C$ values over time were similar between parasite and host liver, which indicates that the parasite assimilates nutrients from sources closely connected to the liver metabolism of its host. This was further confirmed by lower trophic fractionation of the essential amino acids arginine and histidine between parasite and liver tissue ($\Delta\delta^{13}C$ = 0.2 ± 0.7 ‰ and -0.1 ± 1.9 ‰) compared to muscle ($\Delta\delta^{13}C$ = 1.0 ± 0.8 ‰ and 1.9 ± 1.4 ‰). Carbon isotope signatures of glucose in the parasite showed similar linear regressions over days post infection compared to the glucogenic amino acids alanine, asparagine and glutamine and an isotopic offset of -2 to -3 ‰, indicated conversion of these compounds to glucose to accumulate large glycogen storages for maturation and reproduction. Trophic fractionation between parasite and host liver was highest for glycine, serine and threonine ($\Delta\delta^{13}C$ = -2.5 ± 1.3 ‰, 3.8 ± 1.7 ‰ and 2.3 ± 1.3 ‰) and could be interpreted as extensive conversion of threonine and serine to glycine to fuel parasitic growth through one-carbon metabolism. A comparison of $\Delta\delta^{13}C$ patterns between infected and uninfected sticklebacks showed tendencies of higher trophic fractionation of amino acids in infected individuals, which could be related to increased metabolic activities and modulation of immunometabolism due to parasitic infection. Our results show that compound-specific stable isotope analysis has unique opportunities to study host and parasite physiology.

4.2 Introduction

Parasites are ubiquitously present in our environment and contribute high amounts of biomass to ecosystems, rivaling that of top predators [149, 150]. They are major parts of ecological food webs [151-153] and can account for substantial energy and carbon transfer [154, 155]. A key difference between parasites and predators is that parasites only interact with one other individual (host) during a single life stage, and that this interaction usually does not result in the death of its host [156]. The nutrients that the parasite acquires is therefore only derived from one organism, and since they can occupy specific tissues or organs, this limitation can be extended in many cases to, e.g., only muscle, blood or dietary nutrients from the gut or intestines of its host. Ecologists struggle to incorporate parasites in their studies because they are difficult to observe and sampled in nature, but ignoring parasites will lead to false assumptions in terms of structure, density, resistance to stressors and energy flow of environments [157].

One well-studied host-parasite model system is the cestode *Schistocephalus solidus* and its specific intermediate host, the three-spined stickleback (*Gasterosteus aculeatus). S. solidus* is an endoparasite with a complex life cycle, in which the stickleback represents the second intermediate host harboring the plerocercoid stage inside of its body cavity. The plerocercoid avoids the host's immune system and grows substantially in size [158, 159]. During this time, huge amounts of glucose are built and stored as glycogen inside the parasite, which are used later for maturation and reproduction [160, 161]. The cestode manipulates the stickleback's behavior [162, 163] to increase transmission to the final host, usually a fish-eating bird. Based on techniques for culturing the parasite in vitro and infecting sticklebacks experimentally, *S. solidus* has been extensively used to investigate host parasite-interactions such as immune response, reproductive development, effects on host behavior and movement abilities [158, 163-168].

A recent review highlights the importance and usefulness of stable isotope analysis (SIA), which has been recognized as a powerful tool over the last decade to gain insights into the energy and nutrient exchange between parasite and host [169]. In SIA, isotope signatures of an element are measured as the ratio of heavy to light isotopes and referenced to an international standard of known isotopic composition, leading to the widely used δ-value, expressed in per mil (‰). Biochemical reactions tend to discriminate against the heavier isotope, resulting in isotope fractionations where, in comparison to the external supply,

the instantaneously built product is isotopically depleted (the ratio of heavy to light isotope is lower) and the remaining substrate gets isotopically enriched (the ratio of heavy to light isotope is higher) [170]. The initial carbon isotope signatures in environments are fixed by primary producers, mainly plants and microorganisms, but also vary according to the exact mechanisms employed by these organisms. In water bodies, e.g., $\delta^{13}C$ values can differentiate between pelagic and littoral sources because baseline values of littoral food webs are isotopically ^{13}C-enriched compared to pelagic food webs [171]. When nutrients then traverse through a food chain, their overall isotope signatures tend to increase per level of trophic transmission, which is most apparent for nitrogen with an average increase in $\delta^{15}N$ by 3 – 4 ‰ of consumer tissue compared to its diet, but also to a smaller extent for carbon with an average increase of <1 ‰ [86]. The exact metabolic reason for trophic fractionation is still not fully understood, but the most likely explanation is that conversion and catabolism of nutrients for energy production leads to mineralization and excretion of isotopically depleted end-products (e.g., CO_2 or urea), whereas the remaining isotopically enriched substrates are then measured in tissue samples. It is worth noting, however, that variations in trophic fractionation can occur between species and a universal trophic fractionation factor is most likely not adequate [172]. Furthermore, *de-novo* synthesis of compounds like non-essential amino acids (NEAA) from other cell compartments can significantly contribute to their carbon isotope signature and lead to different patterns of trophic fractionation depending on dietary composition [92, 93, 95, 97, 173].

Measurements can be either done from whole sample materials in bulk stable isotope analysis (BSIA) or, due to advances in recent years in the coupling of isotope ratio mass spectrometers (IRMS) to chromatographic separation techniques, from individual compounds in compound specific isotope analysis (CSIA). There are major advantages of using isotope ratios of single constituents compared to bulk tissue. One important shortcoming of BSIA is that the isotope signature of bulk tissue can be confounded by variations in baseline values across space and time by primary producers, which complicates the interpretation of isotope values on higher trophic levels. CSIA can overcome this shortcoming by measuring isotope signatures of different compound classes. The isotope signature of, e.g., essential amino acids (EAA), due to their nature to traverse food chains isotopically mostly unchanged, then represents baseline values of primary producers and dietary sources in a higher trophic organism and can be directly

compared to the isotope signature of NEAA to estimate origin of resources and nutrient utilization on different diets in a variety of research fields [49, 51, 56, 83, 85, 95, 99, 174-177].

The transfer and conversion of nutrients within host-parasite systems is not fully known and CSIA can give valuable insights and elucidate information hidden to regular BSIA. The aim of this study was to 1) determine the nutrient source of the parasite within the host organism, 2) investigate the origin of glucose storages for maturation and 3) compare trophic fractionation between infected and uninfected control sticklebacks from an earlier study [178]. We therefore measured the carbon stable isotope signature of thirteen individual AAs and glucose of the cestode *S. solidus* in addition to muscle and liver tissue of its second intermediate host, the three-spined stickleback, in a controlled infection experiment over the course of 90 days post infection (dpi). We are the first to apply CSIA of carbon to examine host-parasite relationships and our overall goal is not only to refine our understanding of nutrient flow and conversion, but also to outline promising metabolic pathways to stimulate future research.

4.3 Materials and methods

4.3.1 Infection experiment

The infection and breeding experiments were carried out in accordance with the local veterinary and animal welfare authorities under the project number 87.51.04.2010.A297. Three-spined sticklebacks were collected from a brook (Ibbenbürener Aa, 52°17'33.11"N, 7°36'46.48"E, North-West Germany) and held in 14 L tanks (VewaTech, Germany) at 18 °C with recirculating water. Light/dark cycles were set to 15/9 h and sticklebacks were fed daily with red mosquito larvae (Chironomidae).

Larval parasites were produced by *in vitro* breeding of adults according to established methods [179, 180], replacing the bird host by *in vitro* culture allowing for reproduction of the adult cestodes. The released eggs were washed, stored in tap water at 4 °C and incubated for three weeks at 20 °C in the dark. The hatching of free living coracidia was initiated by illumination for 3 h, followed by 8 h in the dark and again illumination for 2 h. Single coracidia were transferred to wells containing one single copepod (*Macrocyclops*

albidus) in 2 mL tap water. Copepods were checked after two weeks for the presence of *S. solidus* procercoids.

Sticklebacks for the infection experiments were eight months old and tagged individually with visible implant elastomer tags (Northwest Marine Technologies, USA) three weeks before parasite exposure. 144 sticklebacks in total were divided into twelve 14 L tanks, each containing a group of 12 individuals, and fasted 72 h prior to exposure before they were transferred to glass jars filled with 300 mL tank water. On the next day, 3 sticklebacks per group were exposed to an uninfected copepod (sham-exposed) and 9 sticklebacks were exposed to an infected copepod, containing a three-week-old procercoid. The water was sieved after 24 h to confirm ingestion of the copepod and sticklebacks were then returned to the water tanks.

36 Sticklebacks were sampled 30, 60, 90 and 120 dpi each and fasted for 72 h prior to sampling. Ingestion of an infected copepod does not always lead to parasitic infection (exposed but not infected), and out of the 108 sticklebacks exposed to an infected copepod, 74 individuals were itself infected with the parasite after ingestion. We analyzed five infected and five uninfected (sham-exposed) individuals in this study on each time point. Although sampling was done over a period of 120 days, we only considered samples up to 90 dpi after the start of the experiment. An explanation why the last sampling date was removed is given in the data analysis section. Anesthetization was done with MS 222 (Sigma Aldrich, USA) and sticklebacks were subsequently killed by decapitation. The body cavity was opened and *S. solidus* plerocercoids were removed and washed with MilliQ water. Liver and muscle samples of sticklebacks were collected, and all samples were stored at -20 °C. Five infected sticklebacks (liver and muscle tissue) and their respective parasites were randomly chosen per time point for CSIA, which is an identical number of individuals as in our previous study on sham-exposed sticklebacks.

4.3.2 Sample preparation and CSIA via LC-IRMS

Hydrolysis and sample analysis of individual AAs were carried out analogously to our previous study [178]. In brief, approximately 5 mg sample material were hydrolyzed with 2.5 mL 6 M hydrochloric acid (>99 %, Alfa Aesar, Kandel, Germany) at 110 °C in 5 mL PTFE vials (CEM GmbH, Kamp-Lintfort, Germany) for 24 h. The hydrolysate was filtered (0.2 µm PTFE filter), evaporated to dryness and reconstituted in 1 mL distilled water. CSIA was carried out on a Dionex Ultimate 3000 HPLC Pump (Thermo Fisher Scientific, Bremen,

Germany) coupled to an Isolink Interface and Delta V Advantage mass spectrometer (Thermo Fisher Scientific, Bremen, Germany) with a mixed mode cation exchange column (Primesep A, 2.1 mm ID, 250 mm L, 5 µm particle size) from SIELC. A mix of in-house standards (L-Alanine, L-Glutamic acid, USGS 64, USGS 66, L-Phenylalanine, L-Proline and L-Valine, ordered from Arndt Schimmelmann, Department of Earth and Atmospheric Sciences at Indiana University, Bloomington, IN, USA) with a concentration of 100 mgL^{-1} for each amino acid was regularly measured in between sample runs and used to directly assign final isotope values on the VPDB scale.

Sample preparation for glucose analysis was carried out by acid hydrolysis of 5 - 10 mg sample material in 5 mL of 1.1 M sulfuric acid at 120°C for 1 hour [181]. The hydrolysate was filtered (0.2 µm PTFE filter, WICOM, Germany) and neutralized to pH 6-7 by adding $Ca(OH)_2$ and $CaSO_4$. The samples were stored overnight at -4 °C for precipitation and filtered again. Chromatographic separation of glucose was achieved with an ion-exchange column (Rezex™ RCM-Monosaccharide, 7.8 * 300 mm, 8 µm, Phenomenex, Germany) and pure Milli-Q water as eluent. Flow rate was set to 400 $\mu Lmin^{-1}$ and the column was heated to 80 °C. While direct stable isotope measurements of glucose from muscle or liver tissue were not feasible, the abundance of glucose in the parasite was sufficient for direct injections of 10 µL sample volume and $\delta^{13}C$ measurements via LC-IRMS.

4.3.3 Data analysis

Isotope data was analyzed using Excel from Microsoft Office 365 ProPlus (Microsoft, Redmond, Washington, USA), Origin 2019 version 9.60 (OriginLab, Northampton, Massachusetts, USA) and Matlab R2021a (MathWorks Inc., Natick, Massachusetts, USA) with the PLS_Toolbox suite (Eigenvector Research Inc., Manson, WA). Isotope data are reported as mean $\delta^{13}C$ values for each AA and glucose on individual time points on the VPDB scale in per mill (‰) with its corresponding standard deviation (SD) in the supplementary material (**Table 4.1**, **Figure 4.3**). Data was tested for normality with Kolmogorov-Smirnov-Tests and by Brown-Forsythe tests ($\alpha = 0.05$) to check for equality of group variances.

We used linear fits and F-tests between slopes of the regression line to investigate changes in $\delta^{13}C$ values of individual AAs and tissues on a time series. F-tests were conducted between all sample tissues and additionally pairwise to investigate differences between individual sample tissues (liver vs. muscle, muscle vs. parasite, etc.). We

measured a noticeable shift in dietary $\delta^{13}C$ values of individual AAs over time in the same experimental design for uninfected fish samples [178], but the shift was not linear over the complete period (**Table 4.2**). $\delta^{13}C$ values of dietary samples decreased by approximately -2 ‰ between 30-60 and 30-90 dpi, but the last shift between 90-120 dpi was positive and $\delta^{13}C$ values increased on average by +2 ‰. To approximate data by a linear fit for fish and parasite tissue, we removed the last time point from the analysis and only analyzed changes in $\delta^{13}C$ values between the first 90 dpi.

We calculated average trophic fractionation between parasite and host liver/muscle tissue over 90 dpi (n = 15) and tested the significance with two-sided t-tests against zero (DF = 14, $\alpha = 0.01$). We chose to also exclude the last sampling date at 120 dpi so we can consider the slopes of linear regression during the discussion, as trophic fractionation of AAs with differences in regression slopes between tissues are not directly comparable.

We further compared trophic fractionation of liver and muscle tissue from infected to uninfected control sticklebacks in a multivariate approach using ANOVA simultaneous component analysis (ASCA). Data of uninfected sticklebacks and dietary samples were taken from our earlier study using the same experimental design [178]. Tissues and time points were set as independent variables (factors) and AA $\Delta\delta^{13}C_{Fish\text{-}Diet}$ values of infected and uninfected sticklebacks as variables. Multivariate data analysis was used because the differences in trophic fractionation were small but consistent for many AAs, which makes a multivariate approach more powerful compared to a univariate analysis by, e.g., regular ANOVA. The analysis was performed without data pre-processing and with 1000 permutations.

4.4 Results

4.4.1 Changes in AA $\delta^{13}C$ values over 90 days after infection

$\delta^{13}C$ values of AAs overall ranged between -25 and 0 ‰ on the VPDB scale, with patterns of lowest $\delta^{13}C$ values between -25 and -20 ‰ for Phe, Tyr and Val and highest $\delta^{13}C$ between -10 and 0 ‰ for Ser and Gly (**Table 4.1**).

Adjusted coefficients of determinations (Adj. R^2) of linear regressions from dietary $\delta^{13}C$ values between 30 and 90 dpi were higher than 0.73 (DF = 7) for any individual AA. Slopes of regression curves were between -0.069 and -0.028 ‰/dpi with significant differences

from zero (one-way ANOVA, DF = 1, 7, $p \leq 0.002$), showing negative linear relationships between $\delta^{13}C$ values of AAs and dpi (**Table 4.2**) in the used food source.

In parasite and liver tissues, analysis of linear regression showed that $\delta^{13}C$ values of the NEAAs Ala, Asx, Glx, Tyr and the EAAs Arg and Lys decreased over time (one-way ANOVA of regression slopes against zero, DF = 1, 13, $p < 0.01$), with significant negative slopes between -0.02 and -0.06 ‰/dpi (DF = 13, **Table 4.2**). Comparing the regression slopes of individual AAs between sample tissues showed that Ala, Asx, Glx, Tyr, Arg and Lys were significantly different between tissues (F-test, DF = 2, 39, $p < 0.01$, **Table 4.3**). For Ala, Arg and Lys, those differences were observed between host liver and muscle tissue. Differences in linear regressions between host muscle and parasite tissue were seen for Asx, Glx and Tyr (pairwise F-test, DF = 1, 26, $p \leq 0.001$, **Table 4.3**) and for Ser between parasite and liver tissue (F-test, DF = 1, 26, $p = 0.009$, **Table 4.3**).

4.4.2 $\delta^{13}C$ values of Glucose

The supply of glycogen that *S. solidus* acquired had a carbon isotope signature between -15 and -18 ‰ (**Table 4.1**), with a linear decrease of -0.060 ± 0 007 ‰/dpi (Adj. $R^2 = 0.84$, **Table 4.2**) in the regression slope between 30 and 90 dpi, which was significantly different from zero (one-way ANOVA, DF = 1, 13, $p \leq 0.001$, **Table 4.3**). AAs with a comparable linear decrease in their $\delta^{13}C$ values are Ala and Glx in host liver (-0.054 ± 0.006 and -0.044 ± 0.011 ‰/dpi) and Asx, Glx and Tyr in parasite tissue (-0.048 ± 0.00, -0.050 ± 0.008 and -0.045 ± 0.007 ‰/dpi). Ala, Asx and Glx additionally had similar carbon isotope signatures between -10 and -15 ‰, with glucose in parasite tissue being isotopically ^{13}C-depleted by -2 to -3 ‰ in comparison.

4.4.3 Trophic fractionation between parasite and host tissues

We calculated average trophic fractionation ($\Delta\delta^{13}C$ ± SD) between parasite and host muscle/liver tissue over 90 dpi (n = 15, **Figure 4.1**). $\Delta\delta^{13}C$ values were tested with two-sided t-tests against zero and significant differences are marked with an asterisk (DF = 14, $p < 0.01$). Average values and statistical data are reported in **Table 4.4**. Trophic fractionation was not measurable for almost all EAAs except Thr between parasite and liver tissue, whereas $\Delta\delta^{13}C$ values of Arg and His were additionally significant between parasite and muscle. NEAAs showed more often fractionation between parasite and liver tissue, with Glx and Ser being isotopically ^{13}C-enriched, whereas Gly and Pro were ^{13}C-depleted in the parasite compared to host liver. Note that although $\Delta\delta^{13}C$ values of Asx

and Glx between parasite and muscle tissue were close to zero, both NEAAs showed very different changes of $\delta^{13}C$ values over time points and are therefore not directly comparable. There was no universal trend of either positive or negative trophic fractionation between parasite and host liver, with Asx, Ser and Thr having positive $\Delta\delta^{13}C$ values, whereas Gly and Ser showed the opposite trend of negative trophic fractionation.

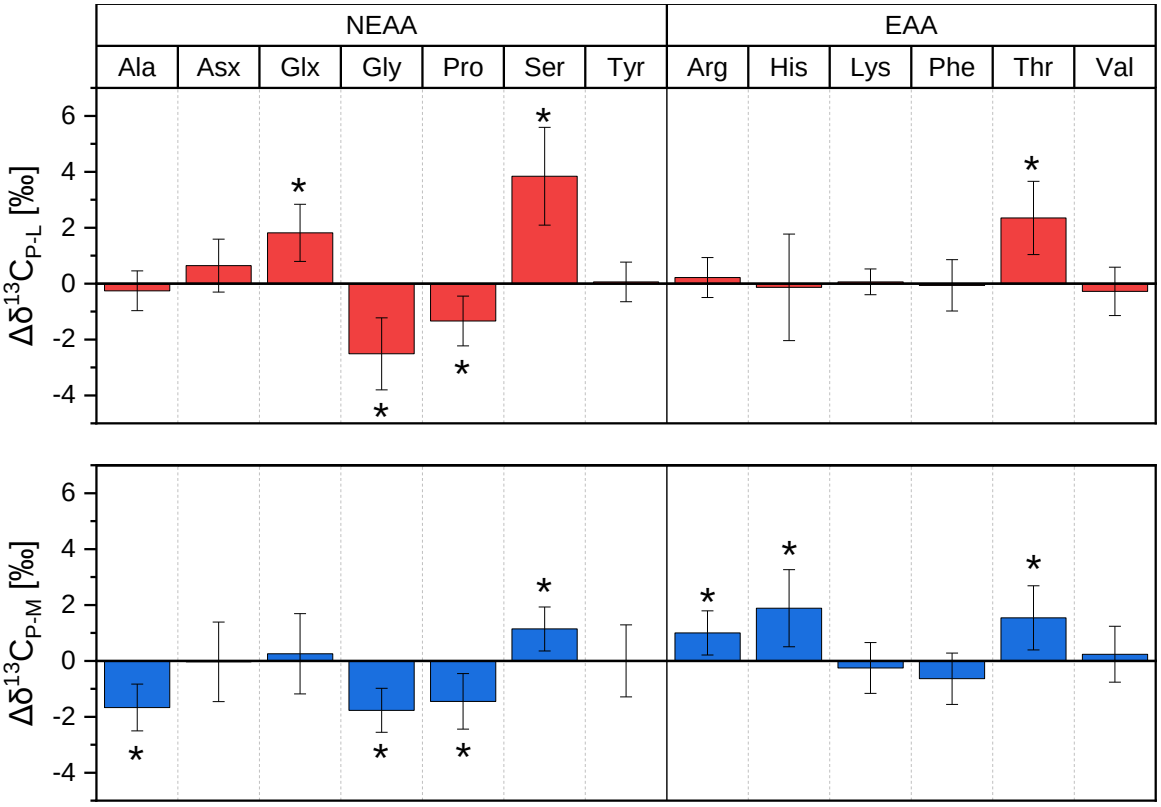

Figure 4.1: Average trophic fractionation values (n = 15) ± SD of individual AAs between parasite and host tissue over 90 dpi. EAAs showed no trophic fractionation between parasite and host liver except for Thr, whereas significant $\Delta\delta^{13}C$ values between the parasite and muscle tissue of the EAAs Arg, His and Thr were observed. $\Delta\delta^{13}C$ values were negative for the NEAAs Gly and Pro and positive for Ser. Note that trophic fractionation of Asx and Glx between the parasite and muscle tissue seemed low and not significant, but regression slopes of $\delta^{13}C$ values from Asx and Glx over time were different between the two tissues and are therefore not directly comparable. Asterisks (*) indicate significant differences of average $\Delta\delta^{13}C$ values from zero (two-sided t-tests, DF = 14, $p < 0.01$)

4.4.4 Trophic fractionation patterns between infected and uninfected sticklebacks

$\Delta\delta^{13}C$ values of individual AAs between infected and uninfected control sticklebacks did not show any differences between liver or muscle tissues in univariate analysis except for Thr (**Table 4.5**), which was significantly lower in the liver of infected fish (-1.0 ± 1.8 ‰) compared to uninfected liver samples (0.8 ± 1.0 ‰). We therefore performed ASCA on $\Delta\delta^{13}C$ values of AAs as a more powerful multivariate approach. Time points had the highest effect (30.78 %) on system variance, while tissue type accounted for 26.78%. To

investigate fractionation patterns between infected and uninfected individuals, we will focus on tissue type (factor 2). A biplot with sample scores and AA loadings on PC1 and PC2 (**Figure 4.2**) shows separate clusters of liver and muscle samples, separated by differences in their $\Delta\delta^{13}C$ values by mainly His and Ser with loadings of -0.5 and 0.64, respectively. Liver scores on PC1 are negative and center around mean values of -2.6 ± 1.3 for uninfected and -2.0 ± 0.7 for infected samples, whereas muscle scores are positive with mean values of 2.3 ± 0.6 for both uninfected and infected individuals. PC2, however, shows differences in sample scores between infected and uninfected samples for both liver and muscle tissue. Uninfected samples on PC2 have positive scores for liver (1.1 ± 1.3) and muscle (0.9 ± 1.3) tissue, whereas infected samples have negative scores for liver (-1.3 ± 0.9) and muscle (-0.7 ± 1.1) tissue.

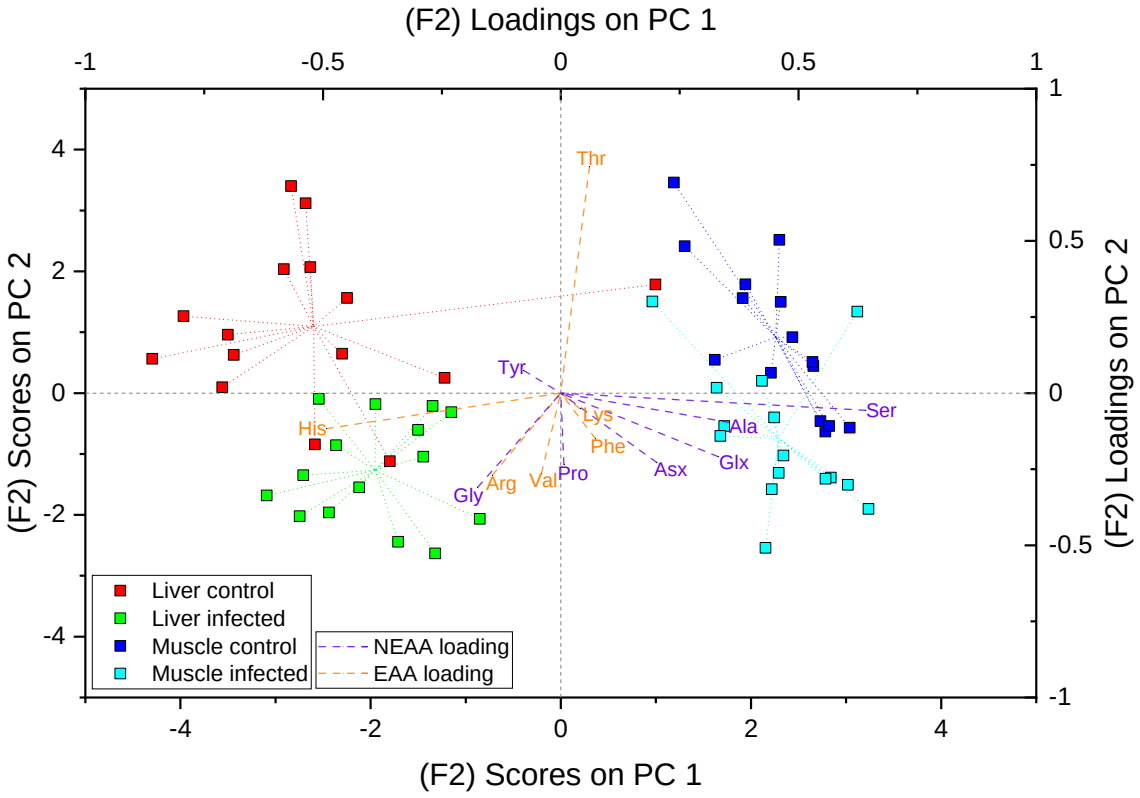

Figure 4.2: Multivariate analysis of $\Delta\delta^{13}C$ values shows higher trophic fractionation of most individual AAs in liver and muscle tissue of infected sticklebacks compared to uninfected control individuals on the same diet. PC1 of the first factor (tissue) from ASCA analysis separates muscle and liver tissue of the infected and control individuals, whereas PC2 shows separate clusters of infected and control liver and muscle tissues.

The separation is not as clear as between liver and muscle tissues and there are some overlapping samples. Eleven out of the thirteen measured AAs have negative loadings on PC2, with only Thr and Tyr having positive loadings. The influence of His, Ser, Tyr and Lys might be miniscule due to their loadings being close to zero on PC2, but the results show a universal trend of tissues from infected sticklebacks having higher trophic fractionation values of carbon for most AAs except Thr, which shows the opposite trend of lower $\Delta\delta^{13}C$ values in both muscle and liver tissue compared to uninfected individuals on the same diet.

4.5 Discussion

We measured the carbon isotope signature of 13 individual AAs of the cestode *S. solidus* and liver and muscle tissue of its second intermediate host, the three-spined stickleback. Although we sampled over the course of 120 days, we only considered samples up to 90 dpi to have a linear shift of dietary $\delta^{13}C$ values, which showed a sudden increase after 120 days in comparison to the linear decrease over the first 90 days. Host liver and parasite tissue showed similar linear decreases over 90 dpi for six of the thirteen measured AAs in contrast to more constant isotope signatures of muscle tissue over time.

The sticklebacks used in this infection experiment were reared in parallel to the individuals described in our previous studies [178]. The dietary isotope signature of AAs changed over the course of the experiment and caused a significant shift of $\delta^{13}C$-values in the liver tissue of uninfected control sticklebacks, whereas $\delta^{13}C$-values in muscle tissue remained unaffected. Analogous to uninfected sticklebacks and to earlier bulk isotope studies investigating carbon isotope turnover in different tissue types [105, 182, 183], the liver of infected fish also adapted quickly to the dietary isotope shift. The liver is an essential organ for nutrient metabolism and serves as a modifying and communicating link between the digestive tract of an organism and its peripheral tissues [184]. The parasite, on the other hand, absorbs nutrients from the surrounding body cavity of its host through the tegument [185]. It has been shown in studies using BSIA of carbon and nitrogen that passively feeding parasites do not follow typical trophic fractionation patterns, which makes a direct comparison of bulk isotope signatures between parasite and fish tissues difficult for source allocation. Instead of isotope enrichment, as it is expected in a predator-prey relationship, some gutless helminths such as cestodes and acanthocephalans exhibit lower δ-values for carbon and nitrogen compared to their hosts [24, 186-188]. It is speculated that these parasites feed on reprocessed metabolites, which

are lighter in their isotope signature and might originate from the host's liver and gut metabolism [24, 187]. Recent research on the tapeworm *Schyzocotyle acheilognathi*, which is an adsorptive feeder inside of fish intestines, also points towards nutrients being derived from liver metabolites [187]. Although *S. solidus* does not live inside the gut of its host and has no direct access to liver metabolites, its presence inside the body cavity between liver and gut could enable the parasite to adsorb nutrients from liver excretes. The observed dietary isotope shifts in fish diet and associated change of carbon isotope signatures in stickleback liver and parasite tissue over time support this idea. Comparing the regression slopes showed that especially the isotope signatures of Asx and Glx over time in the parasite do not match the general trend of constant isotope signatures in muscle tissue, and the change over time of parasitic Asx and Glx instead is identical to changes observed in liver tissue. This could be interpreted as a close connection between the nutrients that *S. solidus* assimilates and the hosts liver metabolism. Interestingly, some AAs in parasite and host tissues did not show an overall negative shift over time in their isotope signatures, which was the case for Gly, Pro, Ser, His, Phe and Thr. Slopes of linear regression were either close to zero or showed large variation, such that statistical tests would not indicate significant differences. For example, average regression slopes of Gly in liver and parasite tissue over 90 dpi were -0.021 ‰/dpi for both tissues, but liver tissues had higher uncertainties resulting in no statistically significant difference from zero in contrast to parasite samples. It appears that these AAs do not follow dietary trends on shorter time scales, which in case of NEAAs could indicate *de-novo* synthesis from other compounds like lipids, carbohydrates, and other AAs, but could also stem from catabolism and nutrient conversion associated with isotope fractionation.

The ability of CSIA to identify nutrient sources hinges on differences in isotope signatures between those sources, which are subsequently transferred to higher trophic organisms and visible in compounds which show no or only minor trophic fractionation. Comparing trophic fractionation of EAAs between parasite and host tissue is consequently only useful for resource allocation when there are significant differences in the isotope signatures of EAAs between liver and muscle tissue. Many EAAs did not show such differences between muscle and liver tissue except for His, which had higher $\delta^{13}C$-values in the liver (**Table 4.1**). Unusual fractionation patterns of His between diets and uninfected sticklebacks were already mentioned and discussed in our earlier study [178], where His not only showed high trophic fractionation between uninfected sticklebacks and diets but also

higher trophic fractionation in liver compared to muscle tissue. The same trends were also seen in this study for infected sticklebacks. Average $\Delta\delta^{13}C$ values of His and other EAAs except Thr between parasite and host liver are close to zero, whereas $\Delta\delta^{13}C$ values between parasite and muscle tissue show significant differences for His and additionally Arg. Overall, the similar $\delta^{13}C$ shifts of AAs over time and lower trophic fractionation of EAAs between parasite and liver tissue suggests that nutrient absorption and assimilation in *S. solidus* takes place through liver metabolites and not through sources derived from muscle tissue of its host. We will therefore subsequently focus on isotopic fractionation between parasite and liver tissue to investigate metabolic pathways for nutrient conversion, parasitic growth, and the buildup of glycogen storages for growth and reproduction.

Glycogen is the major macronutrient for cestodes and the glycogen content in *S. solidus* plerocercoids can reach up to 50 % of dry weight [160]. It might be unlikely that the parasite is able to acquire all its glycogen directly from the host and biosynthesis of glucose from other nutrients may be necessary. Interestingly, half of the proteins in the secretome of the parasite show enriched functions for glycolytic processes and gluconeogenesis in addition to cell division [163], which suggests that biosynthesis of glucose might not only happen inside the parasite from assimilated sources, but also outside in the secretome directly from host nutrients. The changes in $\delta^{13}C$ values of glucose in the parasite over time were similar to those of the NEAAs Ala, Asx and Glx, with a constant offset between -2 to -3 ‰. This would fit the idea of enzymatic reactions discriminating against the heavier isotope and inducing isotopic fractionation to lower $\delta^{13}C$ values in the built product. Furthermore, the carbon isotope signature of Ala in liver and parasite tissue showed some striking similarities. Ala itself is an important precursor for gluconeogenesis and can be directly converted to pyruvate via deamination, which is mainly used by organisms to cycle AAs and carbohydrates between tissues [189]. This would indicate that the parasite has access to the alanine-glucose cycle of its host, which results in identical isotope signatures of alanine in parasite and host liver because extensive amounts of nutrients are transferred this way without noticeable fractionation.

The AAs Gly, Pro, Ser and Thr were less affected by the isotope shift over time resulting in no significant slopes in linear regression over 90 dpi. Thr is an essential AA and must be taken up through diets by higher organisms. It has been shown that animals can convert significant amounts of Thr to Gly [190], which is itself convertible to Ser and vice versa

[191]. Thr can also be catabolized extensively to yield Gly and acetate during the growth of single-cell parasites [192]. The enriched carbon isotope signatures of Thr in the parasite could therefore indicate extensive conversion of Thr to produce Gly, which would again match the idea of enzymatic reactions discriminating against the heavier isotope [170]. This could further explain the lower carbon isotope signatures of Gly in parasite tissue compared to both fish muscle and liver, as metabolic processes of Thr catabolism would yield a product which is isotopically depleted compared to the substrate, in addition to the already lower carbon isotope signature of Thr itself.

Gly can be used to produce Ser by reversing the Gly biosynthesis pathway using serine hydroxymethyl transferase. However, carbon isotope signatures of Ser in the parasite are enriched in ^{13}C compared to muscle and liver throughout the experiment, which does not indicate extensive conversion of Gly to Ser. A more dominant pathway for Gly catabolism in animals and plants is the Gly cleavage system to produce 5,10-methylenetetrahydrofolate, which is an important C1 donor in biosynthesis processes [193]. The enriched carbon isotope signature of Ser in the parasite can therefore be interpreted in a similar way to Thr, where Ser is utilized leading to enriched isotope signatures compared to diets.

The important connection of Ser and Gly to one-carbon metabolism for cell growth and proliferation has been described in literature [194, 195] and would be necessary for the parasite to grow substantially in size inside of the stickleback. Biosynthesis of Ser from other compounds might be unlikely to result in higher $\delta^{13}C$, because Ser typically has the highest carbon isotope signature of all AAs [49, 83, 94, 95, 97], possibly due to its high conversion rates in organisms and its metabolic importance for cell proliferation [195]. As seen in our results, the carbon isotope signature of carbohydrates such as glucose in parasite tissue is also depleted compared to Ser, which makes conversion of glucose into Ser unlikely to result in enriched Ser isotope signatures and lipids are typically even more ^{13}C-depleted [196].

Comparing $\Delta\delta^{13}C$ values of AAs between infected and uninfected sham-exposed sticklebacks on the same diet in a multivariate analysis showed a general pattern of higher $\Delta\delta^{13}C$ values in muscle and liver tissue of infected individuals for almost all AAs except Thr and Tyr. Both classes of NEAAs and EAAs contributed to the separation of infected and uninfected tissue scores on PC2 from ASCA, indicating that differences are caused by

a general shift in AA metabolism, independent of their class. Parasites are bound to have severe impacts on host metabolism. It was shown that infected sticklebacks have higher respiration rates by oxygen consumption than uninfected individuals and that the additional oxygen consumption of the parasite does not cover these discrepancies [197]. The nutrients that the parasite accumulates are on account of host organisms, which must fuel parasitic growth in addition to its own survival and energy demands. An increase in trophic fractionation of NEAAs could be explained by increased biosynthesis to maintain cell homeostasis, as recent research showed that biosynthesis of AAs from precursor molecules like pyruvic acids or α-ketoglutaric acid can also lead to ^{13}C-enriched NEAAs like Gly, Ala and Glx [198]. However, this is not the case for EAAs which cannot be synthesized. Increased catabolism of EAAs, like earlier mentioned for Thr in parasite tissue, could be another reason, but there is to date no scientific study that investigated small trophic fractionation values of EAAs due to metabolic reactions. It is certainly true that these compounds remain mostly conservative to trophic fractionation, but there are still metabolic pathways they are involved in that should induce fractionation, even if not to the same extent as for NEAAs.

Furthermore, parasitic infection causes a response of the host's immune system to fight and remove the infection, which is an ongoing burden on the host's energy metabolism. T-Cell activation, e.g., is a metabolically demanding process and requires nutrients such as Ala, Glx, Ser and Arg [199]. Host-parasite systems such as *G. aculeatus* and *S. solidus* showed upregulation of host immune response during later infection stages, when the parasite was already established [159] and would explain their increased fractionation patterns in infected sticklebacks to fuel an ongoing immune reaction. Furthermore, the highest negative loading on PC2 for differentiation of $\Delta\delta^{13}C$ values between infected and uninfected sticklebacks were observed for Gly, which is an important neurotransmitter, anti-inflammatory and immunomodulatory agent [200] preventing apoptosis, sepsis and endotoxic shock. Immunometabolism is a recently emerging field in medical research to understand auto-immune disorders [201] and helminth parasites can modulate the immunometabolism of their hosts and are recognized as models to study immunometabolic principles [165, 202, 203]. It is interesting to see that not only nutrient metabolism, but possibly also immunometabolism might be a subject of investigation for CSIA, giving new prospects for future research.

4.6 Conclusion

We could provide first insights into the carbon isotope signatures and fractionation of individual AAs and glucose between the cestode *S. solidus* and its second intermediate host, the three-spined stickleback. The parasite likely gets most of its nutrients from sources closely related to the liver metabolism of its host, which should be considered as comparing whole body or muscle tissue of host and parasite might give misleading information. The carbon isotope signatures of glucose could be directly measured after hydrolysis due to the high amounts present in parasite tissue, which makes it an ideal candidate along with amino acids for future studies preferably using artificially enriched materials to quantify energy and nutrient flow. We highlighted two promising areas in amino acid and glucose metabolism in that regard, namely biosynthesis of glucose from glucogenic AA precursors, especially Ala, Asx and Glx, and conversion of Thr, Ser and Gly for one carbon metabolism. Higher trophic fractionation of AAs in infected sticklebacks compared to uninfected sham-exposed individuals on the same diet indicate increased catabolism of AAs to either fight off the infection through an ongoing immune response and/or to sustain parasitic growth and cell homeostasis. Our results show that CSIA of carbon bears additional prospects in the study of host-parasite physiology and immunometabolism.

4.7 Appendix to chapter 4

Table 4.1: Average carbon isotope signatures and SD (n = 5) of individual AAs for liver, muscle and parasite tissue after 30, 60, 90 and 120 DPI in ‰ on the VPDB scale.

Tissue	DPI	Ala		Asp		Glu		Gly		Pro		Ser		Glucose	
		Avg	SD	Avg	SD	Avg	SD	Avg	SD	Avg	SD	Avg	SD	Avg	SD
Liver	30	-12.3	0.6	-11.5	0.8	-11.1	1.1	-6.4	0.8	-13.6	0.9	-3.6	1.0	-	-
	60	-14.6	0.4	-12.1	1.1	-13.4	0.5	-6.3	1.4	-13.8	0.9	-4.5	1.4	-	-
	90	-15.5	0.5	-13.6	0.7	-14.3	1.1	-7.3	1.1	-14.6	1.1	-5.1	1.0	-	-
	120	-15.4	0.5	-14.4	1.4	-13.4	0.8	-7.7	1.0	-13.3	1.5	-5.4	1.1	-	-
Muscle	30	-12.3	0.5	-11.8	0.7	-11.2	0.5	-7.1	0.7	-14.3	0.8	-1.5	0.2	-	-
	60	-12.8	0.7	-11.6	0.7	-11.3	0.9	-7.7	0.6	-14.1	1.2	-2.0	0.7	-	-
	90	-13.0	0.4	-11.9	0.7	-11.6	0.6	-7.4	0.8	-13.3	1.0	-1.5	0.8	-	-
	120	-13.6	0.6	-12.3	0.5	-11.9	0.7	-8.7	0.7	-13.6	0.4	-3.3	0.6	-	-
Parasite	30	-13.1	0.2	-10.1	0.6	-9.2	0.7	-9.1	1.1	-15.2	1.3	-0.8	0.7	-14.6	0.9
	60	-15.0	0.5	-12.2	0.3	-11.7	0.2	-8.9	0.4	-15.4	0.6	-0.8	0.6	-16.5	0.3
	90	-15.1	0.1	-13.1	0.4	-12.5	0.8	-9.6	0.9	-15.4	1.1	0.0	0.9	-18.1	0.6
	120	-14.8	0.3	-13.5	0.5	-13.0	0.9	-10.0	0.7	-15.5	0.9	-0.2	0.4	-17.5	0.3

Tissue	DPI	Arg		His		Lys		Phe		Thr		Tyr		Val	
		Avg	SD	Avg	SD	Avg	SD	Avg	SD	Avg	SD	Avg	SD	Avg	SD
Liver	30	-16.8	0.4	-7.9	0.7	-14.8	0.3	-23.9	0.6	-14.0	0.7	-21.2	0.4	-19.7	0.5
	60	-16.8	0.3	-9.8	1.1	-15.7	0.4	-24.0	0.8	-12.0	1.1	-21.5	0.6	-20.4	1.0
	90	-18.6	0.6	-9.4	0.6	-16.8	0.7	-25.1	0.7	-14.2	0.6	-23.0	0.5	-21.6	1.0
	120	-19.5	0.7	-9.5	0.9	-17.8	0.6	-25.5	0.8	-12.4	1.0	-23.3	0.9	-22.3	0.8
Muscle	30	-18.0	0.8	-11.2	1.0	-15.3	0.6	-23.6	0.7	-11.6	1.1	-22.0	0.8	-20.9	0.8
	60	-18.4	0.6	-10.6	0.4	-15.5	0.5	-23.8	0.6	-13.3	0.4	-21.7	0.9	-21.4	1.3
	90	-18.1	0.4	-11.4	0.6	-15.5	0.5	-23.9	0.3	-12.9	0.9	-21.9	0.5	-20.9	1.1
	120	-18.5	0.7	-12.2	0.5	-16.1	0.4	-24.7	0.5	-12.6	0.9	-22.1	0.4	-21.4	0.3
Parasite	30	-16.6	0.4	-9.6	1.1	-14.8	0.4	-24.4	0.7	-11.2	1.1	-20.7	0.6	-20.4	1.0
	60	-17.2	0.3	-9.0	1.2	-15.6	0.3	-24.0	0.8	-10.9	0.8	-21.9	0.6	-20.9	0.7
	90	-17.8	0.6	-8.9	0.9	-16.7	0.7	-24.8	0.5	-11.2	0.9	-22.9	0.8	-21.2	0.5
	120	-18.1	0.5	-8.9	1.0	-16.7	0.5	-24.4	0.9	-10.4	0.7	-22.9	0.5	-21.6	0.9

Table 4.2: Parameters (y-intercept, slope and adjusted coefficient of determination) of linear regression for dietary, liver, muscle and parasite tissue. Standard deviations are given in brackets and p-values are drawn from one-way ANOVA of regression slopes, indicating significant differences from zero. Significance levels for one-way ANOVA and F-tests was set to 0.05 and significant differences are marked bold.

AA	Tissue	Y-Intercept [‰]		Slope [‰/dpi]		p-value (slope = 0)	Adj. R^2
Ala	Diet	-9.5	(0.4)	-0.069	(0.006)	**0.000**	0.947
	Liver	-10.9	(0.4)	-0.054	(0.006)	**0.000**	0.835
	Muscle	-11.9	(0.4)	-0.013	(0.006)	0.035	0.244
	Parasite	-12.5	(0.4)	-0.032	(0.006)	**0.000**	0.673
Asx	Diet	-9.3	(0.2)	-0.052	(0.004)	**0.000**	0.950
	Liver	-10.9	(0.6)	-0.029	(0.009)	**0.007**	0.402
	Muscle	-12.1	(0.4)	0.004	(0.006)	0.572	-0.050
	Parasite	-8.9	(0.4)	-0.048	(0.007)	**0.000**	0.786
Glx	Diet	-9.8	(0.4)	-0.047	(0.006)	**0.000**	0.877
	Liver	-10.4	(0.8)	-0.044	(0.011)	**0.001**	0.523
	Muscle	-11.1	(0.5)	-0.005	(0.007)	0.518	-0.042
	Parasite	-8.2	(0.5)	-0.050	(0.008)	**0.000**	0.753
Gly	Diet	-4.6	(0.2)	-0.046	(0.004)	**0.000**	0.946
	Liver	-5.3	(1.0)	-0.021	(0.015)	0.171	0.073
	Muscle	-6.7	(0.4)	-0.009	(0.007)	0.250	0.031
	Parasite	-7.8	(0.4)	-0.021	(0.006)	**0.006**	0.408
Pro	Diet	-11.5	(0.5)	-0.036	(0.007)	**0.002**	0.743
	Liver	-12.8	(0.5)	-0.018	(0.007)	0.029	0.265
	Muscle	-14.7	(0.7)	0.016	(0.011)	0.182	0.066
	Parasite	-15.4	(0.6)	0.000	(0.009)	0.966	-0.077
Ser	Diet	1.0	(0.3)	-0.060	(0.005)	**0.000**	0.945
	Liver	-2.9	(1.1)	-0.025	(0.017)	0.171	0.073
	Muscle	-1.8	(0.5)	-0.001	(0.008)	0.894	-0.075
	Parasite	-1.3	(0.6)	0.009	(0.009)	0.321	0.005
Tyr	Diet	-18.4	(0.4)	-0.036	(0.007)	**0.002**	0.748
	Liver	-20.4	(0.3)	-0.026	(0.005)	**0.000**	0.681
	Muscle	-22.2	(0.5)	0.004	(0.009)	0.691	-0.063
	Parasite	-19.1	(0.5)	-0.045	(0.007)	**0.000**	0.731

Arg	Diet	-16.1	(0.3)	-0.037	(0.005)	**0.000**	0.888
	Liver	-15.8	(0.5)	-0.024	(0.007)	**0.005**	0.430
	Muscle	-17.8	(0.5)	-0.007	(0.008)	0.397	-0.017
	Parasite	-16.0	(0.3)	-0.019	(0.005)	**0.002**	0.505
His	Diet	-14.3	(0.5)	-0.037	(0.008)	**0.002**	0.734
	Liver	-7.6	(0.6)	-0.026	(0.010)	0.023	0.288
	Muscle	-10.8	(0.5)	-0.006	(0.007)	0.455	-0.030
	Parasite	-9.8	(0.6)	0.008	(0.011)	0.459	-0.031
Lys	Diet	-12.8	(0.3)	-0.050	(0.005)	**0.000**	0.926
	Liver	-14.1	(0.3)	-0.029	(0.005)	**0.000**	0.744
	Muscle	-15.5	(0.3)	0.002	(0.004)	0.729	-0.067
	Parasite	-13.9	(0.3)	-0.029	(0.004)	**0.000**	0.750
Phe	Diet	-20.6	(0.2)	-0.049	(0.004)	**0.000**	0.955
	Liver	-23.6	(0.5)	-0.012	(0.008)	0.127	0.106
	Muscle	-23.4	(0.4)	-0.006	(0.006)	0.387	-0.014
	Parasite	-24.0	(0.6)	-0.004	(0.009)	0.629	-0.057
Thr	Diet	-9.2	(0.2)	-0.053	(0.004)	**0.000**	0.962
	Liver	-12.5	(0.7)	-0.012	(0.010)	0.266	0.024
	Muscle	-11.6	(0.6)	-0.027	(0.009)	0.014	0.336
	Parasite	-11.3	(0.7)	-0.002	(0.010)	0.837	-0.073
Val	Diet	-17.6	(0.4)	-0.028	(0.005)	**0.001**	0.770
	Liver	-18.8	(0.5)	-0.027	(0.008)	**0.005**	0.431
	Muscle	-20.8	(0.6)	-0.003	(0.009)	0.754	-0.068
	Parasite	-20.4	(0.5)	-0.009	(0.006)	0.161	0.080
Glucose	Diet	-		-		-	-
	Liver	-		-		**-**	-
	Muscle	-		-		**-**	-
	Parasite	-12.8	(0.5)	-0.060	(0.007)	**0.000**	0.840

Table 4.3: P-values from F-tests of regression slopes over 90 days after infection between parasite and host tissue. Tests were conducted between all tissues (DF = 2, 39) and pairwise (L vs M, L vs P, M vs P, DF = 1, 26) and significant differences are marked bold ($p < 0.01$). Differences were found for Ala, Asx, Glx, Tyr, Arg and Lys, although slopes for Ala, Arg and Lys only differed between liver and muscle tissue. Asx, Glx and Tyr, in addition, also showed significant differences in regression slopes between muscle and parasite tissue, but not between parasite and liver. The only difference between parasite and liver were observed for Ser, but those were close to the significance level of 0.01 and the overall F-test was above this limit with a p-value of 0.013.

	AA	F-test	L vs M	L vs P	M vs P
NEAA	Ala	**0.000**	**0.000**	0.030	0.016
	Asx	**0.000**	**0.006**	0.198	**0.000**
	Glx	**0.000**	**0.001**	0.795	**0.000**
	Gly	0.813	0.554	0.680	0.840
	Pro	0.111	0.042	0.406	0.211
	Ser	0.013	0.059	**0.009**	0.245
	Tyr	**0.001**	**0.004**	0.390	**0.001**
EAA	Arg	**0.005**	**0.004**	0.198	0.028
	His	0.031	0.109	0.017	0.239
	Lys	**0.004**	**0.004**	0.350	0.017
	Phe	0.262	0.128	0.219	0.872
	Thr	0.395	0.323	0.832	0.158
	Val	0.046	0.024	0.119	0.277

Table 4.4: Average trophic fractionation ($\Delta\delta^{13}C$) of AAs between parasite and liver/muscle tissue of host in ‰ over 90 days after infection. Standard deviations are given in brackets (n = 15). Significant differences of $\Delta\delta^{13}C$ values from zero were tested individually with two-sided t-tests (DF = 14, $\alpha = 0.01$) and are marked bold

	AA	Parasite-Liver			Parasite-Muscle			
		$\Delta\delta^{13}C$ (‰)		t-test	P-Value	$\Delta\delta^{13}C$ (‰)		t-test	P-Value
NEAA	**Ala**	-0.3	(0.7)	-1.41	0.180	-1.7	(0.8)	-7.73	**0.000**
	Asx	0.6	(0.9)	2.62	0.020	0.0	(1.4)	-0.10	0.923
	Glx	1.8	(1.0)	6.87	**0.000**	0.3	(1.4)	0.69	0.500
	Gly	-2.5	(1.3)	-7.55	**0.000**	-1.8	(0.8)	-8.69	**0.000**
	Pro	-1.3	(0.9)	-5.81	**0.000**	-1.4	(1.0)	-5.65	**0.000**
	Ser	3.8	(1.7)	8.50	**0.000**	1.1	(0.8)	5.63	**0.000**
	Tyr	0.1	(0.7)	0.32	0.751	0.0	(1.3)	0.00	0.997
EAA	**Arg**	0.2	(0.7)	1.16	0.266	1.0	(0.8)	4.89	**0.000**
	His	-0.1	(1.9)	-0.28	0.787	1.9	(1.4)	5.28	**0.000**
	Lys	0.1	(0.5)	0.53	0.608	-0.3	(0.9)	-1.08	0.299
	Phe	-0.1	(0.9)	-0.27	0.794	-0.6	(0.9)	-2.69	0.017
	Thr	2.3	(1.3)	6.94	**0.000**	1.5	(1.1)	5.19	**0.000**
	Val	-0.3	(0.9)	-1.25	0.233	0.2	(1.0)	0.92	0.372

Table 4.5: Comparison of trophic fractionation between infected sticklebacks and sham exposed control sticklebacks from our previous study. P-values indicate significant differences between either liver and muscle tissue of infected and uninfected tissues on a significance level of 0.01. Differences were not observed for almost all AAs except Thr between liver tissues, which was significantly depleted in host liver tissue compared to control liver samples.

	$\Delta\delta^{13}C_{Lc\text{-}D}$		$\Delta\delta^{13}C_{Lh\text{-}D}$		p-value	$\Delta\delta^{13}C_{Mc\text{-}D}$		$\Delta\delta^{13}C_{Mh\text{-}D}$		p-value
Ala	-0.9	(1.4)	-0.4	(0.9)	0.258	0.8	(1.5)	1.0	(1.6)	0.821
Asx	-0.7	(1.0)	0.1	(1.0)	0.054	0.4	(1.2)	0.7	(1.6)	0.538
Glx	-0.8	(1.2)	-0.3	(1.0)	0.054	0.6	(1.1)	1.3	(1.2)	0.132
Gly	0.2	(1.5)	0.7	(1.4)	0.356	-0.7	(1.1)	-0.1	(1.3)	0.129
Pro	-0.6	(1.5)	-0.2	(1.1)	0.410	-0.8	(0.9)	-0.1	(1.7)	0.220
Ser	-2.1	(1.2)	-1.6	(1.3)	0.348	1.0	(1.6)	1.1	(1.6)	0.840
Tyr	-1.0	(0.8)	-1.5	(0.6)	0.063	-1.7	(1.0)	-1.5	(1.2)	0.513
Arg	0.3	(0.6)	0.9	(0.6)	0.019	-0.3	(0.9)	0.1	(1.1)	0.272
His	8.0	(1.2)	7.5	(1.1)	0.245	5.1	(1.5)	5.4	(1.1)	0.496
Lys	0.1	(0.8)	0.1	(0.6)	0.955	0.1	(1.0)	0.4	(1.3)	0.521
Phe	-1.0	(1.0)	-0.8	(1.0)	0.710	-0.9	(0.9)	-0.2	(1.2)	0.122
Thr	0.8	(1.0)	-1.0	(1.8)	**0.002**	0.9	(1.4)	-0.2	(1.2)	0.037
Val	-2.1	(0.9)	-1.3	(0.8)	0.021	-2.0	(0.9)	-1.8	(1.3)	0.620

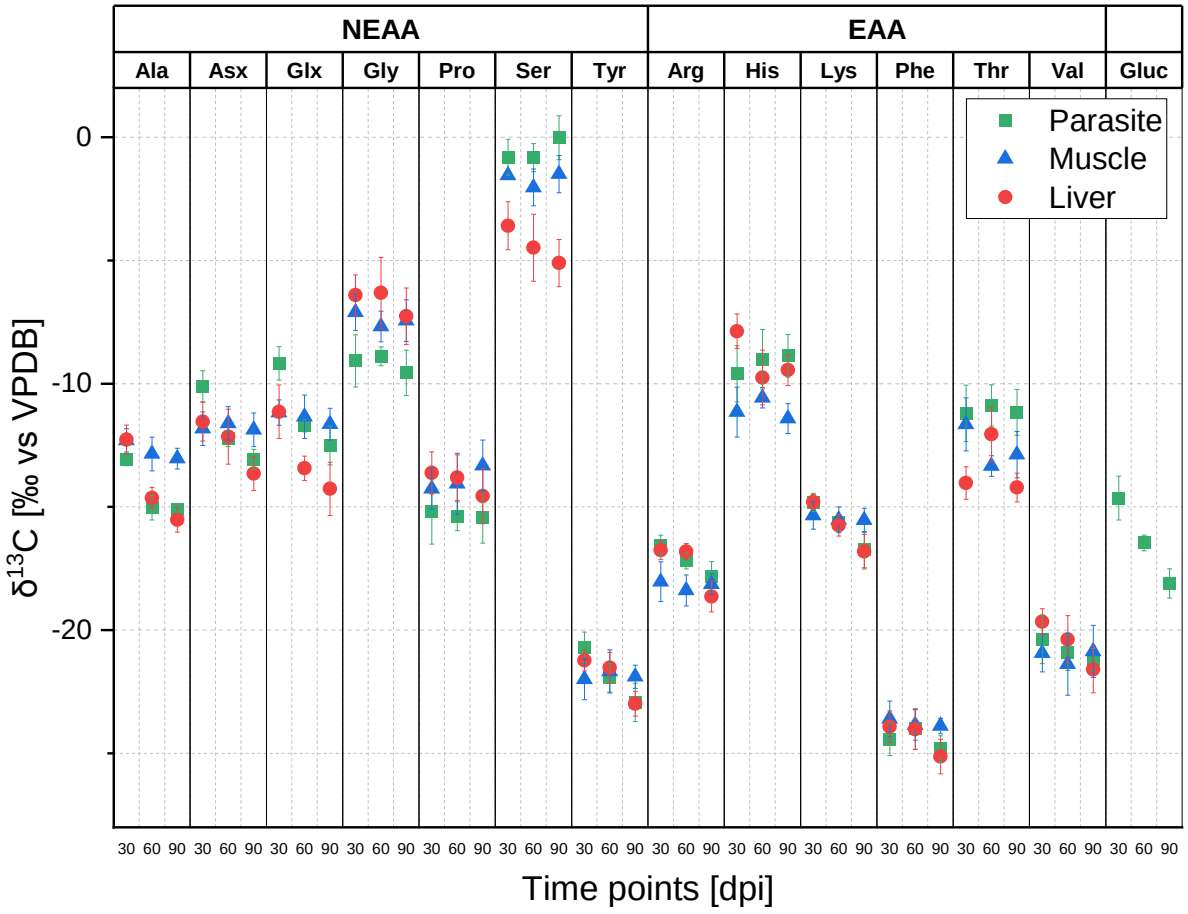

Figure 4.3: Average $\delta^{13}C$ values ± SD (n = 5) of individual AAs and glucose at 30, 60 and 90 dpi for host liver, muscle and parasite samples.

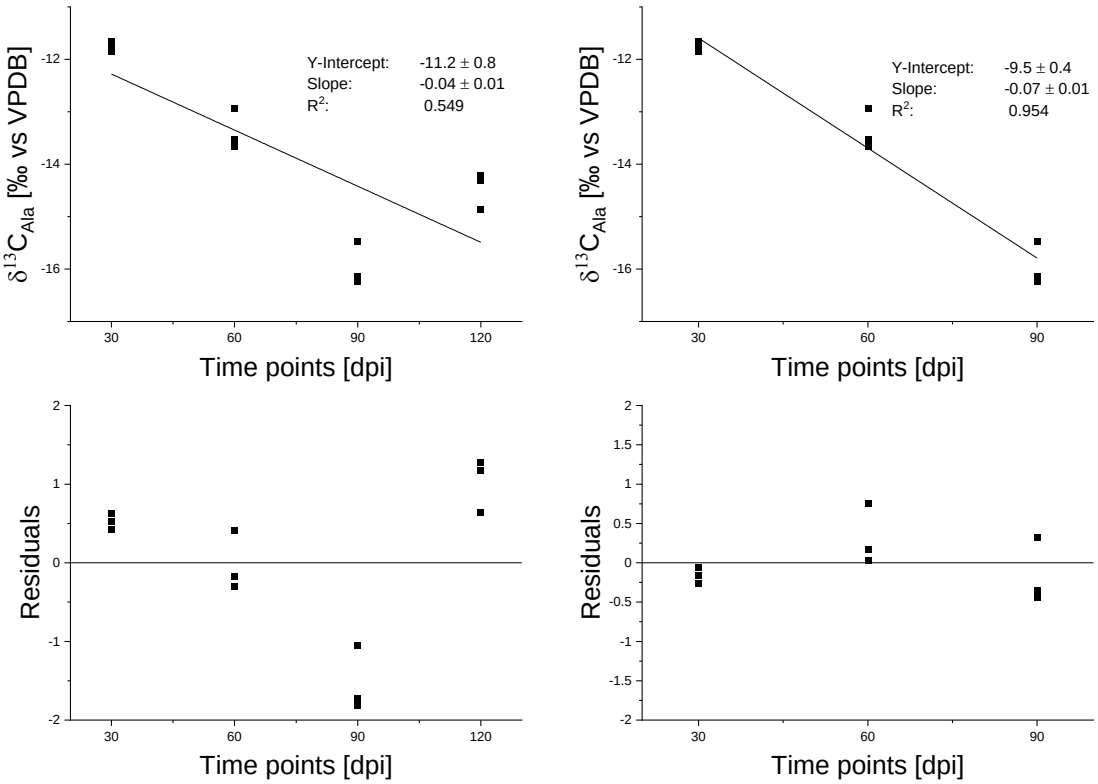

Figure 4.4: Changes of dietary $\delta^{13}C$ values over the first 90 days (right) of the experiment show a linear trend of decreasing $\delta^{13}C$ values, whereas changes of $\delta^{13}C$ over the whole 120 days of the experiment (left) results in a worse approximation by a linear fit due to the sudden increase in $\delta^{13}C$ values after 120 days. Top graphs show $\delta^{13}C$ values and linear fit with y-intercept, slope, and correlation coefficient (R^2), while bottom graphs show the residuals. Data is only shown for Ala as an example and was taken from a previous study [178] utilizing samples of dietary and uninfected control fish during the same infection experiment.

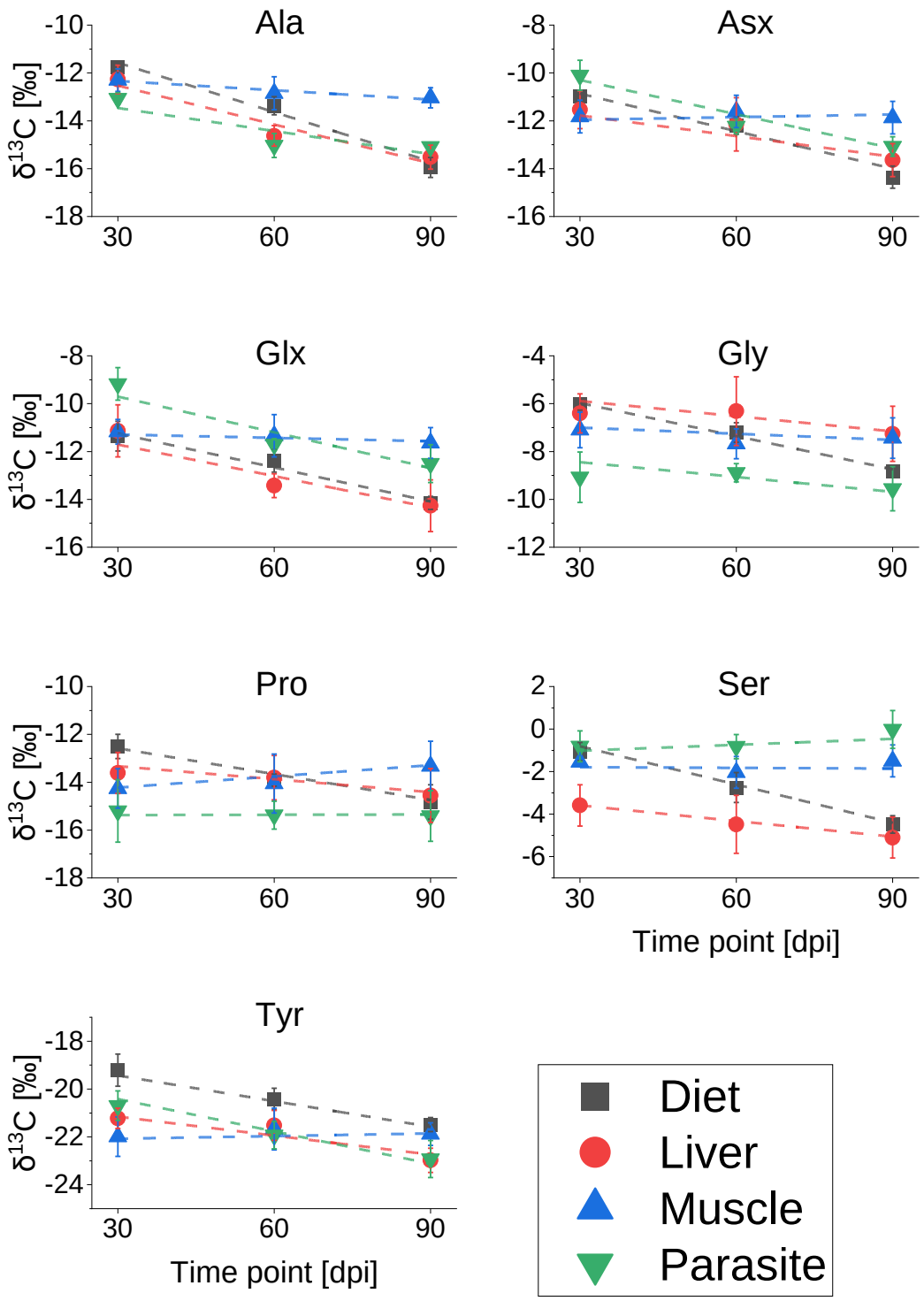

Figure 4.5: Linear regression of $\delta^{13}C$ values (‰ vs VPDB) ± standard deviations (whiskers) over 90 dpi from dietary, liver, muscle, and parasite tissue of individual NEAAs. Data for dietary samples are taken from an earlier study [178] and show a linear decrease of $\delta^{13}C$ values. Slopes of linear regression for liver and parasite tissue are negative for Ala, Asx, Glx and Tyr (one-way ANOVA).

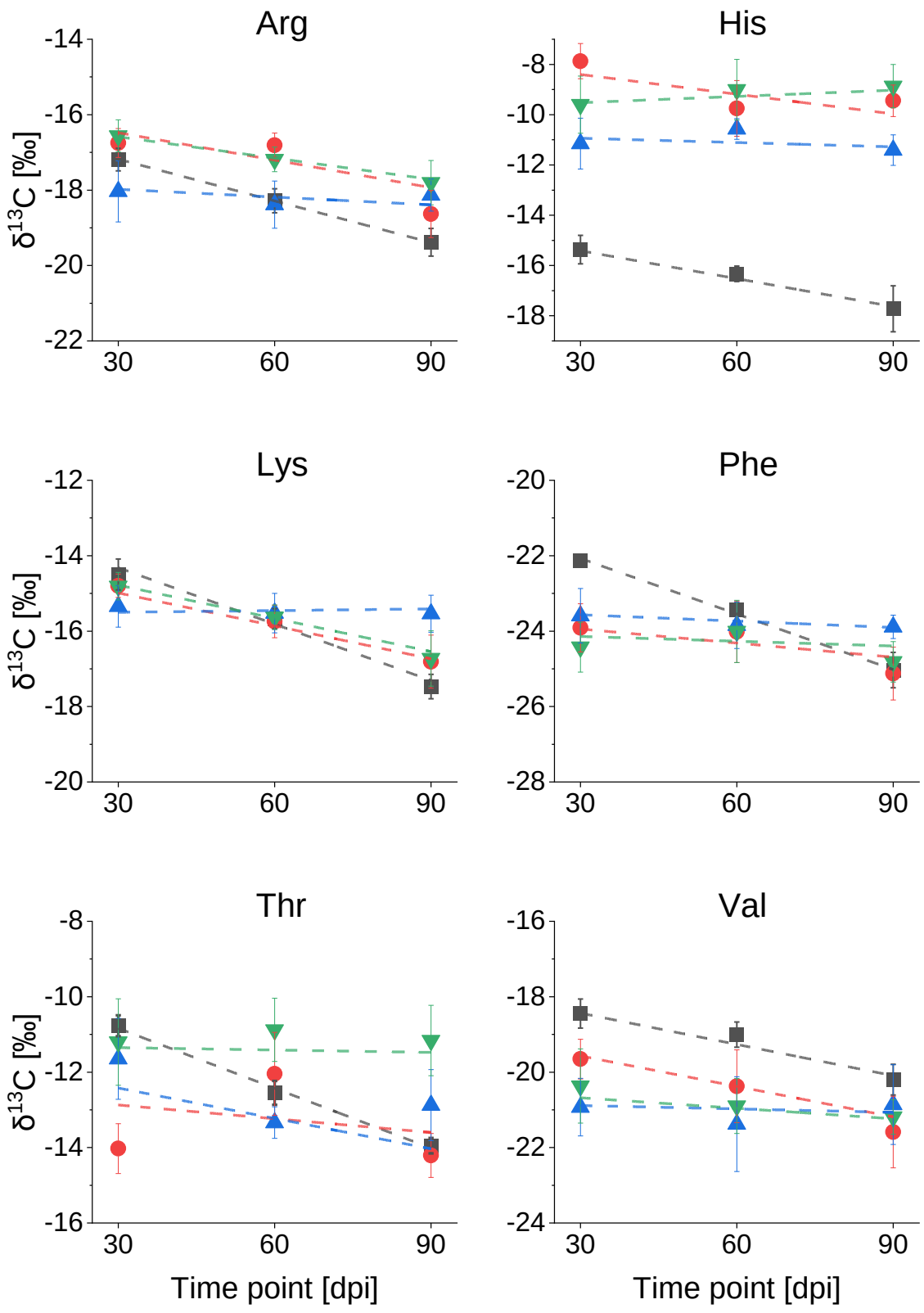

Figure 4.6: δ13C values (‰ vs VPDB) ± standard deviations (whiskers) and linear regression curves over 90 dpi from dietary, liver, muscle, and parasite tissue of individual EAAs. Symbols and colors are analogue to **Figure 4.5**.

Chapter 5: New method for $\delta^{15}N$ measurements of aqueous nitrate in a modified LC-IRMS interface: A proof-of-principle study

5.1 Abstract

Pollution of water bodies with anthropogenic nitrate has become a global environmental concern and measuring the nitrogen isotope analysis of nitrate is not only an effective way to identify pollution sources, but it also bears opportunities to study the nitrogen cycle in unpolluted environments. However, established methods for determining nitrogen isotope compositions of nitrate on natural abundance levels are labor intensive, hindering fast and reliable measurements that are needed for water monitoring programs. We modified a commercially available interface for isotope measurements to convert nitrate online into elemental nitrogen, which could be isotopically measured in an isotope ratio mass spectrometer. Nitrate was chromatographically separated from possible matrix effects on a PGC column before online conversion took place using vanadium(III)chloride and copper as reducing agents, while also implementing published improvements to the commercial interface to improve overall precision and longevity of the ion source. A precision of under 1.4 ‰ was achieved using 10 µL injections of 50 mgL^{-1} N for five different nitrate standards and reference materials, spanning a $\delta^{15}N$ range of over 180 ‰. Measuring different nitrate concentrations introduces a significant shift in $\delta^{15}N$ values, preventing accurate results for lower concentrations and representing the biggest challenge in addition to high nitrogen background levels to reach the required sensitivities for direct injections of samples from polluted water bodies. Measuring nitrate isotope compositions of unpolluted water bodies might still need pre-concentration even under optimal conditions. We discuss ways to improve the current iteration of the modified interface and give an outlook to prospects of this new method, which might even expand our ability to measure nitrogen stable isotope signatures from organic compounds.

5.2 Introduction

Nitrogen plays a major role in any cellular biomass and the nitrogen cycle is one of the most fundamental biochemical processes on earth [204]. The invention of the Haber-Bosch process, an industrial way to convert elemental nitrogen into ammonia, revolutionized our agricultural practices, but also greatly increased anthropogenic nitrogen sources that flow into ecosystems [205]. Human emissions now by far exceed the natural nitrogen fixation by microbes, which has severe impacts on our environments and human health. Nitrogen species accumulate in terrestrial and aquatic ecosystems [206] and can cause acidification while also saturating the demand of plants [207], leading to eutrophication of water bodies [208]. Nitrate is one important nitrogen species in this cycle and an essential anion for plant growth, but also a major contaminant of waterbodies because of increased fertilizer usage [209, 210]. A limit of 10 mgL^{-1} of NO_3-N for drinking water was consequently set by the World Health Organization, but adverse health outcomes such as colorectal cancer, thyroid disease and neural tube defects may even be caused by ingestion of water nitrate levels below regulatory limits [211]. Tracking the origin of nitrate in water bodies for source allocation and control is therefore important to protect our environments and human health.

Most anthropogenic nitrogen is introduced into water bodies by the use of fertilizers for crop production [212] and isotope signatures of nitrate have been frequently used in the past to track and identify their source [213-217]. The nitrogen isotope composition of chemical and natural fertilizers is different, which stems from kinetic isotope fractionation effects during fixation and conversion of nitrogen species. Manure or organic fertilizer generally have higher $\delta^{15}N$ values than synthetic fertilizers or atmospheric nitrogen, resulting in distinct $\delta^{15}N$ nitrate patterns of tile drainage water of agricultural fields according to the applied fertilization method [215]. The nitrogen isotope signature of nitrate from uncontaminated to contaminated surface or ground water consequently differ, which can be used to locate sources of increased emission [218]. However, multiple simultaneous sources of nitrate and fractionation processes may constrain the accuracy of source identification. This could be overcome by implementing water monitoring programs and Bayesian framework estimation on a large scale, but requires precise, fast and broadly applicable techniques to measure the nitrogen isotope signature of water nitrate [218]. Additionally, the nitrogen isotope signature of

nitrate provides useful information and insights into general microbial activities [219, 220] and nutrient cycling of marine ecosystems [221-226].

There are currently three methods used in the literature to determine the nitrogen isotope signature of water nitrate. The ion-exchange method was developed first and uses an anion-exchange columns to preconcentrate nitrate and nitrite, which is subsequently removed by hydrochloric acid and analyzed as silver nitrate and silver nitrite either by combustion in sealed quartz tubes or in an elemental analyzer [227]. The denitrifier method uses bacterial strains with lacking nitrous oxide reductase activity to stop the denitrification of nitrate and nitrite at N_2O, which is purified and trapped prior to IRMS analysis [228]. The cadmium-azide method uses spongy cadmium to reduce nitrate to nitrite in a first step and further reduction of nitrite to nitrous oxide before IRMS analysis [229]. All methods require extensive sample preparation and are labor intensive before the introduction into suitable IRMS systems. Furthermore, the ion-exchange and denitrifier methods cannot distinguish between nitrate and nitrite and only the cadmium-azide method is suitable for both freshwater and seawater.

Another method describes the measurement of ^{15}N abundances of aqueous nitrate and nitrite through online reduction to NO by vanadium or titanium chloride and subsequent measurement with a membrane inlet quadrupole MS (SPINS/MIMS) [230], which goes back to a continuous-flow mass spectrometry method developed in 1999 [231]. This method has been improved over the years [232, 233] and the most recent iteration uses an IRMS system instead of a quadrupole MS to measure isotope ratios directly [234]. Samples with a nitrogen concentration of 35 $\mu molL^{-1}$ N for nitrate can be measured and $\delta^{15}N$ values from standards are reported with a precision smaller than 0.9 mUr. However, this approach uses concentrated hydrochloric acid and high amounts of VCl_3 and peristaltic pumps, hence chromatographic separation beforehand cannot be implemented and problems with blank contributions and matrix effects in addition to high CO_2 and water background in the ion source might occur, leading to isobaric interferences. Furthermore, sample volumes of more than 1 mL are necessary for each measurement, which might be a consequence of the afore mentioned interferences to ensure the necessary precision for measurements on natural abundance levels.

Simultaneously to the method described by Eschenbach and Dyckmans et al. [234], we developed a similar approach by modifying the commercially available LC IsoLink™

interface (Thermo Fisher Scientific Inc., Bremen, Germany). The goal was to measure nitrogen signatures from nitrate through online conversion into gaseous nitrogen species and subsequent reduction to elemental nitrogen while still allowing for low volume sample injections. We further aimed for chromatographic separation of nitrate from the injection peak, but possibly also other nitrogen oxide species like nitrite or matrix interferences encountered in real samples. This will increase accuracy and precision through matrix removal, circumvent the necessity for blank correction, greatly reduce the required sample amounts and has the potential to enable nitrogen isotope analysis of organic compounds via LC-IRMS in the future. Furthermore, we implement already reported improvements to the interface [78], which not only enables the measurement of nitrogen isotope signature of elemental nitrogen instead of nitrous or nitric oxide, but also helps with increased filament lifetime and reduced water, oxygen and carbon dioxide backgrounds in the ion source and is described here for the first time for nitrogen stable isotope measurements. We report first results of standard sample measurements with the modified interface and discuss current problems, improvements, and prospects of this new technique.

5.3 Materials and methods

5.3.1 Chemicals and solutions

Vanadium(III)-chloride (97 %, Merck, Darmstadt, Germany) was used to prepare solutions of 0.015 M VCl_3 in 0.3 M HCl (36.5 – 38 %, Alfa Aesar, Kandel, Germany). To preserve the HPLC pumps, which consist of stainless steel and are susceptible to high chloride concentrations, we did not use excessive amounts of reducing agents. The reduction of NO_3^- to NO with $V(III)Cl_3$ follows the chemical reaction [230]:

$$NO_3^- + 3V^{3+} + 4H^+ \rightarrow NO + 3V^{4+} + 2H_2 \qquad \text{(Eq. 5.1)}$$

Three parts of vanadium(III) are required to reduce one part of nitrate to nitrogen oxide. A solution of 0.015 M VCl_3 is therefore capable to reduce 0.005 M NO_3^-, which corresponds to a sample concentration of 140 mgL^{-1} $N\text{-}NO_3$ that can be injected into the system and completely reduced if we consider that the mobile phase and reducing agents are mixed 1:1 before they enter the reduction oven. The reduction of nitrate with vanadium(III) requires strong acidic conditions at or below pH 1, which was provided by a 0.3 M HCl

solution in which the vanadium(III)-chloride was solved [235]. The solution was prepared with degassed Milli-Q water to avoid oxidation with dissolved oxygen and stored in a refrigerator for up to one week. The eluent was prepared by diluting sulfuric acid (95-97 %, Merck, Darmstadt, Germany) to 0.005 M H_2SO_4 or other required concentrations. All solutions were further purged under vacuum by a membrane pump (Vacuubrand GmbH & Co., Wertheim, Germany) and in an ultrasonic bath (Sonorex RK 100 Bandelin Electronic, Berlin, Germany) for at least 15 min and continuously flushed with a small flow of Helium 5.0 (Air Liquide, Oberhausen, Germany) while being used. The isotopic reference materials USGS 32, 34 and 35 (IVA Analysentechnik GmbH & Co. KG, Meerbusch, Germany) and nitrate in-house standards KNO_3 and $NaNO_3$ (>99 %, Merck, Darmstadt, Germany) were measured on an Isoprime100 Elemental Analyzer (Elementar Analysensysteme GmbH, Langenselbold, Germany) for referencing. Standard solutions usually contained 50 mgL^{-1} Nitrate-N and one standard dilution series was made with concentrations of 10, 25, 50 ,75, 100 mgL^{-1} Nitrate-N to test the concentration dependence of the system.

5.3.2 Experimental setup

A schematic of the modified system is depicted in **Figure 5.1** and based on the commercially available LC-Isolink interface (Thermo Fisher Scientific, Bremen, Germany) coupled to a DELTA V Advantage IRMS (Thermo Fisher Scientific, Bremen, Germany) for continuous flow applications. Eluents and reducing agents were pumped with two separate HPLC pumps (LPG-3400 SD and HPG-3200 SD, Thermo Fisher Scientific, Bremen, Germany). Flow rates for the eluent and reducing agents were both set to 200 $\mu Lmin^{-1}$. Nitrate injections were performed by an HTC PAL autosampler (CTC Analytics AG, Zwingen, Switzerland) with different sizes of PEEK sample loops (5, 10 and 20 µL). Separation of nitrate from the injection peak and other possible matrix effects was achieved with a Hypercarb™ PGC column (2.1 x 100 mm, 3 µm, Thermo Fisher Scientific GmbH, Bremen, Germany) and an eluent of 0.005 M H_2SO_4. In addition, column temperature was increased to 80°C and regulated by a HT-HPLC 200 column oven (Scientific Instruments Manufacturer GmbH, Oberhausen, Germany) to further control retention times and peak shape. The reducing agent was added to the eluent via the low volume mixing T-Piece included in the commercial LC-Isolink interface and pumped into a heated fused silica capillary (ID = 0.32 mm; length = 8 m) for reduction. The dimensions

of the fused silica capillary result in a reactor volume of ~0.64 mL and a residence time of the analytes longer than 1.5 min with a combined flow rate of 0.4 $mLmin^{-1}$. This is comparable to the minimum residence time of 1 min in the regular oxidation reactor of the interface. Heating was facilitated by a small temperature-controlled GC oven and controlled by a Eurotherm 2216e microprocessor (Schneider Electric Systems, Limburg, Germany). The mobile phase was cooled after reduction in a water bath before it entered the gas separation unit of the LC-IRMS interface. A small in-line filter made of PEEK was installed before the gas separation unit to shield the three membranes from possible non soluble particles. The analytes are extracted and transported by a helium stream (Helium 5.0, Air Liquide, Oberhausen, Germany) of approx. 1 – 2 $mLmin^{-1}$ through the two Nafion membranes of the interface and into two subsequent heated copper reactors. The reactors each consisted of 4 individual copper wires (Length = 28 cm; OD = 0.125 mm), which were manually twisted and inserted into a heated ceramic tube (Length = 320 mm; ID = 0.5 mm) inside a custom-made GC oven, controlled by two Jumo Itron16 (JUMO GmbH &Co. KG, Fulda, Germany) microprocessors and held at 650°C. The copper reactor and subsequent water trap using a slurry of acetone/dry for the LC-IRMS system are already described in the literature [78] and serve several purposes. The copper reactor acts as an oxygen scrubber and reduces the oxygen background in the gas phase. Under normal conditions, when measuring carbon isotope signatures, peroxides are used in excess to oxidize any organic carbon to CO_2 in a wet chemical reaction, which leads to a very high oxygen background in the aqueous phase. Oxygen is extracted into the gas phase along with carbon dioxide through the gas separation unit and enters the ion source of the IRMS, causing constant oxidation of the tungsten filament over time. Removing excess oxygen in the gas phase increases the lifetime and precision of the filament. More importantly in this case, however, is the ability of heated copper to reduce gaseous nitrogen oxides species to elemental nitrogen [236] according to the following equation:

$$y\ Cu + N_xO_y \rightarrow y\ CuO + \frac{x}{2}N_2 \qquad \text{(Eq. 5.2)}$$

Regeneration of the copper reactors was achieved by a stream of 3 % H_2 in He (Crystal Mixture, Air Liquide Düsseldorf, Germany) at 3 – 4 $mLmin^{-1}$. The water trap was initially added to further remove the water background, which is still increased even after the two Nafion membranes in the LC-Isolink interface. Excess water in the ion source can compromise isotope measurements due to protonation of analyte molecules, artificially increasing their mass to charge ratio by one. Instead of operating the water trap with

acetone and dry ice, it can also be operated with liquid nitrogen to not only remove water but also carbon dioxide from the gas phase, which can interfere in the ion source through isobaric interferences of CO for the measurement of elemental nitrogen. The same principle is applied in GC-IRMS systems for the measurement of nitrogen stable isotope signatures [237]. The analyte stream now only contains elemental nitrogen and was introduced into the IRMS (Delta V Advantage, Thermo) through the open split system for constant pressure conditions in the ion source.

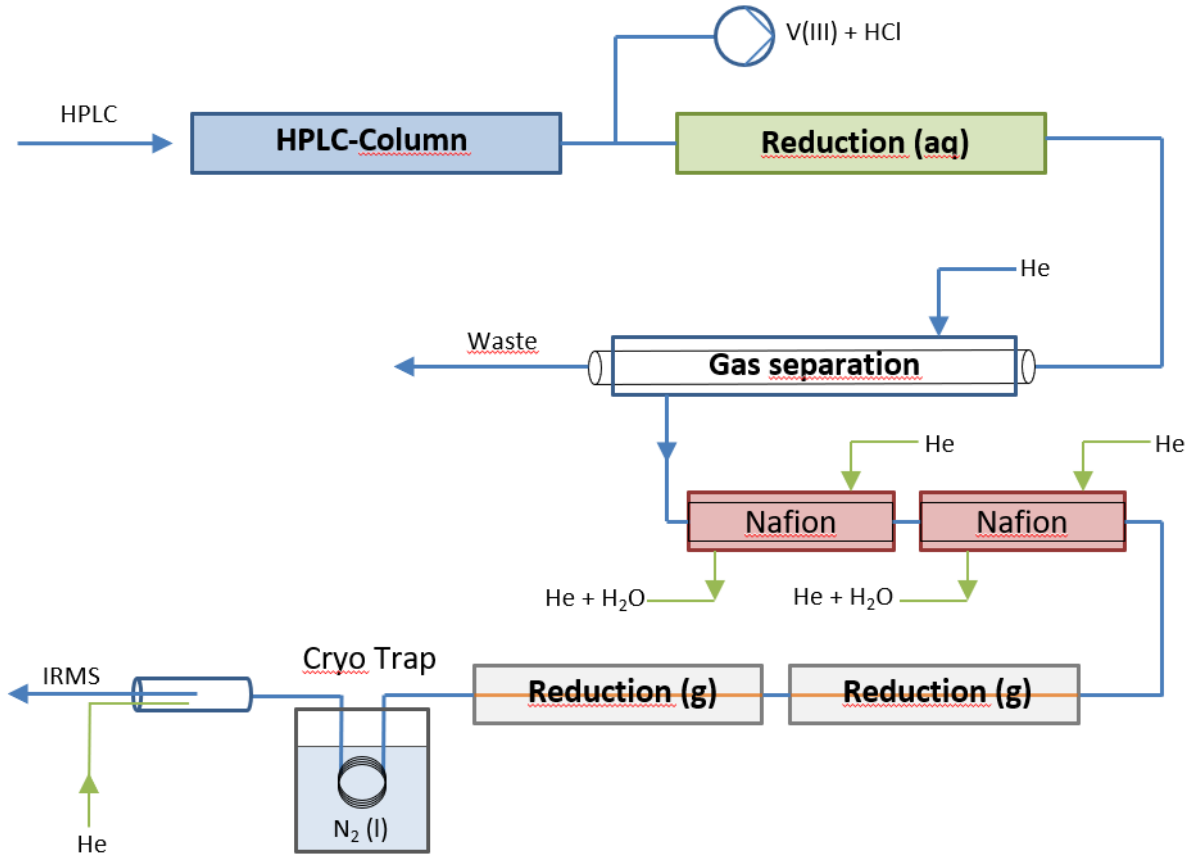

Figure 5.1: Schematic overview of the modified LC-Isolink interface with two reduction reactors as the main part. The first reactor consists of a heated fused silica capillary and reduces nitrate to nitrogen oxide in the aqueous phase with VCl_3 as reducing agent under acidic conditions. The second reduction reactor consists of two heated consecutive ceramic tubings which each hold four twisted copper wires to further reduce nitrogen oxide to elemental nitrogen at 650 °C. A PGC column facilitates separation of nitrate from the injection peak.

5.4 Results and discussion

5.4.1 Stability and linearity under measurement conditions

To evaluate the ability of the modified LC-IRMS system to accurately measure nitrogen isotope signatures of elemental nitrogen, we injected ten consecutive reference gas peaks with constant (stability) and increasing (linearity) signal intensities. The intensity of reference gas peaks was controlled by changing the gas pressure of the reference gas with the pressure regulator of the interface. We simultaneously opened the sample open split while pumping a 0.05 M H_2SO_4 eluent and 0.015 M VCl_3 in 0.3 M HCl reducing agent at 200 $mLmin^{-1}$ each. Average (Avg) and standard deviations (SD) of $\delta^{15}N$ values from ten reference gas peaks are given in **Table 5.1** and compared to linearity measurements without background signals by turning off the sample open split. The SD of linearity measurements of nitrogen isotope signatures without any background signals under ideal conditions was 0.06 and increased to 0.41 when conducting the same measurements with an active sample open split. The SD of stability measurements with an active sample open split was 0.37. The main cause for the increasing SD of measurements with an active open split are outliers (peak no. 6 for linearity and peak no. 4 for stability measurements, marked red in **Table 5.1**) throughout the complete series of ten reference gas injections. The cause for these outliers are small shifts in the m/z 29/28 ratios (**Figure 5.6**, Appendix) occasionally appearing throughout chromatograms. The shifts tend to be one-minute-long and, due to the nature of the interface to produce wide peaks, they might originate from the liquid phase of the system, possibly due to piston movement of the HPLC pumps. We took great care to manually check and avoid measurements where one of these shifts occurred under peaks of interest. Despite these interferences, the system performs sufficiently robust and can measure nitrogen isotope signatures of elemental nitrogen with a precision better than 0.5 ‰ over a peak area range of 4.6 to 21.3 Vs and possibly more precise if background shifts are avoided.

Table 5.1: Average and SD of linearity and stability tests using ten injections of reference gas peaks w/ and w/o background signals. Tests performed with background signals show occasional outliers (marked red) and originate from small shifts in the m/z 29/28 ratio throughout chromatograms.

Peak	Linearity w/ background		Linearity w/o background		Stability w/ background	
	Area All (Vs)	$\delta^{15}N$ (‰)	Area All (Vs)	$\delta^{15}N$ (‰)	Area All (Vs)	$\delta^{15}N$ (‰)
1	4.6	-0.05	5.6	-0.01	12.4	-0.02
2	6.1	0.12	7.5	-0.06	12.4	-0.11
3	7.6	-0.42	9.0	-0.17	12.5	-0.20
4	9.3	-0.33	11.0	-0.18	12.5	0.90
5	11.1	0.16	12.8	-0.10	12.5	0.00
6	13.1	1.07	14.7	-0.09	13.5	-0.03
7	15.1	0.06	16.9	-0.01	12.4	-0.22
8	17.0	-0.13	18.8	-0.03	12.5	-0.26
9	19.2	-0.05	21.3	-0.07	12.5	0.57
10*	21.3	0.00	23.4	0.00	12.5	0.00
Avg		**0.04**		**-0.07**		**0.06**
SD		**0.41**		**0.06**		**0.37**

5.4.2 Separation of nitrate and nitrite from injection peak

Blank injections into the modified interface produce significant nitrogen peaks (**Figure 5.2A**), which also occurred with no reducing agents and reactors at room temperature. The measured $\delta^{15}N$ signatures of these peaks were between +2 and +8 ‰ against the nitrogen reference gas, depending on the exact system conditions. We therefore assume that blank peaks are either produced by dissolved elemental nitrogen in the sample or by switching the valve position of the 6-port valve in the autosampler. Switching the valves might introduce small amounts of elemental nitrogen from the surrounding air into the eluent flow of the system. Separation of nitrate and/or nitrite from the injection peak was therefore crucial to avoid interferences and achieved by a PGC column (Hypercarb 100 * 2.1 mm, 5 µm, ThermoScientific). PGC columns can be used to interact with small negatively charged ions due to π-interactions [238]. We used elevated column temperatures at 80°C and diluted sulfuric acid as an electronic competitor to elute nitrate from the column. Without an electronic competitor and only water as the eluent, nitrate would be totally retained on the column, as it was similarly also described for phosphonic acids [239]. Sodium sulfate was used by Takeuchi et al. [238] to separate inorganic anions including nitrate and nitrite on a PGC column, but we decided to use diluted sulfuric acid instead to keep the pH as low as possible for subsequent reduction. However, due to the

broad peak widths produced in the LC-IRMS interface, efficient separation of nitrite and nitrate simultaneously was not possible. Since the focus of this work was the measurement of nitrogen isotope signatures from nitrate, separation of nitrate from both blank and nitrite peaks was considered sufficient. The concentration of sulfate in the eluent, flow rates and column temperatures can be used to influence the retention time of nitrate, which is not only useful to control the overall run time but should be further beneficial when measuring real samples to avoid possible matrix interferences or baseline fluctuations. Changing and testing different column parameters or materials along with different eluents might result in improved performance of the system.

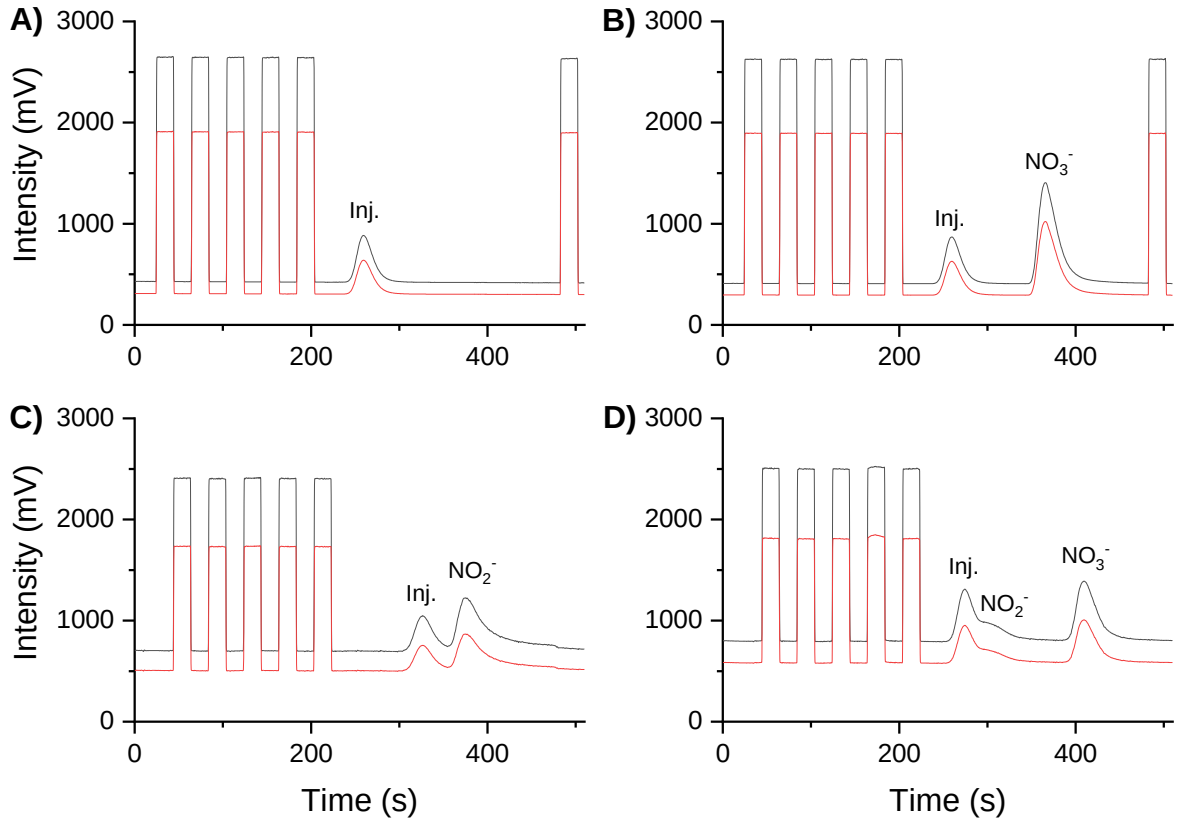

Figure 5.2: Chromatograms of blank (A), nitrate (B), nitrite (C) and a mix of both nitrate/nitrate (D) injections into the modified LC-IRMS interface for the measurement of nitrogen isotope signatures. Blank injections produce a measurable nitrogen peak (A). Separation of nitrate (50 mgL^{-1} N, 10 µL injection volume) from the injection peak (B) was necessary and achieved with a porous graphitic carbon HPLC column (Hypercarb 100 * 2.1 mm, 3 µm, Thermo Scientific) and an eluent of 0.005 M H_2SO_4. The HPLC flow was set to 200 $\mu Lmin^{-1}$ for both the eluent and reducing agent (0.03 M VCl_3 in 0.3 M HCl) and column temperature was held at 55 °C. Injecting a mixture of nitrate and nitrite (50 mgL^{-1} N each, 5 µL injection volume) under these flow conditions (D) shows that nitrite is not fully separated from the injection peak. Reducing the eluent flow from 200 to 150 $\mu Lmin^{-1}$ and increasing the column temperature to 80 °C (C) almost separates nitrite (100 mgL^{-1} N, 5 µL injection volume) from the injection peak. Note that the injection volume was reduced from initially 10 µL (A and B) to 5 µL (C and D) to reduce the load of nitrogen oxides on the copper reactor.

5.4.3 Repeated nitrate measurements and reactor performance

Although the modified interface does not employ any form of peroxides and therefore has a significantly lower oxygen load, the amount of oxygen introduced into the ion source is still higher than in a GC-IRMS system and depletes the copper reactor over time. In addition, the combustion reaction in GC-IRMS partly yields elemental nitrogen and the copper reactor afterwards only needs to reduce residual nitrogen oxide species [240]. The reduction of nitrate with vanadium(III), however, only yields nitrogen oxide species and thus the copper reactor has to reduce higher amounts of nitrogen oxides. To evaluate the ability of the copper reactor to reduce the relatively high loads of nitrogen oxides coming from the modified LC-IRMS interface in addition to the higher oxygen loads coming from the eluent, we consecutively injected 5 µL of a 50 mgL^{-1} N solution of the USGS 34 international reference material on three following days. The copper reactor was reduced overnight in between measurement days with a 2 $mLmin^{-1}$ flow of 3 vol % H_2 in Helium gas. The measured $\delta^{15}N$ values are constant for four to six injections, after which they start to fall off and drop continuously until the 20^{th} to 25^{th} injection (**Figure 5.3**). Regenerating the reactor overnight does increase the measured $\delta^{15}N$ values on the next day, but not to the exact same values previously observed. This shows that regenerating the reactor is feasible, but there might still be daily differences in reactor or system performance. Frequent referencing through international or in-house standards, as typically required and practiced in CSIA, should minimize the influence of changing daily performance. Interestingly, the initial four to five injections on each day show more constant measurements of $\delta^{15}N$ values, after which the measured values start to either slowly or suddenly drop. This indicates that reactor performance is stable for the first few injections, but quickly declines afterwards. Measuring nitrogen isotope ratios from nitrate with high precision throughout a day or for prolonged sample runs might therefore require a combination of two copper reactors in parallel, where one reactor is used for one or several injections of nitrate samples while the other is regenerated with a separate line of hydrogen gas. Switching between the two reactors in between sample runs might facilitate constant and accurate measurement over long measurement series. This approach was also realized in the afore mentioned study to reduce high oxygen loads from persulfate [78], but was out of the scope of this study. One concern employing two reactors in parallel could be that the two separate copper reactors need to perform identical under measurement conditions. Removing excess oxygen for the measurement

of carbon isotope signatures, like it was realized in 2007 [78], does not require the copper reactors to participate in any reaction where the analyte molecules are involved and therefore are only used for removing interfering matrix effects. Slight differences in reactor performance directly after regeneration were therefore not disadvantageous for the measurement of carbon isotope signature, but, as can be seen in our experiments on three consecutive days, it can be detrimental to the analysis if the molecule of interest is part of the reactions occurring in the reactors. Changing the dimensions of the reactors to increase the amount of copper inside the ceramic tubing might be an additional way to further optimize reactor performance, although we already noticed a temperature gradient inside of the reactor case due to the length of the heating block. Evaluating the performance of the reactor on its own by using dissolved nitrogen oxides like N_2O could be beneficial in the future to find optimal reaction parameters and increase stability and precision of isotope measurements.

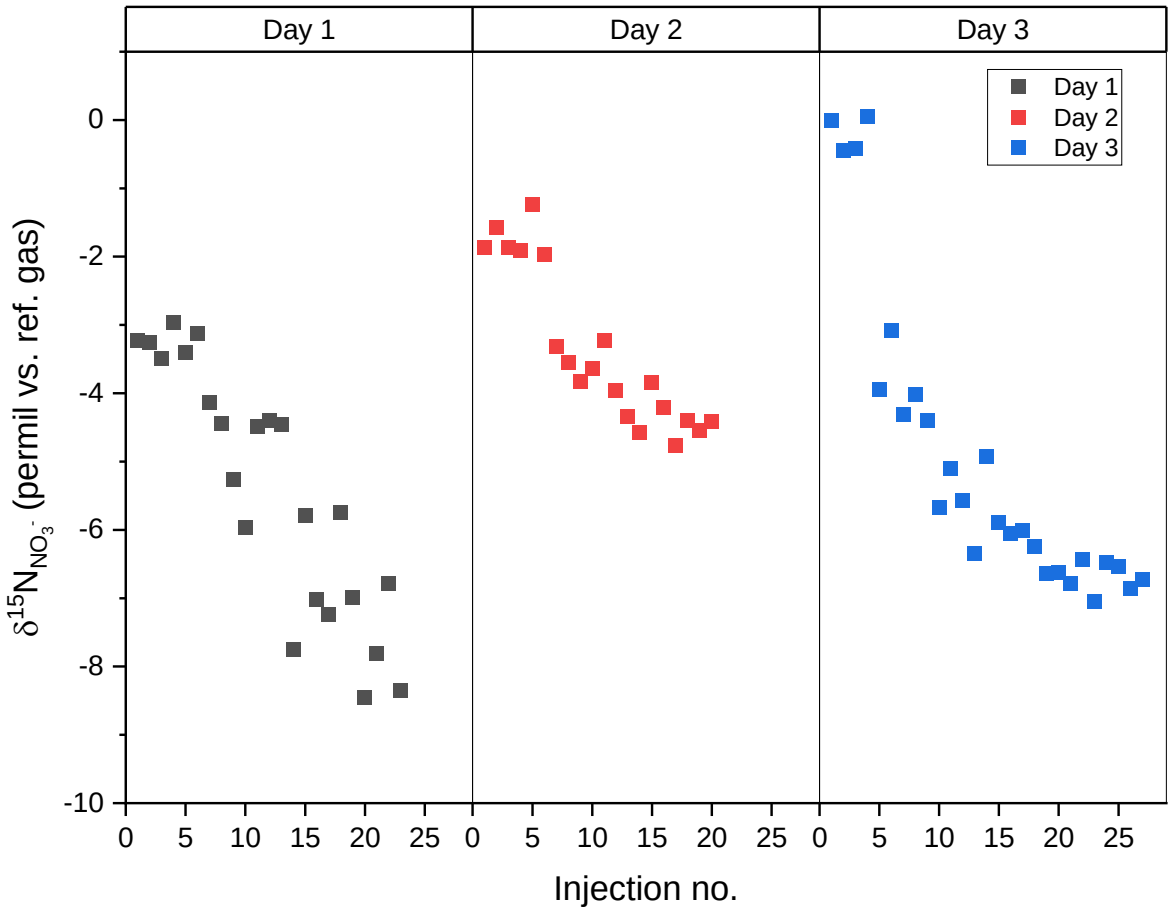

Figure 5.3: Consecutive injections of 5 µL USGS34 (50 mgL^{-1} $N\text{-}NO_3^-$) into the modified interface on three subsequent days. The copper oven was regenerated overnight with a 2 – 4 $mLmin^{-1}$ flow of 3 vol% H_2 in He in between days. The measured $\delta^{15}N$ values are constant for the first four to six injections on each day, after which they gradually decrease with each further injection. Regeneration of the copper wires overnight increases the measured $\delta^{15}N$ values on the next day.

5.4.4 Measuring different nitrogen reference materials with different isotopic signatures

A key point of analytical instruments in stable isotope analysis is the ability to differentiate between samples and materials with different isotope signatures. That does include differences between artificially enriched isotope ratios, which can be as high as hundred permil, but also differences on natural abundance levels of only a few permil or less. We used two international nitrate reference materials with accepted nitrogen isotope signatures on natural abundance levels (USGS 34 and USGS 35) and one material which is enriched in its nitrogen isotope ratio (USGS 32). In addition, we calibrated two in-house nitrate standards (KNO_3 and $NaNO_3$) on an EA-IRMS system with the three USGS reference material. The referenced values of all five standard and reference materials are summarized in **Table 5.2**.

Table 5.2: Referenced and measured $\delta^{15}N$ values of in-house standards and international reference materials. Samples were injected in triplicate with 10 µL injection volume and a concentration of 50 mgL^{-1} N. Although the first injection of USGS 34 was statistically not an outlier according to Grubbs tests with a 95% confidence level due to the low sample size, we removed this value from further analysis because it had an abnormal variation in comparison to the variance of the other standard and reference materials.

Material	Referenced $\delta^{15}N$ (‰)	Measured $\delta^{15}N$ (‰)
KNO_3	0.0	-8.6
		-8.6
		-8.5
$NaNO_3$	8.4	-0.6
		-0.1
		-0.1
USGS 35	2.7	-4.4
		-4.8
		-4.7
USGS 32	180.0	163.6
		166.3
		165.5
USGS 34	-1.8	-7.6
		-10.2
		-10.5

We injected 10 µL of a 50 mgL^{-1} N solution of each material in triplicate and plotted the measured $\delta^{15}N$ values with all standard and reference materials (**Figure 5.4A**) and with only materials on natural abundance levels (**Figure 5.4B**). The y-intercept of a linear

regression curve between referenced and measured $\delta^{15}N$ values shows that measured $\delta^{15}N$ values are in general -8.1 and -8.2 ‰ lower than the referenced values, but a slope of 0.96 and 0.99 indicates that the differences between measured values of different materials are in good agreement to the differences of referenced values.

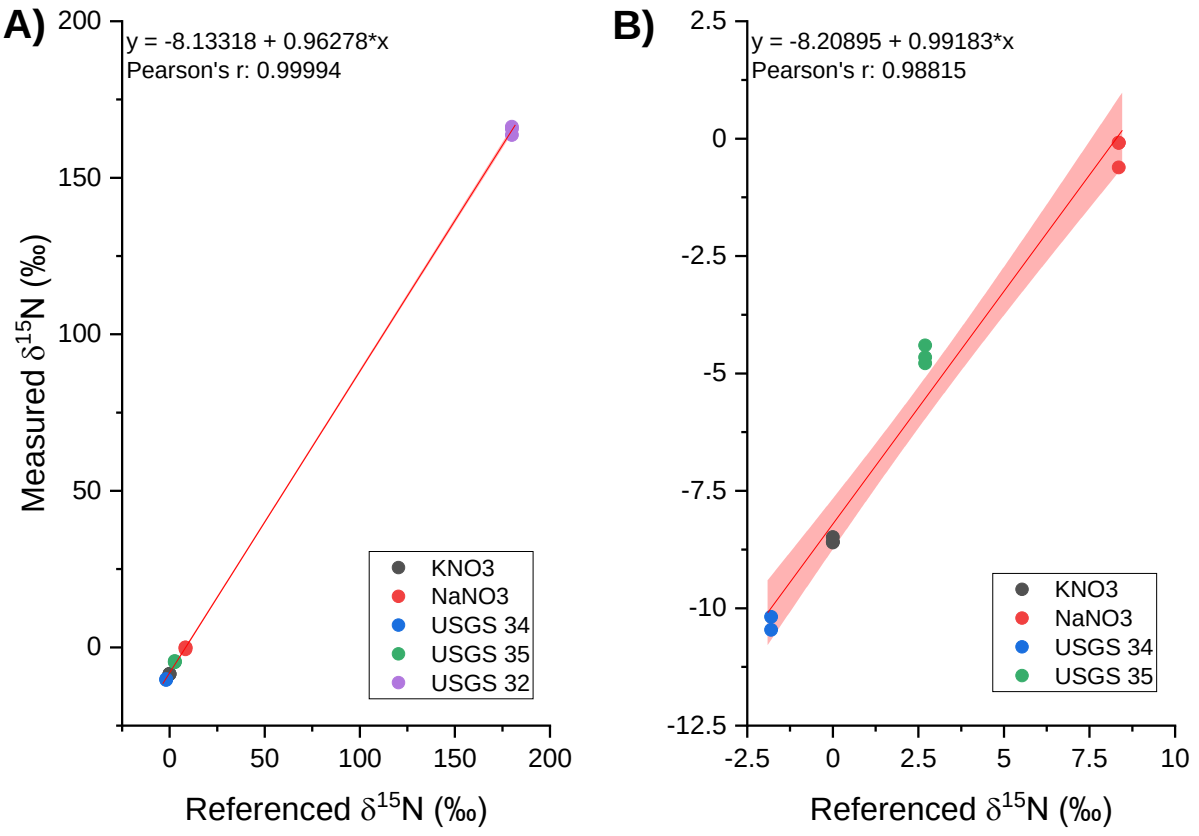

Figure 5.4: Differences between measured and referenced $\delta^{15}N$ values of reference materials and in-house standards are in good agreement. Since USGS 32 is an enriched reference material **(A)**, it was removed for the linear regression **(B)** to decrease the range of $\delta^{15}N$ values to more natural abundance levels. Red line indicates linear regression curve and red areas give the 95 % confidence interval. Samples were injected in triplicates and one injection of USGS 34 was removed from the analysis because it showed an abnormally high variation compared to the variance of the other materials.

The Pearson correlation between samples on natural abundance levels shows a strong linear relationship but is not very informative in case of all samples including the enriched material, since the regression is forced between only two clusters of isotope values. We further removed one measurement from USGS 34 (**Table 5.2**). Although it was not detected as an outlier with Grubbs test and a 95 % confidence level because of the small sample size of only triplicate injection, it showed an abnormal difference compared to the variance of other measurements. As mentioned earlier, we occasionally observed small shifts in the m/z 29/28 ratio during measurements, which resulted in higher measured $\delta^{15}N$ values if the shifts overlapped with either a reference gas peak or a chromatographic

peak and could have caused the observed difference. The reported values were produced throughout continuous measurements on two individual days and the copper reactors were regenerated overnight as explained earlier. The results are therefore also subject to isotope shifts over extended measurement periods and to different copper reactor performance on individual sampling days. Addressing these issues might therefore further improve the precision and linearity of the regression. However, the reported values already show that the measurement of nitrogen isotope signatures from nitrate with the current setup are feasible on both natural abundance and enriched levels.

5.4.5 Measuring different nitrate concentrations

We prepared and measured a dilution series of $NaNO_3$ in-house standards to evaluate the ability of the modified interface to measure nitrogen isotope signatures of nitrate samples with different concentrations (**Table 5.3**). 10 µL injections of different $NaNO_3$ solutions were done in triplicate and the measured $\delta^{15}N$ values and peak areas were plotted against the nitrogen concentration (**Figure 5.5**). $\delta^{15}N$ values increase non-linear from -7.5 ± 1.4 ‰ to +1.8 ± 0.1 ‰ over a range of 10 to 100 mgL^{-1} $N\text{-}NaNO_3$ while peak areas simultaneously increase non-linear from 1.6 ± 0.0 Vs to 55.1 ± 0.3 Vs and are best described by a second order polynomial equation with a Pearson r of 0.998. The measured $\delta^{15}N$ values of 50 mgL^{-1} $N\text{-}NaNO_3$ was -0.4 ± 0.2 ‰ and therefore identical to the isotope signature listed in **Table 5.3** where the same concentration and injected sample volume was used. We do not believe the observed shift of $\delta^{15}N$ values and non-linear increase of peak area are caused by an incomplete reduction of nitrate or nitrogen oxides. An incomplete reaction could be caused by either low amounts of reduction agents (both VCl_3 and copper) or too little residence times in the reactors, but it would lead to a flattening of the curve with increasing nitrate concentrations. In contrast, we observed a non-linear increase in peak areas with increasing nitrate concentrations leading to higher peak areas in comparison to a linear relationship. We therefore assume that some of the nitrate or nitrogen is lost or masked inside the system and not detected. Measuring nitrogen isotope signatures in this setup produced a constant and high nitrogen background signal throughout the chromatogram.

Table 5.3: Measured $\delta^{15}N$ values of $NaNO_3$ in different concentrations shows a shift in the measured nitrogen isotope signature and a non-linear increase of the peak area over a range of 10 to 100 mgL^{-1} N.

Conc. (mgL^{-1} N)	Area (Vs)	Measured $\delta^{15}N$ (‰)
100	54.8	1.7
	55.2	1.8
	55.4	2.0
75	39.9	1.2
	39.4	1.2
	39.3	1.3
50	21.1	-0.6
	22.3	-0.2
	22.5	-0.4
40	15.6	-1.1
	15.8	-1.0
	15.6	-0.9
30	10.4	-1.7
	10.6	-2.1
	10.6	-1.7
25	8.5	-2.8
	8.6	-2.2
	8.6	-2.5
20	5.7	-3.2
	5.7	-3.1
	5.8	-3.8
15	3.7	-4.0
	3.8	-4.7
	3.7	-4.1
10	1.6	-7.3
	1.6	-6.2
	1.6	-9.1

The high nitrogen background is originating from the eluent, as switching off the HPLC pumps drastically decreases the nitrogen background when no eluent flow goes through the gas separation unit. The measured m/z 28 and 29 signal in the IRMS then only represents the nitrogen background from the helium flow in the gas phase of the system and typically is below 40 mV, depending on the carrier and purge gas flow as well as capillary dimensions and air tightness of the connectors. Turning on the HPLC pumps increases the nitrogen background by at least an order of magnitude, going up to 1000 mV depending on the flow rate. Purging the eluent prior in an ultra-sonic bath for up to 1 hour under vacuum and using a degasser unit in front of the HPLC pumps to remove solved nitrogen does not resolve this issue. Early experiments with an older HPLC pump,

which did not have an automated piston flush to clean the backside of the pump head showed even higher nitrogen backgrounds. Degassing the eluent downstream in the high-pressure area of the flow is not feasible, since degasser units or any device with a membrane for degassing would not withstand the high pressures especially if a HPLC column is used for chromatographic separation of analytes. Another possible reason for the non-linear increase of nitrogen peak areas could be the length of the system and corresponding prolonged peak width and accompanied tailing. The original LC-IRMS interface already suffers from high peak widths and bad shape due to the oxidation reactor and subsequent gas separation unit. Any further modification in the form of additional reduction reactors in the gas phase, cryogenic traps, or higher internal diameters of the used FS capillaries for the VCl_3 reactor in comparison to the very narrow diameters of the original stainless-steel capillary, which is not compatible with the used reduction solvents of VCl_3 in hydrochloric acid, further complicates this issue and might compromise peak detection and integration in the ISODAT software. The lowest injected nitrate concentration of 10 mgL^{-1} N shows a noticeable increase in measurement uncertainty and the largest shift of $\delta^{15}N$ values. It might not be useful at this point to determine levels of detection (LOD) for the current state of the modified interface before further improvements and optimizations are done, but it points to an emerging challenge for the direct measurement of nitrogen isotopes signature of aqueous nitrate. The sensitivity of the LC-IRMS system is one of the major drawbacks even for carbon isotope measurements. The lowest reported LODs of amino acids, e.g., were 7.3 and 8.0 ng carbon on column [45, 46] with a precision of below 0.3 ‰, which translates to a sample concentration of just below 1 mgL^{-1} C when 10 µL of sample is injected. Increasing the injection volume is not always feasible to decrease the LOD, since chromatographic separation has to be maintained and is a critical factor when designing LC-IRMS methods [241]. Measuring nitrogen isotope signatures of elemental nitrogen further increases the LOD, as it takes two nitrogen atoms to form one molecule of elemental nitrogen and the ionization efficiency of elemental nitrogen in the electron impact ion source of the IRMS is only ~70 % of the ionization efficiency for carbon dioxide [240]. Under optimal conditions, we could therefore expect a LOD of ~3 mgL^{-1} N, which would be equal to 13 mgL^{-1} NO_3^- when 10 µL of sample volume are injected. This might be sufficient for water samples from areas affected by substantial agricultural activities, which results in nitrate concentrations between 10 and 50 mgL^{-1} N [242], but the nitrate concentration in

groundwaters or areas with limited agricultural activities might be below the currently expected LOD of the modified interface. As mentioned earlier, increasing the injection volume is a potential way of achieving the necessary analyte amount on the column if chromatographic separation is assured and the column is not overloaded, but measuring nitrate isotope signatures by directly injecting water samples might still be out of the scope of the current setup if samples with natural nitrate concentrations are of interest. Sample enrichment prior to injection might be necessary if the sensitivity of the system cannot be further increased. This could be achieved by evaporation under vacuum as long as isotope fractionation is not observed or by the use of anion exchange columns on site to preconcentrate nitrate, as described by the ion-exchange method[227].

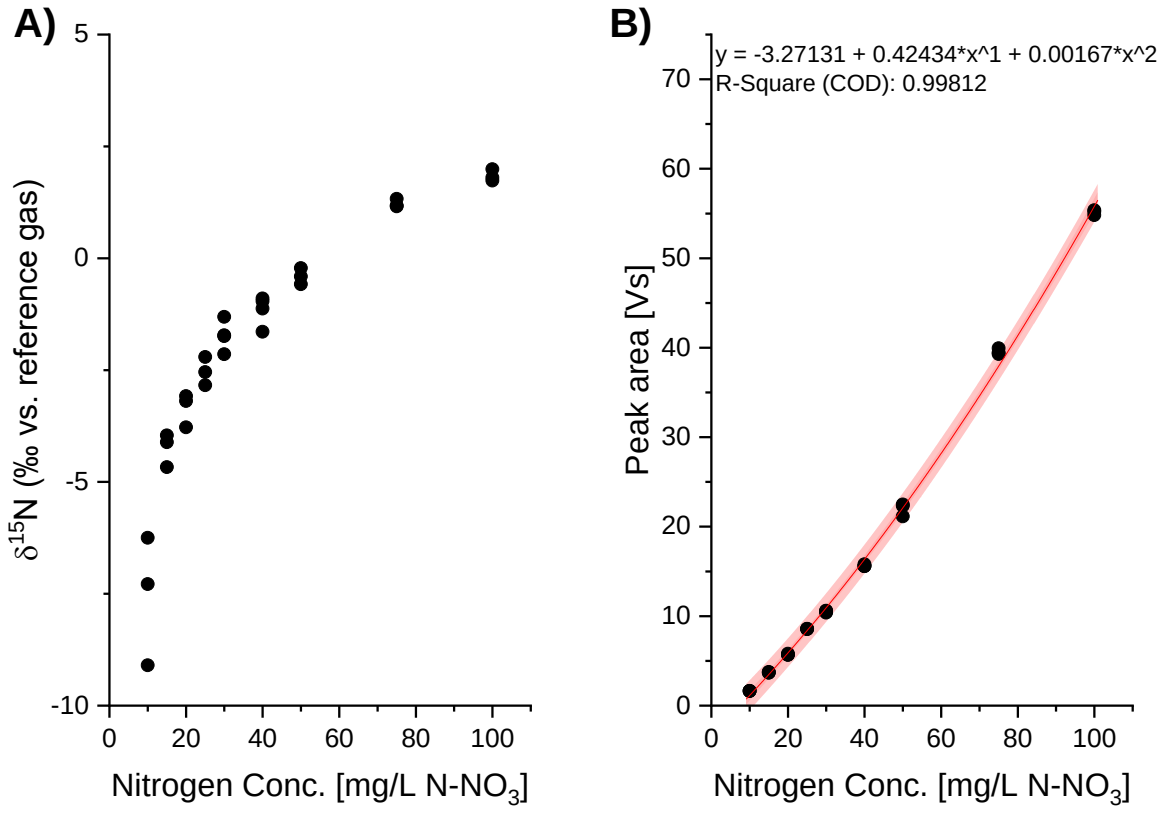

Figure 5.5: Injection of nitrate in different concentrations leads to a shift of measured $\delta^{15}N$ values (A) and a non-linear increase in peak areas (B). 10 µL $NaNO_3$ solutions from 10 to 100 mgL^{-1} N-NO_3 were injected in triplicate and the $\delta^{15}N$ values (‰) and peak area (Vs) measured. Peak integration was done by ISODAT software with the default settings of 0.2 and 0.4 mVs^{-1} start and end slope detection and an individual background detection algorithm with a 5 second history. The increase in peak area over the concentration range is best described by a second polynomial equation with R-Square of 0.998.

5.5 Conclusion

This study presents a modified LC-IRMS interface for the measurement of nitrogen isotope signatures from aqueous nitrate. Chromatographic separation of nitrate and consecutive reduction to elemental nitrogen was achieved and nitrogen isotope signatures were measured from injections of up to 20 µL. The system introduces a very pure analyte gas of nitrogen and helium into the IRMS, prolonging filament lifetime and reducing isobaric interferences. We measured international reference materials and in-house standards, and although a general proof of principle is shown, further evaluations and optimizations are necessary. Major challenges that should be addressed in the future include (1) reducing the nitrogen background from the eluent, (2) modifying the copper reactors to operate in parallel to enable simultaneous regeneration of oxidized copper wires and (3) reducing peak broadening by testing different column materials and optimizing flow conditions both in the liquid and gas phase. This will likely address the observed issues of low sensitivities, drifting isotope signatures over time and non-linearity of peak areas from standard injections of different concentrations and the resulting changes in $\delta^{15}N$ values. Under current conditions, measurements of in-house standards and reference materials with isotope signatures between -1.8 and 8.4‰ show that the linearity of measured $\delta^{15}N$ values are in good agreement to literature and referenced $\delta^{15}N$ values from an EA-IRMS system, if identical sample concentrations are injected. By injecting less than 20 µL of sample materials, chromatographic separation of nitrate from blank peaks is accomplished, increasing accuracy and decreasing influences of matrix interferences. Separation and measurement of both nitrite and nitrate with one measurement might even be possible if retention can be optimized. Further increasing precision, robustness and sensitivity of this system will enable fast and reliable routine measurements of nitrate isotope signatures and help to track nitrate sources, conversion and cycling in aquatic environments, although enrichment of nitrate from unpolluted water samples might still be necessary. The system further bears the potential to enable nitrogen stable isotope analysis of organic compounds via LC-IRMS with the addition of an oxidation reactor to convert organic nitrogen to nitrate.

5.6 Appendix to chapter 5

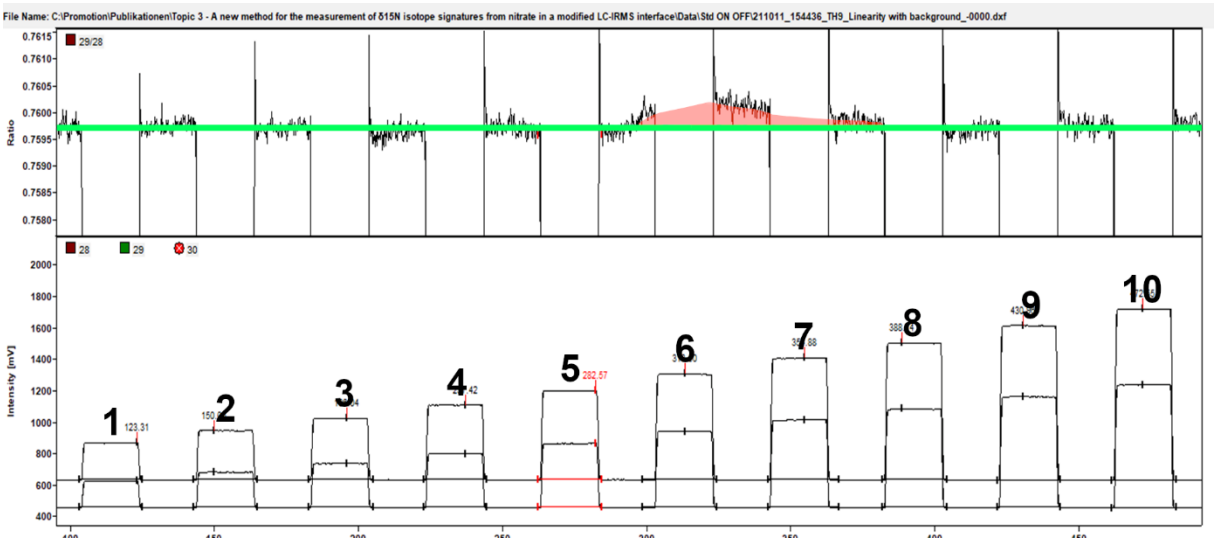

Figure 5.6: Injections of 10 reference gas peaks with open sample split and increasing gas pressure. The upper graph shows the measured m/z 29/28 ratio and the bottom graph the signal intensities (mV) over time (s). The average background m/z 29/28 ratio is indicated by a horizontal green line and a shift in m/z 29/28 ratios under the sixth peak is marked as a red area, resulting in increased $\delta^{15}N$ values of this reference gas peak in **Table 5.1**.

Chapter 6: Administration of ^{15}N-enriched ammonium chloride in a small river and δ^{15}N values of aqueous nitrate throughout the first two weeks of an isotopic tracer study

6.1 Abstract

Measuring the nitrogen stable isotope signatures of nitrate in freshwater systems is an important tool to track nitrate sources and gain a better understanding of nutrient conversion and loss through the nitrogen cycle. Previous techniques are labor intensive and there has been a recent push to enable fast and reliable δ^{15}N analysis of nitrate through online wet-chemical conversion. We developed a modified LC-IRMS interface and measured the nitrogen isotope signature of nitrate from a tracer study with isotopically enriched ammonium chloride, which was administered to a small river in western Germany. Samples needed to be pre-concentrated through vacuum evaporation to reach the sensitivity limits of the system. To our surprise, δ^{15}N values of nitrate downstream remained on natural abundance levels between -2 and +4‰ throughout the first two weeks of ammonium chloride administration, but we also observed highly enriched stable nitrogen isotope signatures of unresolved nitrogen species above 150 ‰. These could possibly be attributed to nitrite or other nitrogen oxides. Although we cannot exclude measurement errors due to the early stages of the modified interface, there is a chance that the ^{15}N-enrichment of the surrounding ecosystems was not completely achieved within two weeks of ammonium chloride administration and more time was needed for organisms to transform the labeled ammonium to nitrate.

6.2 Introduction

Nitrogen is an important component for living organisms and it is the fourth most abundant element in cellular biomass after carbon, hydrogen and oxygen [204]. Although the nitrogen content in our atmosphere is high, only small parts of less than 2 % are available for life and our ecosystems are therefore normally nitrogen limited [243]. Nitrogen is naturally assimilated and utilized by organisms through the nitrogen cycle, a series of biotic and abiotic transformation steps of organic and inorganic nitrogen species. There are still unanswered questions that impede our understanding of the nitrogen cycle and the fate of reactive nitrogen species, with contribution of rivers and streams to the global nitrogen loss being one part requiring urgent research [244, 245]. Atmospheric nitrogen is first fixed into ammonium by nitrogen fixating organisms, but although this process is of great ecological importance for the overall nitrogen balance in ecosystems, the contribution of nitrogen fixation from rivers and freshwater streams to the supply of ammonium is variable and limited [246]. A more important role for the supply of ammonium in freshwater streams is the degradation of organic nitrogen into ammonium through nitrogen mineralization, which is mediated by heterotrophic organisms under oxic or anoxic conditions. Through this process, nitrogen is regenerated from organic matter and available again for oxidation processes, which has great implications for the nutrient cycling in freshwater systems. Ammonium is oxidized stepwise to nitrite and nitrate through nitrifying bacteria and archaea, which represents a major sink for regenerated ammonium and can account for up to 30 % of ammonium utilization [247]. The produced nitrate/nitrite through nitrification is readily transported downstream into oceans or into the groundwater, but can also be reduced to gaseous nitrogen species through denitrification processes [248] or anaerobic ammonium oxidation (Anammox) [249].

The main inorganic nitrogen species in rivers are ammonium, nitrite and nitrate, with nitrate being the most stable form representing more than 80 % of inorganic nitrogen species [250]. Stable isotope techniques have been established as a useful tool to track and discriminate between nitrate sources. Terrestrial nitrogen comes in many forms and from various sources, and the nitrogen isotope signature of terrestrial nitrogen varies between -20 and +30 ‰ [218]. Synthetic fertilizers typically have $\delta^{15}N$ values of -6 to +6 ‰ [251, 252], whereas organic fertilizers like manure are isotopically enriched and have a range of +5 to +25 ‰ [253]. Nitrogen from atmospheric and soil materials have

lower $\delta^{15}N$ values, ranging from -5 to +2 ‰ for soil materials [252, 254] and -15 to +15 ‰ for atmospheric deposits [214, 215, 255, 256]. Since nitrate in rivers originates from different sources, the origin of river nitrate is reflected in its $\delta^{15}N$ value, ranging from -10 to +20 ‰. Rivers which are, e.g., heavily polluted from anthropogenic sources of nitrogen like fertilizer or wastewater treatment plants have higher nitrogen isotope signatures of nitrate compared to unpolluted rivers, where nitrate originates from natural sources [218]. A clear distinction between $\delta^{15}N$ values of natural and anthropogenic origin, however, is not always clear. Techniques to measure nitrogen isotope signatures of nitrate/nitrite from water samples require that nitrogen from nitrate and/or nitrite is quantitively converted to one gaseous nitrogen species as a measurement gas before the ratio of heavy to light isotope can be determined in an isotope ratio mass spectrometer. Nitrate and nitrite can be either combusted as silver nitrate or silver nitrite [227], bacterial strains can be utilized to digest nitrate/nitrite into N_2O [228] or reduction of nitrate to nitrite is achieved by spongy cadmium and subsequent reduction of nitrite with azides to nitrous oxide [229]. Another method describes the reduction of nitrate to ammonium with Devardas alloy [257], which is a strong reducing agent consisting of aluminum, copper and zinc. In either case, sample preparation is carried out offline and a time-consuming process, but the results can be used to quantify nitrogen uptake, transformation and cycling in freshwater streams by tracer studies [258-260]. Tracer studies are an important tool to study the fate and transformation of nitrogen species in water systems. Isotopically labeled materials, e.g., ^{15}N enriched ammonium salts are administered into a water body and samples taken regularly in the surrounding area. The labeled material is taken up and converted by microorganisms and plants, thus entering the nitrogen cycle causing a measurable increase in the $\delta^{15}N$ value of any organic or inorganic matter. The spatio-temporal distribution of enriched isotope signatures then gives insights into uptake and conversion rates of nitrogen.

Recent efforts have been made to measure nitrogen isotope signatures of nitrate online through wet chemical reactions using strong reducing agents like $Ti(III)Cl_3$ or $V(III)Cl_3$ [232-234]. In chapter 5, we presented first results of our own efforts to develop a modified LC-IRMS interface for the measurement of nitrogen isotope signature of nitrate from water samples. Although initial results were promising, problems occurred including high nitrogen background noise and system stability, which could not be fully resolved.

However, we had an opportunity to further test our system with samples from an enrichment experiment carried out in a small river in western Germany. During this experiment, isotopically enriched ammonium chloride was constantly administered to the flow of the freshwater stream and water samples were taken at different locations downstream on a weekly basis. We measured the nitrogen isotope signature of water samples after the first and second week of ammonium chloride administration. The goal was not only to verify the success of nitrogen isotope enrichment in the surrounding water stream, since we expected a quick utilization of the labeled ammonium by microorganisms and oxidation to nitrate, but also to test the system with real water samples. Although the sensitivity of the modified interface would not be sufficient to allow for direct measurement of 10 µL water sample injections, concentration of nitrate should be possible by vacuum evaporation. The enrichment experiment is an ideal proving ground, since the expected ^{15}N-enriched isotope signatures of nitrate should be well above natural abundance levels and therefore detectable even under non-optimized system conditions.

6.3 Materials and methods

6.3.1 Enrichment experiment

The river Rotbach is a small tributary of the Rhine in west Germany (51.5724°N 6.6871°E) and was used as a site for the administration of isotopically enriched ammonium chloride. A bottle of the labelled material was exposed to the river in May and June 2021 so that a constant portion leached into the stream over the course of six weeks. Water samples were taken weekly at 50, 100, 200, 300, 500, 750, 1000, 1500 and 2000 m downstream in relation to the administration point and one sample was taken 50 m upstream as a reference. Samples were frozen and stored until further use. Because we knew that the sensitivity of the modified LC-Isolink™ interface was not suitable for direct injection and measurement of nitrate from water samples, we pre-concentrated the water samples after thawing in a vacuum evaporator (Q-101 Syncore Polyvap, BÜCHI Labortechnik GmbH, Germany). 50 mL of each water sample was evaporated at 60 °C and under 50 mbar to approximately 1 mL and therefore enriched 50-fold. Separate spectroscopic measurements of ammonium, nitrite and nitrate (**Table 6.3**) showed that the nitrate concentration in the river was around 7 mgL^{-1}, which corresponds to 1.58 mgL^{-1} N.

Enriching the nitrate concentration 50-fold by vacuum evaporation would result in a concentration of ~80 mgL^{-1} N, which should fall well within the previously determined measurement range of the modified interface in chapter 5. Although the system still suffers from a non-linear shift of $\delta^{15}N$ values and peak areas, the shift should not be detrimental to the purpose of detecting enriched nitrogen isotope signatures. We further evaporated and measured a 1:50 diluted sample of in-house standard at an initial concentration of 50 mgL^{-1} N to check for isotope fractionation effects during evaporation. All samples were filtered through 0.2 µm PTFE filters after evaporation and 10 µL sample volume were directly injected into the system.

6.3.2 Chemicals and solutions

A 0.03 M solution of Vanadium(III)-chloride (97 %, Merck, Darmstadt, Germany) in 0.3 M HCl (36.5 – 38 %, Alfa Aesar, Kandel, Germany) was prepared as a reducing agent. Concentrated sulfuric acid (95-97 %, Merck, Darmstadt, Germany) was diluted to a concentration of 0.005 M and served as the eluent for chromatographic separation of nitrate. All solutions were prepared with degassed Milli-Q water and were further degassed after preparation by a membrane pump (Vacuubrand GmbH & Co., Wertheim, Germany) and in an ultrasonic bath (Sonorex RK 100 Bandelin Electronic, Berlin, Germany) and stored in a refrigerator for up to one week. A small flow of Helium 5.0 (Air Liquide, Oberhausen, Germany) was introduced into the reduction agent and eluent bottles while they were in use to prevent re-gassing of oxygen or nitrogen. 50 and 25 mgL^{-1} N-nitrate in-house standards (KNO_3 and $NaNO_3$, >99%, Merck, Darmstadt, Germany) and international reference materials USGS 32, 34 and 35 (IVA Analysentechnik GmbH & Co. KG, Meerbusch, Germany) were frequently used in between measurements for data referencing as described previously in chapter 5.

6.3.3 Instrumental setup

The Instrumental setup is identical to the one described in chapter 5 for nitrogen isotope analysis of nitrate via LC-IRMS. In short, nitrate is separated chromatographically on a Hypercarb™ PGC column (2.1 x 100 mm, 3 µm, Thermo Fisher Scientific GmbH, Bremen, Germany) with 0.005 M sulfuric acid as eluent. Column temperature was set to 60 °C and the reducing agent (0.03 M Vanadium(III)-chloride in 0.3 M HCl) was added through a T-piece made of PEEK. The eluent and reducing agent were pumped at 200 $\mu Lmin^{-1}$ by two separate HPLC pumps (Dionex Ultimate LPG-3400 SD and HPG-3200 SD, Thermo Fisher

Scientific, Bremen, Germany). Reduction of nitrate and nitrite species took place at 95 °C in a fused silica capillary (ID = 0.32 mm; length = 8 m) inside a temperature-controlled GC oven controlled by a Eurotherm 2216e microprocessor (Schneider Electric Systems, Limburg, Germany). Nitrogen oxide species were then extracted into a helium carrier gas stream through the regular gas separation units of the Isolink™ interface and reduced to elemental nitrogen in a heated copper reactor at 650°C. Residual water and carbon dioxide are removed by a cooling trap filled with liquid nitrogen before the measurement gas enters the open split of the interface and subsequent DELTA V Advantage IRMS (Thermo Fisher Scientific, Bremen, Germany). Referencing of isotope data was done by two-point normalization using the in-house nitrate standards KNO_3 and $NaNO_3$, which were already measured and referenced on an EA-IRMS system in chapter 5. Their referenced nitrogen isotope signature of 0.0 ‰ ($NaNO_3$) and 8.4 ‰ ($NaNO_3$) was used to normalize the measured nitrate isotope signature of water samples according to equation 6.1:

$$\delta^h E_{c,i-ref} = \frac{\delta^h E_{i-ref1} - \delta^h E_{i-ref2}}{\delta^h E_{m-ref1} - \delta^h E_{m-ref2}} * (\delta^h E_c - \delta^h E_{m-ref2}) + \delta^h E_{i-ref2} \quad \text{(Eq. 6.1)}$$

where $\delta^h E_c$ is the measured isotope signature of the sample compound and $\delta^h E_{i\text{-}ref}$ and $\delta^h E_{m\text{-}ref}$ are the referenced and measured isotope signatures of the reference materials.

6.4 Results

6.4.1 Sample evaporation, blank samples, and raw river water

Background nitrogen signals were elevated at up to 500 mV on the first cup (m/z 28) and originated from the mobile phase, like it was described in chapter 5. Injections of 10 µL MilliQ water (blank) into the system showed blank peaks of nitrogen gas in the IRMS system after 260 s under the used conditions, which had $\delta^{15}N$ values between +4 ‰ and +10 ‰ against the reference gas. No nitrate peak was visible in blank samples. Injecting raw river water, which was not evaporated to pre-concentrate nitrate, also showed an injection peak after 265 s and no measurable nitrate peak afterwards. The injection peak from raw water samples, however, exhibited a visible positive shift in mass 29/28 ratios leading to an increased $\delta^{15}N$ value of +91.0 ± 2.5 ‰, (**Figure 6.1**, **Table 6.1**).

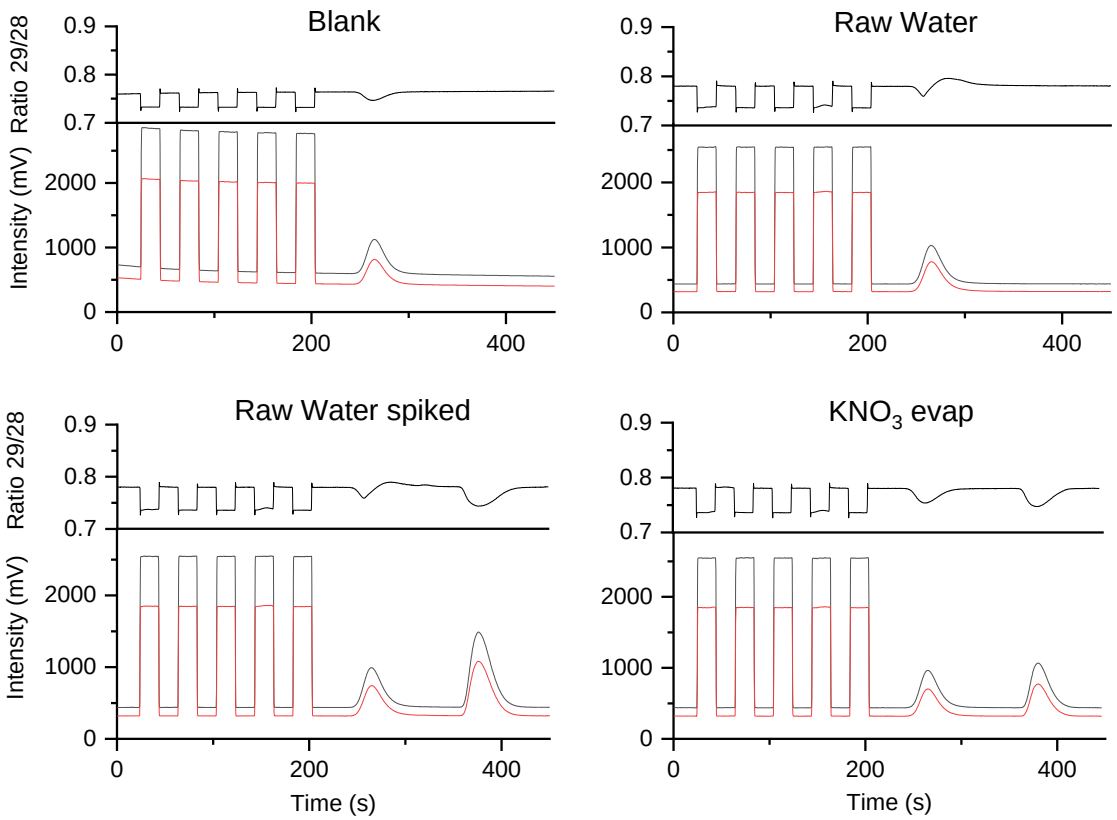

Figure 6.1: Chromatograms showing measurements of a blank sample of evaporated MilliQ water (Top left), raw river water (Top right), raw river water spiked with a nitrate standard (Bottom left) and an evaporated KNO_3 standard solutions (Bottom right). Evaporation overnight in a vacuum evaporator does not influence the 29/28 ratio of either the nitrate peak or injection peaks. The water matrix furthermore does not influence separation of nitrate, as NO_3^- in a raw water sample spiked with a nitrate standard is eluted with a similar retention time around 380 s, as observed in other measurements under these conditions.

The observed positive shift did not immediately occur with the beginning of the peak, where signal intensities started to rise, but shortly afterwards before the peak intensity reached its maximum. Spiking a raw water sample with nitrate in-house standards resulted in a nitrate peak after 376.2 s, while the positive isotope shift during the injection peak remained. To test if evaporation of nitrate solutions leads to isotope fractionation, we diluted (1:50) standard solutions of 50 mgL^{-1} KNO_3 and 25 mgL^{-1} $NaNO_3$ and evaporated 50 mL down to 1 mL sample volume. Injecting 10 µL of the evaporated standard solutions and measuring the nitrogen isotope signature showed no significant difference in $\delta^{15}N$ values compared to non-evaporated standard samples (Welch's t-tests, t_2 = -2.488, p = 0.124 for $NaNO_3$ and t_2 = 0.257, p = 0.821 for KNO_3, **Table 6.1**). The reported standard deviations for evaporated standard solutions were noticeably higher (1.7 for KNO_3 and 1.2 for $NaNO_3$) compared to normal standard solutions (0.2 for both KNO_3 and $NaNO_3$). The injection peaks of evaporated standard solutions further did not

exhibit the unusual positive shift of mass 29/28 ratio observed in water samples and the $\delta^{15}N$ values of the injection peaks remained under 10 ‰ and comparable to blank or regular standard solutions.

Table 6.1: $\delta^{15}N$ measurements of Blank samples, raw and spiked river water and standards of a 50 mgL^{-1} N solution of KNO_3 and 25 mgL^{-1} N solution of $NaNO_3$ compared to solutions which were diluted 1:50 and then evaporated as described in chapter 6.3.

Sample	N	Injection Peak			Nitrate Peak		
		Rt (s)	$\delta^{15}N$ (‰)	SD (‰)	Rt (s)	$\delta^{15}N$ (‰)	SD (‰)
Blank	3	259.3	3.9	0.3	-	-	-
KNO_3	3	264.4	6.3	0.6	348.9	-8.5	0.2
KNO_3 evap	3	265.3	5.7	0.7	380.7	-8.8	1.7
$NaNO_3$	3	264.5	5.1	0.3	349.5	-3.9	0.2
$NaNO_3$ evap	3	265.2	9.4	0.2	364.2	-2.1	1.2
Raw Water	2	265.3	91.0	2.5	-	-	-
Raw Water spiked	1	264.8	68.1	-	376.2	-0.5	-

6.4.2 River samples

We measured the nitrogen isotope signature of nitrate from concentrated river water one and two weeks after administration of isotopically enriched ammonium chloride. $\delta^{15}N$ values of river nitrate stayed between +0.4 ± 0.4 ‰ and +4.1 ± 0.3 ‰ in those two weeks, varying over a small range of 3.7 ‰ (**Figure 6.2**, **Table 6.2**). No trends in $\delta^{15}N$ values were observed either between sampling points or between weeks. A small difference in $\delta^{15}N$ can be seen for the reference point 50 m upstream from the administration point, which had a $\delta^{15}N$ value of -1.9 ± 1.6 ‰. After the second week, the reference point had a $\delta^{15}N$ value of +2.2 ± 1.7 ‰, which was well within the observed range of $\delta^{15}N$ values of nitrate downstream the administration point. The $\delta^{15}N$ values of the injection peak for all samples during that time were much higher and ranged between +164.8 ± 8.1 ‰ and +272.4 ± 1.2 ‰, but also with no observable trend either between sampling points or weeks.

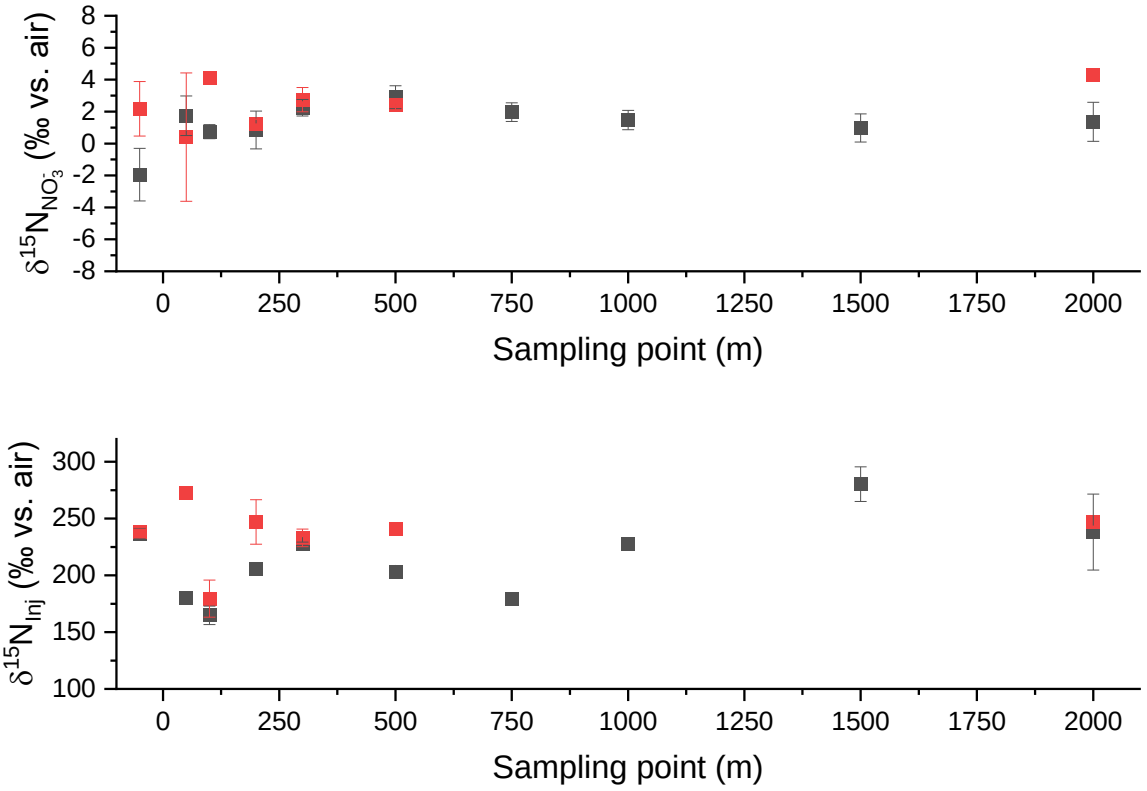

Figure 6.2: Nitrogen isotope signatures (‰ vs Air) of nitrate (NO_3^-, Top) and the injection peak (Inj., Bottom) from evaporated water samples of the river Rotbach after one week (grey squares) and two weeks (red squares) of introducing isotopically enriched ammonium chloride. Samples were taken up to 2000 m downstream of the administration point and one sample 50 m upstream as a reference. The nitrogen isotope signature of nitrate does not show any significant enrichment during this timeframe and $\delta^{15}N$ values remain between 0 and +4 ‰ except for the reference sample after one week (-2 ‰). The nitrogen isotope signature of the injection peak is well above +150 ‰ for any sample with no clear trend between sampling points.

Note that measurements during the second week only included sampling points up to 500 m downstream from the administration point and a last sample after 2000 m. The $\delta^{15}N$ values of nitrate from the last sampling point after 2000 m was still in the same range as other samples and we do not assume something would change between 500 and 2000 m that would lead to a sudden increase in $\delta^{15}N$ values. The chromatograms of evaporated river water show that something highly enriched in mass 29 is eluted from the column right after the start of the injection peak (**Figure 6.3**), as the mass 29/28 ratio shows a strong positive shift shortly after the beginning of the injection peak around 230 s, which was comparable to what we also observed in non-evaporated water samples. The sudden swing in mass 29/28 ratio during the injection peak is not visible in standard measurements and only appears while measuring samples from the river.

Table 6.2: Nitrogen isotope signatures (Avg in ‰ vs Air) and standard deviations (SD) from evaporated water samples for nitrate (NO_3) and the injection peak (Inj) on two sampling days in May 2021.

Sampling point	210518_Inj		210518_NO_3		210525_Inj		210525_NO_3	
	Avg	SD	Avg	SD	Avg	SD	Avg	SD
-50	236.7	4.7	-1.9	1.6	238.3	3.4	2.2	1.7
50	180.3	1.0	1.7	1.2	272.4	1.2	0.4	4.0
100	164.8	8.1	0.7	0.4	179.5	16.3	4.1	0.3
200	205.2	1.9	0.8	1.2	247.0	19.6	1.2	0.3
300	227.9	1.4	2.2	0.5	233.0	7.8	2.7	0.8
500	203.5	2.5	2.9	0.7	240.7	2.1	2.4	0.0
750	179.1	1.0	2.0	0.6	-	-	-	-
1000	227.9	1.9	1.5	0.6	-	-	-	-
1500	280.3	15.2	1.0	0.9	-	-	-	-
2000	238.1	33.5	1.4	1.2	247.0	-	4.3	-

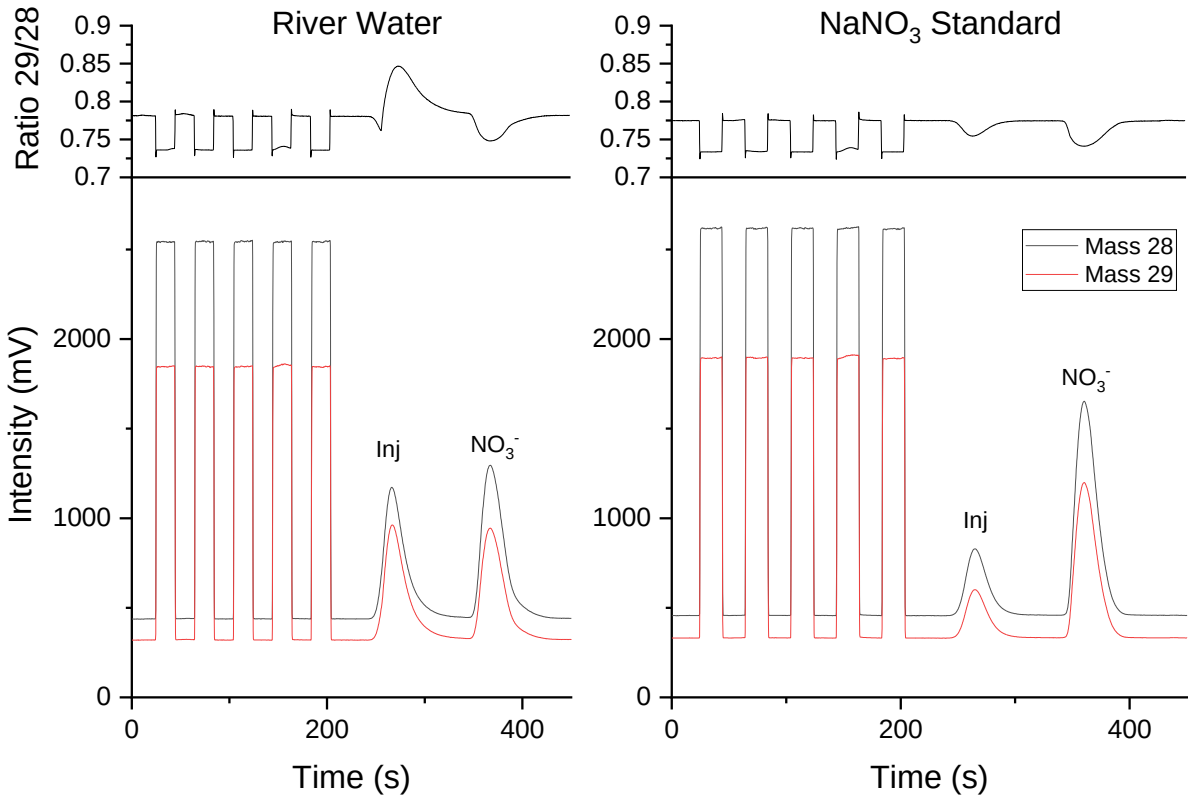

Figure 6.3: Chromatogram of evaporated river water (left) and $NaNO_3$ standard solution at 50 mgL^{-1} N (right) showing separation of nitrate from the injection peak. Lines in the bottom section represent signal intensities (mV) of m/z 28 (black) and 29 (red) for the determination of $\delta^{15}N$ values by the IRMS. The upper sections show the ratio of mass 29/28 intensities and reveal an unusual swing in the injection peak for the river water sample, which is not observed in standard samples.

6.5 Discussion

The modified interface suffers from a lack of sensitivity, not only because of the observed high nitrogen background, but also because nitrogen stable isotope measurements via N_2 as the measurement gas faces problems of lower ionization efficiencies in the ion source by electron impact (~70% compared to ionization of CO_2) and a 2:1 ratio of necessary nitrogen atoms to form one molecule of elemental nitrogen [240]. The measured nitrate concentration in the river Rotbach between 6 to 8 mgL^{-1} and resulting nitrogen concentration around 1.2 mgL^{-1} N are not measurable directly, as detection limits even for carbon rarely exceed 1 mgL^{-1} for 10 µL injection volumes [46]. Consequently, injecting raw water samples into the modified interface leads to no observable nitrate signal in the chromatogram. Increasing the injection volume can help to increase the necessary nitrogen load into the system, but it is unlikely that the system, under current conditions, will be able to measure natural nitrate concentrations from water bodies without pre-concentration.

The isotope swing observed in raw water samples during the injection peak represents an interesting result, leading to highly increased $\delta^{15}N$ values of the injection peak around ~90 ‰. This indicates that enriched nitrogen oxide species are present in the sample, which are subsequently reduced and measured as elemental nitrogen in the IRMS. In chapter 5, we evaluated the elution and separation of nitrate and nitrite with a Hypercarb PGC column. While nitrate showed good retention on the column, nitrite was much harder to retain and partly coeluted directly with the injection peak, with a little offset depending on the exact system parameters. This would indicate that the observed isotope swing during the injection peak of raw river water is caused by partial coelution of isotopically enriched nitrite. The abundance of nitrite in river water is two orders of magnitude lower compared to nitrate (**Table 6.3**) , which means that the isotope composition of nitrite in the water sample would be much higher than the measured $\delta^{15}N$ value of ~90 ‰, since it coelutes with the much more abundant nitrogen injection peak and typically has a $\delta^{15}N$ value of ~5 ‰. This is supported by measurements of evaporated river water, where the $\delta^{15}N$ value of the injection peak is even higher and reaches over +200 ‰, which would be a direct result of concentration of nitrite alongside nitrate in the sample material.

Our results suggest that concentration of nitrate in water samples via evaporation under vacuum is feasible without isotope fractionation falsifying $\delta^{15}N$ values. The measured

$\delta^{15}N$ values of evaporated and non-evaporated nitrate standards are statistically not distinguishable. It is worth noting, however, that an increase in the measurement uncertainty was observed. Although the $\delta^{15}N$ values of evaporated and non-evaporated $NaNO_3$ showed an average difference of almost ±2 ‰, no statistical difference was found due to the higher standard deviation. On the other hand, a difference of around 2 ‰ could be also caused by other interferences like the mentioned baseline shifts in chapter 5, which were also observed during these measurements and could explain the increased standard deviations from triplicate injections. Evaporation of water samples to distinguish between nitrogen isotope signatures on natural abundance levels might be a subject for future research, but our results show that it is at least suitable to distinguish between isotope signatures in an enrichment experiment.

Another surprising result was that $\delta^{15}N$ values of nitrate in river water remained on natural abundance levels. $\delta^{15}N$ values of nitrate from uncontaminated surface waters typical fall into a range between 0 and +8 ‰ [218], which matches the observed $\delta^{15}N$ values of river water measured in this study. We expected that the nitrogen stable isotope signature of river nitrate would be significantly enriched due to the introduction of isotopically enriched ammonium chloride into the river, which should be oxidized by microorganisms and enter the nitrogen cycle of the water body. Instead, we observed nitrogen stable isotope signatures of nitrate on natural abundance levels and only see an observable shift in mass 29/28 ratio and $\delta^{15}N$ values of possibly nitrite during the injection peak of the chromatogram. The range of $\delta^{15}N$ values of the injection peak was also higher compared to the range of $\delta^{15}N$ values from nitrate, but higher variances in enriched isotope signatures from tracer studies are commonly observed and more likely caused by natural processes and not by analytical errors [258]. Due to the early development stage of the modified interface, including ongoing problems like high nitrogen background and isotope shifts depending on analyte concentrations, these results are still most likely not 100 % accurate. However, the system has proven to reliably distinguish between differences in isotope signatures higher than natural abundance levels of only several permil. Injections of, e.g., international reference materials USGS 32, 34 and 35 in chapter 5 produced measured $\delta^{15}N$ values which, when plotted against literature values, resulted in a linear regression with a slope of 0.96 and show that differences in true nitrogen isotope signatures of samples are almost completely reflected in measured $\delta^{15}N$ values. The biggest problem of the interface to date

are shifts in measured $\delta^{15}N$ values for samples with different concentrations of nitrate, but these differences are below ±5 ‰ if nitrate concentrations are above 30 mgL^{-1} N (chapter 5). Concentrating the river water approximately 50 times by evaporation of 50 mL to 1 mL should result in N-NO_3 concentrations of above 50 mgL^{-1} N, given an initial nitrate concentration of ~7 mgL^{-1} NO_3 and we therefore assume that the observed $\delta^{15}N$ values of river nitrate in the measured samples are on natural abundance levels and not isotopically enriched from the experiment.

Transformation of nitrogen species in rivers is mainly associated with microbial activities. NH_3 is stepwise oxidized to NO_2^- and NO_3^- under aerobic conditions. The first step, oxidation of NH_3 to NO_2^- is facilitated by proteobacteria and archaea and is the rate-limiting step in nitrification [261-263], while the second step, oxidation of NO_2^- to NO_3^-, is solely carried out by autotrophic bacteria [264-266]. In recent years, reports on microorganism who are even capable to completely oxidize ammonia to nitrate on their own are emerging, which is energetically advantageous in contrast to a separated two-step oxidation by different stems of bacteria/archaea [264, 266]. Nitrate reduction to nitrite can be further mediated by microorganisms [267] and the resulting nitrite is mainly used in three subsequent reaction pathways: 1) dissimilatory reduction to ammonia [268], 2) reduction to gaseous nitrogen species by denitrification [269] and 3) coupled reduction to elemental nitrogen with ammonia oxidation through Anammox [263, 270, 271]. Anammox is mediated by chemoautotrophic bacteria under anaerobic conditions and converts ammonium and nitrite directly to elemental nitrogen, representing a newly found and alternative pathway for nitrogen loss in water bodies. The role of Anammox for nitrogen loss in rivers varies, but a study from an urban river assigned losses of up to 81.6 % to Anammox [272] and could be one reason why nitrate isotope signatures remain on natural abundance levels. Initial ammonium oxidation rates can be low in the water column of a river and the resulting low rates of nitrite production could be immediately used by Anammox bacteria in the anaerobic sediments of the water body to produce elemental nitrogen. The reaction rates of ammonium oxidation and nitrite oxidation are strongly dependent on the pH, where ammonium oxidation is inhibited under acidic conditions and nitrite oxidation is inhibited at higher pH [273]. Both reactions work best under neutral condition with a pH between 7.0 and 7.5. Ammonium chloride is an acidic salt, but it is hard to imagine that the low amounts of

enriched ammonium chloride influenced the pH value of the river water and therefore had any impact on the reaction rates of ammonium oxidizing bacteria/archaea. It is also questionable if other reactions like denitrification or Anammox could outpace the production of nitrate, especially since some bacteria are capable of complete oxidation of ammonium to nitrate without the need of two different strains of microorganisms [264, 266]. Another unusual observation was that water samples from the reference point 50 m upstream of the administration point of ammonium chloride also showed enriched nitrogen isotope signatures during the injection peak, which either means that part of the isotopically enriched material is transported upstream by organisms or that the isotopic baseline of the compounds causing these values are isotopically ^{15}N-enriched compared to the natural abundance level of nitrogen stable isotopes. Bulk stable isotope analysis after the enrichment experiment showed artificially enriched nitrogen isotope signatures in animal and plant matter (Nachev, M., personal communication) surrounding the administration point, which shows that the enriched ammonium was taken up and incorporated into organisms, but due to unknown reasons it does not translate into $\delta^{15}N$ values of nitrate. Our results are further in direct contrast to earlier studies conducting nitrogen tracer studies in freshwater streams with isotopically enriched ammonium chloride [258-260, 274]. It was reported that major parts of the introduced ammonium were readily taken up by organisms and nitrate was the major pool for ^{15}N transformation and uptake rates of over 50 %. Given the stark contrast of previous tracer studies and the enriched bulk $\delta^{15}N$ values of animal and plant material after the enrichment experiment to the observed $\delta^{15}N$ values of nitrate on natural abundance levels, a re-evaluation of the samples with already established methods to determine nitrate isotope signatures should be conducted to either confirm or disprove results of the modified LC-IRMS interface including the sample preparation procedure.

6.6 Appendix to chapter 6

Table 6.3: Spectroscopic determination of nitrite, nitrate and ammonium on May 25th, 2022, in the river Rotbach on sampling points up to 2000 m downstream from the administration of ^{15}N-enriched NH_4Cl

Sampling point [m]	Nitrite [mg/L]	Nitrate [mg/L]	Ammonium [mg/L]
50	0.053	7.173	0.142
100	0.055	8.175	0.120
200	0.056	7.545	0.142
750	0.045	6.478	0.072
1500	0.044	6.87	0.079
2000	0.082	6.562	0.116

Chapter 7: General conclusion and outlook

7.1 General Conclusion

LC-IRMS has been a niche analytical application since its invention in 2004 and bears analytical restraints in terms of chromatographic performance and the accessible elements. Although efforts were made to improve the scope and applicability of the system through instrumental advances and modifications [78, 79, 81, 275, 276], many scientists to date still use GC-IRMS systems even for polar compounds like amino acids. However, the analysis of amino acids is one of the main fields of LC-IRMS and chromatographic methods were quickly developed. A number of recently published studies show that this field is of ongoing scientific interest and has great potential for further advances [52-54, 176]. The strength of this application was demonstrated by measuring carbon isotope signatures of amino acids from a controlled feeding and infection experiment and for a great number of samples, since our understanding of isotope fractionation and incorporation between tissues is still limited [113]. It is known that bulk material of liver tissue adapts more quickly to changes in dietary isotope signatures compared to bulk material from muscle tissue [105, 106] and the isotope composition of most individual amino acids show a similar behaviour when fish are fed with high protein diets. Essential amino acids in fish were preferably routed from dietary sources, which is in accordance with the established literature [95, 99], but trophic fractionation of NEAAs in the liver indicate biosynthesis of amino acids from small amounts of dietary lipids, visible through multivariate analysis. It seems that even on high protein diets with little amounts of other macronutrients, metabolic activities of NEAAs are still measurable by CSIA in regular diet-consumer interactions. SIA of parasites has been of growing interest in recent years, but studies so far focused on the use of BSIA to investigate trophic positions and nutrient sources [187, 188, 277], although the potential of CSIA to investigate host-parasite systems has already been acknowledged [169]. Carbon CSIA of amino acids was applied via LC-IRMS on plerocercoids of *S. solidus* and its second intermediate host, the three-spined stickleback. The parasite resides in the hosts body cavity and passively feeds on nutrients which might originate from the hosts liver tissue or metabolism, as patterns of $\delta^{13}C$ values from EAAs over time and isotope fractionation of His in the parasite resemble those of host liver tissue. Distinct fractionation patterns between the parasite and both liver and muscle tissue of its host were identified for the EAA Thr and the NEAAs Gly and Ser, which are metabolically linked

and indicate extensive conversion as a means to ensure the rapid growth of the parasite during this life stage. The parasite accumulates huge storages of glycogen for adulteration and reproduction, and the carbon isotope signature of glucose was measured via LC-IRMS without any pre-concentration and little sample preparation, once again showing the advantage of this system in comparison to GC-IRMS for polar compounds.

The biggest drawback of the LC-IRMS system, however, might still be the limitation to only carbon isotope measurements, which limits the scope of applications and drives a lot of scientists to the more flexible GC-IRMS by default. The presented results from a modified interface for the online measurement of $\delta^{15}N$ values from small samples of nitrate not only serves as a first step towards nitrogen isotope analysis of organic nitrogen, but also has intrinsic value by measuring nitrogen isotope signatures of nitrate from surface or groundwater systems. Studies on this subject, which were conducted and published during the timeframe of this work by other groups, indicate the importance and interest in stable isotope measurements of nitrate to study the dynamics of the nitrogen cycle or source allocation of anthropogenic nitrate in areas with increased agricultural activity [232-234]. Although the modified system needs further validation and improvement, a first proof-of-principle with standard and reference materials was shown. The main difference of the modified interface, in comparison to methods developed by other groups, is that chromatographic separation of nitrate was achieved and maintained throughout the system, giving the opportunity to measure nitrate isotope signatures separate from the nitrogen background of water samples. This was especially useful during measurements from an isotope enrichment experiment in a small river, where the nitrogen isotope composition of nitrate was measured separately from other compounds like nitrite or nitrogen oxides eluting early with the injection peak. Results indicate that nitrification might not always completely lead to fast conversion of ammonium to nitrate in all zones of a small river and within two weeks of administration, but the early development stage of the modified interface still leaves room for uncertainties and measurement errors. However, separation and measurement of nitrate and nitrite isotope signatures with only one run and appropriate pre-concentration of water samples is a necessary requirement for CSIA of organic nitrogen and a future prospect of this application.

7.2 Outlook

It was pointed out on several occasions that our understanding of isotope fractionation and incorporation into consumer tissue is still limited, and more studies are needed using controlled feeding experiments to form the foundation for correct interpretation of ecological field data. We contributed to this field by conducting CSIA of amino acids in a common diet-consumer system as well as a novel approach to study host-parasite interactions. While the gained results on natural abundance levels are of great importance, the use of isotopically enriched materials in tracer studies promises to give even greater insights into metabolic pathways and nutrient transfer in complex systems. On a bigger scope, although separation of amino acids via LC-IRMS was achieved by mixed mode chromatography, the resolution of individual amino acids can still be compromised and is influenced by chromatographic conditions and matrix effects. Combining IRMS with two-dimensional liquid chromatography was already reported shortly after the introduction of the interface for amino acids [45], and recently the same idea was picked up to analyse gluconic acids from honey samples in heart-cut mode [276]. There are interesting prospects for this approach, including an improved chromatography using two HPLC columns in conjunction, but also enabling more fundamental changes to the way that chromatography works in LC-IRMS. Major chromatographic challenges in LC-IRMS are broad peaks produced throughout the system and the limitation of pure aqueous mobile phases to prevent oxidation of organic modifiers in the oxidation reactor. Both aspects might be mitigated by the use of 2D-chromatography. Methods for amino acid analysis employ a flow rate of below 300 $\mu L min^{-1}$ to facilitate ideal separation conditions on column, although the system can run a maximal flow rate of 700 $\mu L min^{-1}$ without damaging the gas separation unit. High flow rates are advantageous since they minimize the time that analytes need to flow through the system and therefore reduce peak broadening from diffusion. 2D-chromatography typically uses a low flow rate on the first dimension and a faster flow rate on the second dimension for optimal results. The first dimension in 2D-LC-IRMS could therefore employ a mixed-mode column at below 300 $\mu L min^{-1}$ for the separation of amino acids, while the second dimension uses a higher flow rate up to 700 $\mu L min^{-1}$ (minus the flow rate of the oxidation reagents) to get the analytes quickly through the rest of the system and reduce peak broadening. More importantly, the second chromatographic dimension could be used to remove matrix components from the sample in heart-cut mode or remove organic modifiers from the

eluent. Especially the latter aspect could drastically increase the range of applications, since any organic substances in the eluent must be avoided so far.

In order to improve nitrogen isotope analysis of nitrate via LC-IRMS, the individual conversion steps of nitrate reduction with V(III)Cl_3 and subsequent reduction of nitrogen oxides with elemental copper should be validated on their own, in addition to chromatographic conditions of nitrate retention and via PGC columns. The system was completely tested in a proof-of-principle concept, which makes it hard to point out sources for the observed nitrogen isotope shift on different nitrate concentrations levels. Mitigating the nitrogen background coming from the mobile phase might pose the greatest challenge, since it could be stemming from the heads of the HPLC pumps and online degassing of the eluent after the HPLC pumps is not feasible due to the high back pressure. Once the system has been optimised, a final step of wet chemical oxidation to oxidize organic nitrogen to nitrate can be implemented before the reduction of nitrate via V(III)Cl_3 to enable nitrogen isotope analysis of organic nitrogen via LC-IRMS. Previous research showed that wet chemical oxidation of nitrogen containing species can be achieved by alkaline persulfate oxidation at high pH values [278]. The employed high pH of 12 should not pose a problem for the subsequent reduction with V(III)Cl_3 under acidic conditions since the pH value significantly drops during wet chemical oxidation due to hydrolysis of persulfate at high temperatures.

The current work and recent literature prove that LC-IRMS can be a powerful tool, but general improvements are necessary to make this technique more attractive to a broader audience. Enabling the combined analysis of carbon and nitrogen isotope signatures in addition to improved chromatographic separation via 2D-LC-IRMS will lead to new perspectives in the study of polar organic compounds like amino acids, sugars and other compounds of environmental importance and show that LC-IRMS has great potential for many research fields in the future.

Chapter 8: References

1. Jochmann, M.A. and T.C. Schmidt, *Compound-specific stable isotope analysis*. 2012, Cambridge: Royal Society of Chemistry.
2. Freeman, K.H., et al., *Evidence from carbon isotope measurements for diverse origins of sedimentary hydrocarbons.* Nature, 1990. **343**(6255): p. 254-256.
3. Matthews, D.E., & Hayes, J. M. , *Isotope-ratio-monitoring gas chromatography-mass spectrometry.* Analytical chemistry, 1978. **50**(11): p. 1465-1473.
4. Krummen, M., et al., *A new concept for isotope ratio monitoring liquid chromatography/mass spectrometry.* Rapid Commun Mass Spectrom, 2004. **18**(19): p. 2260-6.
5. Morrison, D.J., K. Taylor, and T. Preston, *Strong anion-exchange liquid chromatography coupled with isotope ratio mass spectrometry using a Liquiface interface.* Rapid Commun Mass Spectrom, 2010. **24**(12): p. 1755-62.
6. van Grieken, R. and M. de Bruin, *Nomenclature for radioanalytical chemistry.* Pure & Appl. Chem., 1994. **66**(12): p. 2513-2526.
7. Erler, J., et al., *The limits of the nuclear landscape.* Nature, 2012. **486**(7404): p. 509-12.
8. McKinney, C.R., et al., *Improvements in mass spectrometers for the measurement of small differences in isotope abundance ratios.* Rev Sci Instrum, 1950. **21**(8): p. 724-30.
9. Urey, H.C., *The thermodynamic properties of isotopic substances.* J Chem Soc, 1947: p. 562-581.
10. Bigeleisen, J., *The Relative Reaction Velocities of Isotopic Molecules.* The Journal of Chemical Physics, 1949. **17**(8): p. 675-678.
11. Epstein, S., et al., *Carbonate-water isotopic temperature scale.* Geological Society of America Bulletin, 1951. **62**(4): p. 417-426.
12. Friedman, I., J. O'Neil, and G. Cebula, *Two new carbonate stable-isotope standards.* Geostandards Newsletter, 1982. **6**(1): p. 11-12.
13. Coplen, T.B., Kendall, C., & Hopple, J., *Comparison of stable isotope reference samples.* Nature, 1983. **302**(5905): p. 236-238.
14. Stichler, W., *Interlaboratory comparison of new materials for carbon and oxygen isotope ratio measurements*, in *Reference and intercomparison materials for stable isotope of light elements*. 1993, International Atomic Energy Agency: Vienna.
15. Werner, R.A. and W.A. Brand, *Referencing strategies and techniques in stable isotope ratio analysis.* Rapid Commun Mass Spectrom, 2001. **15**(7): p. 501-19.
16. Bohlke, J.K., Gwinn, C. J., & Coplen, T. B. , *New reference materials for nitrogen-isotope-ratio measurements.* Geostandards Newsletter, 1993. **17**(1): p. 159-164.
17. Coplen, T.B., Brand, W. A., Gehre, M., Gröning, M., Meijer, H. A., Toman, B., & Verkouteren, R. M., *New guidelines for δ13C measurements.* Analytical Chemistry, 2006. **78**(7): p. 2439-2441.
18. Paul, D., G. Skrzypek, and I. Forizs, *Normalization of measured stable isotopic compositions to isotope reference scales - a review.* Rapid Commun Mass Spectrom, 2007. **21**(18): p. 3006-14.
19. Godin, J.P., L.B. Fay, and G. Hopfgartner, *Liquid chromatography combined with mass spectrometry for 13C isotopic analysis in life science research.* Mass Spectrom Rev, 2007. **26**(6): p. 751-74.
20. Seltzer, A.M. and D.V. Bekaert, *A unified method for measuring noble gas isotope ratios in air, water, and volcanic gases via dynamic mass spectrometry.* International Journal of Mass Spectrometry, 2022. **478**: p. 116873.

21. Newman, A., *The Precise World of Isotope Ratio Mass Spectrometry.* Analytical Chemistry, 1996. **68**(11): p. 373A-377A.
22. Fraser, I., W. Meier-Augenstein, and R.M. Kalin, *The role of stable isotopes in human identification: a longitudinal study into the variability of isotopic signals in human hair and nails.* Rapid Commun Mass Spectrom, 2006. **20**(7): p. 1109-16.
23. Wanek, W., S. Heintel, and A. Richter, *Preparation of starch and other carbon fractions from higher plant leaves for stable carbon isotope analysis.* Rapid Commun Mass Spectrom, 2001. **15**(14): p. 1136-40.
24. Nachev, M., et al., *Understanding trophic interactions in host-parasite associations using stable isotopes of carbon and nitrogen.* Parasit Vectors, 2017. **10**(1): p. 1-9.
25. Benson, S., et al., *Forensic applications of isotope ratio mass spectrometry - a review.* Forensic Sci Int, 2006. **157**(1): p. 1-22.
26. Grassineau, N.V., D.P. Mattey, and D. Lowry, *Sulfur isotope analysis of sulfide and sulfate minerals by continuous flow-isotope ratio mass spectrometry.* Analytical chemistry, 2001. **73**(2): p. 220-225.
27. Kolthoff, I.M. and I.K. Miller, *The chemistry of persulfate. I. The kinetics and mechanism of the decomposition of the persulfate ion in aqueous medium.* Journal of the American Chemical Society, 1951. **71**(7): p. 3055-3059.
28. Tsitonaki, A., et al., *In Situ Chemical Oxidation of Contaminated Soil and Groundwater Using Persulfate: A Review.* Critical Reviews in Environmental Science and Technology, 2010. **40**(1): p. 55-91.
29. Waldemer, R.H., et al., *Oxidation of chlorinated ethenes by heat-activated persulfate: kinetics and products.* Environmental Science & Technology, 2007. **41**(3): p. 1010-1015.
30. Neta, P., et al., *Rate constants and mechanism of reaction of sulfate radical anion with aromatic compounds.* J. Am. Chem. Soc., 1977. **99**(1): p. 163-164.
31. Bender, M.M., *Variations in the 13C/12C ratios of plants in relation to the pathway of photosynthetic carbon dioxide fixation.* Phytochemistry, 1971. **10**(6): p. 1239-1244.
32. Cerling, T.E., et al., *Global vegetation change through the Miocene/Pliocene boundary.* Nature, 1997. **389**(6647): p. 153-158.
33. Cabanero, A.I., J.L. Recio, and M. Ruperez, *Liquid Chromatography Coupled to Isotope Ratio Mass Spectrometry: A New Perspective on Honey Adulteration Detection.* J. Agric. Food Chem., 2006. **54**: p. 9719−9727.
34. Elflein, L. and K.-P. Raezke, *Improved detection of honey adulteration by measuring differences between 13C/12C stable carbon isotope ratios of protein and sugar compounds with a combination of elemental analyzer - isotope ratio mass spectrometry and liquid chromatography - isotope ratio mass spectrometry (δ13C-EA/LC-IRMS).* Apidologie, 2008. **39**(5): p. 574-587.
35. Dong, H., et al., *Authenticity determination of honeys with non-extractable proteins by means of elemental analyzer (EA) and liquid chromatography (LC) coupled to isotope ratio mass spectroscopy (IRMS).* Food Chem, 2018. **240**: p. 717-724.
36. She, S., et al., *Discrimination of geographical origins of Chinese acacia honey using complex (13)C/(12)C, oligosaccharides and polyphenols.* Food Chem, 2019. **272**: p. 580-585.
37. El Hawari, K., et al., *Evaluation of honey authenticity in Lebanon by analysis of carbon stable isotope ratio using elemental analyzer and liquid chromatography coupled to isotope ratio mass spectrometry.* J Mass Spectrom, 2021. **56**(6): p. e4730.

38. Xu, J., et al., *A comprehensive analysis of (13)C isotope ratios data of authentic honey types produced in China using the EA-IRMS and LC-IRMS.* J Food Sci Technol, 2020. **57**(4): p. 1216-1232.
39. Guyon, F., et al., *Intrinsic ratios of glucose, fructose, glycerol and ethanol 13C/12C isotopic ratio determined by HPLC-co-IRMS: toward determining constants for wine authentication.* Anal Bioanal Chem, 2011. **401**(5): p. 1551-8.
40. Guyon, F., et al., *(13)C/(12)C isotope ratios of organic acids, glucose and fructose determined by HPLC-co-IRMS for lemon juices authenticity.* Food Chem, 2014. **146**: p. 36-40.
41. Suto, M. and H. Kawashima, *Compound Specific Carbon Isotope Analysis in Sake by LC/IRMS and Brewers' Alcohol Proportion.* Sci Rep, 2019. **9**(1): p. 17635.
42. Jochmann, M.A., et al., *Flow injection analysis-isotope ratio mass spectrometry for bulk carbon stable isotope analysis of alcoholic beverages.* J Agric Food Chem, 2009. **57**(22): p. 10489-96.
43. Schierbeek, H., et al., *Analysis of [U-13C6]glucose in human plasma using liquid chromatography/isotope ratio mass spectrometry compared with two other mass spectrometry techniques.* Rapid Commun Mass Spectrom, 2009. **23**(23): p. 3824-30.
44. Morrison, D.J., et al., *Quantitation of plasma 13C-galactose and 13C-glucose during exercise by liquid chromatography/isotope ratio mass spectrometry.* Rapid Commun Mass Spectrom, 2011. **25**(17): p. 2484-8.
45. Godin, J.P., et al., *Isotope ratio monitoring of small molecules and macromolecules by liquid chromatography coupled to isotope ratio mass spectrometry.* Rapid Commun Mass Spectrom, 2005. **19**(18): p. 2689-98.
46. Smith, C.I., et al., *A three-phase liquid chromatographic method for delta13C analysis of amino acids from biological protein hydrolysates using liquid chromatography-isotope ratio mass spectrometry.* Anal Biochem, 2009. **390**(2): p. 165-72.
47. Godin, J.P., et al., *Liquid and gas chromatography coupled to isotope ratio mass spectrometry for the determination of 13C-valine isotopic ratios in complex biological samples.* J Mass Spectrom, 2008. **43**(10): p. 1334-43.
48. Dunn, P.J., N.V. Honch, and R.P. Evershed, *Comparison of liquid chromatography-isotope ratio mass spectrometry (LC/IRMS) and gas chromatography-combustion-isotope ratio mass spectrometry (GC/C/IRMS) for the determination of collagen amino acid delta13C values for palaeodietary and palaeoecological reconstruction.* Rapid Commun Mass Spectrom, 2011. **25**(20): p. 2995-3011.
49. Raghavan, M., et al., *Amino acid delta13C analysis of hair proteins and bone collagen using liquid chromatography/isotope ratio mass spectrometry: paleodietary implications from intra-individual comparisons.* Rapid Commun Mass Spectrom, 2010. **24**(5): p. 541-548.
50. Lynch, A.H., J.S. McCullagh, and R.E. Hedges, *Liquid chromatography/isotope ratio mass spectrometry measurement of delta13C of amino acids in plant proteins.* Rapid Commun Mass Spectrom, 2011. **25**(20): p. 2981-8.
51. Mora, A., et al., *High-resolution palaeodietary reconstruction: Amino acid δ 13 C analysis of keratin from single hairs of mummified human individuals.* Quaternary International, 2017. **436**: p. 96-113.
52. Mora, A., et al., *Pica 8: Refining dietary reconstruction through amino acid δ 13 C analysis of tendon collagen and hair keratin.* Journal of Archaeological Science, 2018. **93**: p. 94-109.

53. Jackson, G.P., et al., *Biometrics from the carbon isotope ratio analysis of amino acids in human hair.* Sci Justice, 2015. **55**(1): p. 43-50.
54. Matos, M.P.V. and G.P. Jackson, *Compound-Specific Isotope Analysis of Human Hair: Predicting Behaviors and Biometrics beyond Dietary Factors.* Anal Chem, 2020. **92**(4): p. 3014-3022.
55. McCullagh, J., J. Gaye-Siessegger, and U. Focken, *Determination of underivatized amino acid delta(13)C by liquid chromatography/isotope ratio mass spectrometry for nutritional studies: the effect of dietary non-essential amino acid profile on the isotopic signature of individual amino acids in fish.* Rapid Commun Mass Spectrom, 2008. **22**(12): p. 1817-22.
56. Gaye-Siessegger, J., J.S. McCullagh, and U. Focken, *The effect of dietary amino acid abundance and isotopic composition on the growth rate, metabolism and tissue delta13C of rainbow trout.* Br J Nutr, 2011. **105**(12): p. 1764-71.
57. Lorrain, A., et al., *Nitrogen and carbon isotope values of individual amino acids: a tool to study foraging ecology of penguins in the Southern Ocean.* Marine Ecology Progress Series, 2009. **391**: p. 293-306.
58. Schierbeek, H., et al., *Novel method for measurement of glutathione kinetics in neonates using liquid chromatography coupled to isotope ratio mass spectrometry.* Rapid Commun Mass Spectrom, 2007. **21**(17): p. 2805-12.
59. Schierbeek, H., et al., *Simultaneous analysis of (13)C-glutathione as its dimeric form GSSG and its precursor [1-(13)C]glycine using liquid chromatography/isotope ratio mass spectrometry.* Rapid Commun Mass Spectrom, 2009. **23**(18): p. 2897-902.
60. Reinnicke, S., A. Bernstein, and M. Elsner, *Small and reproducible isotope effects during methylation with trimethylsulfonium hydroxide (TMSH): a convenient derivatization method for isotope analysis of negatively charged molecules.* Analytical chemistry, 2010. **82**(5): p. 2013-2019.
61. Kujawinski, D.M., et al., *Carbon isotope ratio measurements of glyphosate and AMPA by liquid chromatography coupled to isotope ratio mass spectrometry.* Anal Bioanal Chem, 2013. **405**(9): p. 2869-78.
62. Melsbach, A., et al., *(13)C- and (15)N-Isotope Analysis of Desphenylchloridazon by Liquid Chromatography-Isotope-Ratio Mass Spectrometry and Derivatization Gas Chromatography-Isotope-Ratio Mass Spectrometry.* Anal Chem, 2019. **91**(5): p. 3412-3420.
63. Torrento, C., et al., *Solid-phase extraction method for stable isotope analysis of pesticides from large volume environmental water samples.* Analyst, 2019. **144**(9): p. 2898-2908.
64. Limon, A.W., M. Moingt, and D. Widory, *The carbon stable isotope compositions of glyphosate and aminomethylphosphonic acid (AMPA): Improved analytical sensitivity and first application to environmental water matrices.* Rapid Commun Mass Spectrom, 2021. **35**(5): p. e9017.
65. Gilevska, T., M. Gehre, and H.H. Richnow, *Performance of the wet oxidation unit of the HPLC isotope ratio mass spectrometry system for halogenated compounds.* Anal Chem, 2014. **86**(15): p. 7252-7.
66. Franke, S., S. Kummel, and I. Nijenhuis, *Liquid chromatography/isotope ratio mass spectrometry analysis of halogenated benzoates for characterization of the underlying degradation reaction in Thauera chlorobenzoica CB-1(T).* Rapid Commun Mass Spectrom, 2018. **32**(11): p. 906-912.

67. Birkigt, J., et al., *Carbon Stable Isotope Fractionation of Sulfamethoxazole during Biodegradation by Microbacterium sp. Strain BR1 and upon Direct Photolysis.* Environ Sci Technol, 2015. **49**(10): p. 6029-36.
68. Wei, X., et al., *Characterization of phenol and cresol biodegradation by compound-specific stable isotope analysis.* Environ Pollut, 2016. **210**: p. 166-73.
69. Alberic, P., *Liquid chromatography/mass spectrometry stable isotope analysis of dissolved organic carbon in stream and soil waters.* Rapid Commun Mass Spectrom, 2011. **25**(20): p. 3012-8.
70. Scheibe, A., L. Krantz, and G. Gleixner, *Simultaneous determination of the quantity and isotopic signature of dissolved organic matter from soil water using high-performance liquid chromatography/isotope ratio mass spectrometry.* Rapid Commun Mass Spectrom, 2012. **26**(2): p. 173-80.
71. Blyth, A.J., Y. Shutova, and C. Smith, *δ13C analysis of bulk organic matter in speleothems using liquid chromatography–isotope ratio mass spectrometry.* Organic Geochemistry, 2013. **55**: p. 22-25.
72. Blyth, A.J., C.I. Smith, and R.N. Drysdale, *A new perspective on the δ13C signal preserved in speleothems using LC–IRMS analysis of bulk organic matter and compound specific stable isotope analysis.* Quaternary Science Reviews, 2013. **75**: p. 143-149.
73. Malik, A. and G. Gleixner, *Importance of microbial soil organic matter processing in dissolved organic carbon production.* FEMS Microbiol Ecol, 2013. **86**(1): p. 139-48.
74. Cabanero, A.I., J.L. Recio, and M. Ruperez, *Simultaneous stable carbon isotopic analysis of wine glycerol and ethanol by liquid chromatography coupled to isotope ratio mass spectrometry.* J Agric Food Chem, 2010. **58**(2): p. 722-8.
75. Bononi, M., G. Quaglia, and F. Tateo, *Easy Extraction Method To Evaluate delta13C Vanillin by Liquid Chromatography-Isotopic Ratio Mass Spectrometry in Chocolate Bars and Chocolate Snack Foods.* J Agric Food Chem, 2015. **63**(19): p. 4777-81.
76. Köster, D., et al., *Origin of Xylitol in Chewing Gum: A Compound-Specific Isotope Technique for the Differentiation of Corn- and Wood-Based Xylitol by LC-IRMS.* J Agric Food Chem, 2018. **66**(8): p. 2015-2020.
77. Ding, B., et al., *Authenticity determination of tea drinks in the Chinese market by liquid chromatography coupled to isotope ratio mass spectrometry.* Microchemical Journal, 2019. **144**: p. 139-143.
78. Hettmann, E., W.A. Brand, and G. Gleixner, *Improved isotope ratio measurement performance in liquid chromatography/isotope ratio mass spectrometry by removing excess oxygen.* Rapid Commun Mass Spectrom, 2007. **21**(24): p. 4135-41.
79. Fry, B., et al., *Position-specific (13) C/(12) C analysis of amino acid carboxyl groups - automated flow-injection-analysis based on reaction with ninhydrin.* Rapid Commun Mass Spectrom, 2018.
80. Fry, B. and J.F. Carter, *Stable carbon isotope diagnostics of mammalian metabolism, a high-resolution isotomics approach using amino acid carboxyl groups.* PLoS One, 2019. **14**(10): p. e0224297.
81. Marks, R.G.H., et al., *How to Couple LC-IRMS with HRMS–A Proof-of-Concept Study.* Anal Chem, 2022. **94**(6): p. 2981-2987.
82. Perini, M. and L. Bontempo, *Liquid Chromatography coupled to Isotope Ratio Mass Spectrometry (LC-IRMS): A review.* TrAC Trends in Analytical Chemistry, 2022. **147**.
83. Newsome, S.D., M.T. Clementz, and P.L. Koch, *Using stable isotope biogeochemistry to study marine mammal ecology.* Marine Mammal Science, 2010. **26**(3): p. 509-572.

84. Layman, C.A., et al., *Applying stable isotopes to examine food-web structure: an overview of analytical tools.* Biol Rev Camb Philos Soc, 2011. **87**(3): p. 545-62.
85. Larsen, T., et al., *Tracing carbon sources through aquatic and terrestrial food webs using amino acid stable isotope fingerprinting.* PLoS One, 2013. **8**(9): p. e73441.
86. Post, D.M., *Using stable isotopes to estimate trophic position: models, methods and assumptions.* Ecology, 2002. **83**(3): p. 703-718.
87. Inger, R. and S. Bearhop, *Applications of stable isotope analyses to avian ecology.* Ibis, 2008. **150**: p. 447-461.
88. McCutchan, J.H., et al., *Variation in trophic shift for stable isotope ratios of carbon,nitrogen, and sulfur.* OIKOS, 2003. **102**: p. 378-390.
89. Olive, P.J.W., et al., *Isotope trophic-step fractionation: a dynamic equilibrium model.* Journal of Animal Ecology, 2003. **72**(4): p. 608-617.
90. McMahon, K.W., et al., *Carbon and nitrogen isotope fractionation of amino acids in an avian marine predator, the gentoo penguin (Pygoscelis papua).* Ecol Evol, 2015. **5**(6): p. 1278-90.
91. Webb, E.C., et al., *Compound-specific amino acid isotopic proxies for distinguishing between terrestrial and aquatic resource consumption.* Archaeological and Anthropological Sciences, 2016. **10**(1): p. 1-18.
92. Whiteman, J.P., et al., *Amino acid isotope discrimination factors for a carnivore: physiological insights from leopard sharks and their diet.* Oecologia, 2018. **188**(4): p. 977-989.
93. Rogers, M., et al., *Assessment of two feeds on survival, proximate composition, and amino acid carbon isotope discrimination in hatchery-reared Chinook salmon.* Fisheries Research, 2019. **219**: p. 105303.
94. Wang, Y.V., et al., *(13)C values of glycolytic amino acids as indicators of carbohydrate utilization in carnivorous fish.* PeerJ, 2019. **7**: p. e7701.
95. McMahon, K.W., et al., *Carbon isotope fractionation of amino acids in fish muscle reflects biosynthesis and isotopic routing from dietary protein.* J Anim Ecol, 2010. **79**(5): p. 1132-41.
96. McMahon, K.W., et al., *Tracing carbon flow through coral reef food webs using a compound-specific stable isotope approach.* Oecologia, 2016. **180**(3): p. 809-821.
97. Wang, Y.V., et al., *Know your fish: A novel compound-specific isotope approach for tracing wild and farmed salmon.* Food Chem, 2018. **256**: p. 380-389.
98. Jim, S., et al., *Quantifying dietary macronutrient sources of carbon for bone collagen biosynthesis using natural abundance stable carbon isotope analysis.* Br J Nutr, 2006. **95**(6): p. 1055-62.
99. Newsome, S.D., et al., *Contributions of direct incorporation from diet and microbial amino acids to protein synthesis in Nile tilapia.* Functional Ecology, 2011. **25**(5): p. 1051-1062.
100. Griffiths, H., *Applications of Stable Isotope Technology in Physiological Ecology.* Functional Ecology, 1991. **5**(2): p. 254-269.
101. Lorrain, A., et al., *Differential y13C and y15N signatures among scallop tissues: implications for ecology and physiology.* Journal of Experimental Marine Biology and Ecology, 2002. **275**: p. 47-61.
102. Li, P., et al., *New developments in fish amino acid nutrition: towards functional and environmentally oriented aquafeeds.* Amino Acids, 2009. **37**(1): p. 43-53.
103. Falco, F., et al., *Amino Acids as the Main Energy Source in Fish Tissues.* Aquac Fish Stud, 2020. **3**(2): p. 1-11.

104. Boecklen, W.J., et al., *On the Use of Stable Isotopes in Trophic Ecology.* Annu. Rev. Ecol. Evol. Syst., 2011. **42**(1): p. 411-440.
105. Perga, M.E. and D. Gerdeaux, *'Are fish what they eat' all year round?* Oecologia, 2005. **144**(4): p. 598-606.
106. Sponheimer, M., et al., *Turnover of stable carbon isotopes in the muscle, liver, and breath CO2 of alpacas (Lama pacos).* Rapid Commun Mass Spectrom, 2006. **20**(9): p. 1395-9.
107. Logan, J.M. and M.E. Lutcavage, *Stable isotope dynamics in elasmobranch fishes.* Hydrobiologia, 2010. **644**(1): p. 231-244.
108. Madigan, D.J., et al., *Tissue turnover rates and isotopic trophic discrimination factors in the endothermic teleost, pacific bluefin tuna (Thunnus orientalis).* PLoS One, 2012. **7**(11): p. e49220.
109. Skinner, M.M., B.K. Cross, and B.C. Moore, *Estimating in situ isotopic turnover in Rainbow Trout (Oncorhynchus mykiss) muscle and liver tissue.* Journal of Freshwater Ecology, 2016. **32**(1): p. 209-217.
110. Kaushik, S.J. and I. Seiliez, *Protein and amino acid nutrition and metabolism in fish: current knowledge and future needs.* Aquaculture Research, 2010. **41**(3): p. 322-332.
111. Hou, Y., et al., *Amino Acid Metabolism in the Liver: Nutritional and Physiological Significance*. Vol. 1265. 2020.
112. Gannes, L.Z., D.M. O'Brien, and C.M. Del Rio, *Stable isotopes in animal ecology: assumptions, caveats and a call for more laboratory experiments.* Ecology, 1997. **78**(4): p. 1271-1276.
113. Martinez del Rio, C.M., et al., *Isotopic ecology ten years after a call for more laboratory experiments.* Biol Rev Camb Philos Soc, 2009. **84**(1): p. 91-111.
114. Hendry, A.P., et al., *Stickleback research: the now and the next.* Evolutionary Ecology Research, 2013. **15**(2): p. 111-141.
115. Fang, B., et al., *Worldwide phylogeny of three-spined sticklebacks.* Mol Phylogenet Evol, 2018. **127**: p. 613-625.
116. Kume, M. and J. Kitano, *Genetic and stable isotope analyses of threespine stickleback from the Bering and Chukchi seas.* Ichthyological Research, 2017. **64**(4): p. 478-480.
117. Reimchen, T.E., T. Ingram, and S.C. Hansen, *Assessing niche differences of sex, armour and asymmetry phenotypes using stable isotope analyses in Haida Gwaii sticklebacks.* Behaviour, 2008. **145**: p. 561-577.
118. Pinnegar, J., *Unusual stable isotope fractionation patterns observed for fish host–parasite trophic relationships.* Journal of Fish Biology, 2001. **59**(3): p. 494-503.
119. Power, M. and G.M. Klein, *Fish host-cestode parasite stable isotope enrichment patterns in marine, estuarine and freshwater fishes from northern Canada.* Isotopes Environ. Health Stud., 2004. **40**(4): p. 257-266.
120. Li, X., S. Zheng, and G. Wu, *Nutrition and metabolism of glutamate and glutamine in fish.* Amino Acids, 2020. **52**(5): p. 671-691.
121. Vander Zanden, M.J., et al., *Stable isotope turnover and half-life in animal tissues: a literature synthesis.* PLoS One, 2015. **10**(1): p. e0116182.
122. Newsome, S.D., et al., *A niche for isotopic ecology.* Front Ecol Environ, 2007. **5**(8): p. 429-436.
123. Voigt, C.C., et al., *Nutrient routing in omnivorous animals tracked by stable carbon isotopes in tissue and exhaled breath.* Oecologia, 2008. **157**(1): p. 31-40.
124. Tieszen, L.L., et al., *Fractionation and turnover of stable carbon isotopes in animal tissues: Implications for 613C analysis of diet.* Oecologia, 1983. **57**(1): p. 32-37.

125. Cerling, T.E., et al., *Determining biological tissue turnover using stable isotopes: the reaction progress variable.* Oecologia, 2007. **151**(2): p. 175-89.
126. Martínez del Rio, C. and S.A. Carleton, *How fast and how faithful: the dynamics of isotopic incorporation into animal tissues: Fig. 1.* Journal of Mammalogy, 2012. **93**(2): p. 353-359.
127. McCullagh, J.S., D. Juchelka, and R.E. Hedges, *Analysis of amino acid 13C abundance from human and faunal bone collagen using liquid chromatography/isotope ratio mass spectrometry.* Rapid Commun Mass Spectrom, 2006. **20**(18): p. 2761-8.
128. Newsome, S.D., et al., *Amino acid delta13C analysis shows flexibility in the routing of dietary protein and lipids to the tissue of an omnivore.* Integr Comp Biol, 2014. **54**(5): p. 890-902.
129. Walton, M.J. and C.B. Cowey, *Aspects of intermediary metabolism in salmonid fish.* Comp. Biochem. Physiol, 1982. **73B**(1): p. 59-79.
130. Fernandes, R., M.-J. Nadeau, and P.M. Grootes, *Macronutrient-based model for dietary carbon routing in bone collagen and bioapatite.* Archaeol Anthropol Sci, 2012. **4**(4): p. 291-301.
131. Ohkouchi, N., et al., *Biochemical and physiological bases for the use of carbon and nitrogen isotopes in environmental and ecological studies.* Progress in Earth and Planetary Science, 2015. **2**(1): p. 1-17.
132. Wu, G. and M. Morris, *Arginine metabolism: nitric oxide and beyond.* Biochem. J., 1998. **336**: p. 1-17.
133. Metges, C.C., K.J. Petzke, and U. Henning, *Gas Chromatography/Combustion/Isotope Ratio Mass Spectrometric Comparison of N-Acetyl- and N-Pivaloyl Amino Acid Esters to Measure 15N Isotopic Abundances in Physiological Samples : A Pilot Study on Amino Acid Synthesis in the Upper Gastro-intestinal Tract of Minipigs.* J. Mass Spectrom., 1996. **31**: p. 367-376.
134. Ayayee, P.A., S.C. Jones, and Z.L. Sabree, *Can (13)C stable isotope analysis uncover essential amino acid provisioning by termite-associated gut microbes?* PeerJ, 2015. **3**: p. e1218.
135. Ayayee, P.A., T. Larsen, and Z. Sabree, *Symbiotic essential amino acids provisioning in the American cockroach, Periplaneta americana (Linnaeus) under various dietary conditions.* PeerJ, 2016. **4**: p. e2046.
136. Larsen, T., et al., *The dominant detritus-feeding invertebrate in Arctic peat soils derives its essential amino acids from gut symbionts.* J Anim Ecol, 2016. **85**(5): p. 1275-85.
137. Romero-Romero, S., et al., *Abyssal deposit feeders are secondary consumers of detritus and rely on nutrition derived from microbial communities in their guts.* Sci Rep, 2021. **11**(1): p. 12594.
138. McCullagh, J.S., *Mixed-mode chromatography/isotope ratio mass spectrometry.* Rapid Commun Mass Spectrom, 2010. **24**(5): p. 483-94.
139. Tsai, Y., et al., *Histamine contents of fermented fish products in Taiwan and isolation of histamine-forming bacteria.* Food Chemistry, 2006. **98**(1): p. 64-70.
140. Landete, J.M., et al., *Updated molecular knowledge about histamine biosynthesis by bacteria.* Crit Rev Food Sci Nutr, 2008. **48**(8): p. 697-714.
141. Kanki, M., et al., *Histidine decarboxylases and their role in accumulation of histamine in tuna and dried saury.* Appl Environ Microbiol, 2007. **73**(5): p. 1467-73.
142. Fernandez-Salguero, J. and I.M. Mackie, *Histidine metabolism in mackerel (Scomber scombrus). Studies on histidine decarboxylase activity and histamine formation during*

storage of flesh and liver under sterile and non-sterile conditions. J. Fd Technol., 1979. **14**(2): p. 131-139.
143. Sánchez-Muros, M.-J., F.G. Barroso, and F. Manzano-Agugliaro, *Insect meal as renewable source of food for animal feeding: a review.* Journal of Cleaner Production, 2014. **65**: p. 16-27.
144. Khan, M.A., *Histidine Requirement of Cultivable Fish Species: A Review.* Oceanogr Fish Open Access J, 2018. **8**(5): p. 1-7.
145. Hatch, K.A., *The Use and Application of Stable Isotope Analysis to the Study of Starvation, Fasting, and Nutritional Stress in Animals*, in *Comparative Physiology of Fasting, Starvation, and Food Limitation*. 2012. p. 337-364.
146. Bertinetto, C., J. Engel, and J. Jansen, *ANOVA simultaneous component analysis: A tutorial review.* Anal Chim Acta X, 2020. **6**: p. 100061.
147. Nogales-Mérida, S., et al., *Insect meals in fish nutrition.* Reviews in Aquaculture, 2018. **11**(4): p. 1080-1103.
148. Thongprajukaew, K., et al., *Freeze-dried forms of mosquito larvae for feeding of Siamese fighting fish (Betta splendensRegan, 1910).* Aquaculture Research, 2018. **50**(1): p. 296-303.
149. Kuris, A.M., et al., *Ecosystem energetic implications of parasite and free-living biomass in three estuaries.* Nature, 2008. **454**(7203): p. 515-8.
150. Dobson, A., et al., *Homage to Linnaeus: How many parasites? How many hosts?* Proceedings of the National Academy of Sciences,, 2008. **105**: p. 11482-11489.
151. Lafferty, K.D., A. Dobson, and A.M. Kuris, *Parasites dominate food web links.* Proceedings of the National Academy of Sciences, 2006. **103**(30): p. 11211-11216.
152. Amundsen, P.A., et al., *Food web topology and parasites in the pelagic zone of a subarctic lake.* J Anim Ecol, 2009. **78**(3): p. 563-72.
153. Thompson, R.M., K.N. Mouritsen, and R. Poulin, *Importance of parasites and their life cycle characteristics in determining the structure of a large marine food web.* Journal of Animal Ecology, 2005. **74**(1): p. 77-85.
154. Thieltges, D.W., et al., *Parasites as prey in aquatic food webs: implications for predator infection and parasite transmission.* Oikos, 2013. **122**(10): p. 1473-1482.
155. Sato, T., et al., *Nematomorph parasites drive energy flow through a riparian ecosystem.* Ecology, 2011. **92**(1): p. 201-207.
156. Lafferty, K.D. and A.M. Kuris, *Trophic strategies, animal diversity and body size.* TRENDS in Ecology & Evolution, 2002. **17**(11): p. 507 - 513.
157. Timi, J.T. and R. Poulin, *Why ignoring parasites in fish ecology is a mistake.* Int J Parasitol, 2020. **50**(10-11): p. 755-761.
158. Barber, I. and P.A. Svensson, *Effects of experimental Schistocephalus solidus infections on growth, morphology and sexual development of female three-spined sticklebacks, Gasterosteus aculeatus.* Parasitology, 2003. **126**(Pt 4): p. 359-67.
159. Scharsack, J.P., K. Koch, and K. Hammerschmidt, *Who is in control of the stickleback immune system: interactions between Schistocephalus solidus and its specific vertebrate host.* Proc Biol Sci, 2007. **274**(1629): p. 3151-8.
160. Hopkins, C.A., *Studies on Cestode Metabolism. I. Glycogen Metabolism in Schistocephalus solidus In vivo.* The Journal of Parasitology, 1950. **36**(4): p. 384-390.
161. Körting, W. and J. Barrett, *Carbohydrate catabolism in the plerocercoids of Schistocephalus solidus (Cestoda: Pseudophyllidea).* International journal for parasitology, 1977. **7**(5): p. 411-417.

162. Hebert, F.O., et al., *Major host transitions are modulated through transcriptome-wide reprogramming events in Schistocephalus solidus, a threespine stickleback parasite.* Mol Ecol, 2017. **26**(4): p. 1118-1130.
163. Berger, C.S., et al., *The parasite Schistocephalus solidus secretes proteins with putative host manipulation functions.* Parasit Vectors, 2021. **14**(1): p. 436.
164. Jolles, J.W., et al., *Schistocephalus parasite infection alters sticklebacks' movement ability and thereby shapes social interactions.* Sci Rep, 2020. **10**(1): p. 12282.
165. Scharsack, J.P., et al., *Climate change facilitates a parasite's host exploitation via temperature-mediated immunometabolic processes.* Glob Chang Biol, 2021. **27**(1): p. 94-107.
166. Kochneva, A., E. Borvinskaya, and L. Smirnov, *Zone of Interaction Between the Parasite and the Host: Protein Profile of the Body Cavity Fluid of Gasterosteus aculeatus L. Infected with the Cestode Schistocephalus solidus (Muller, 1776).* Acta Parasitol, 2021. **66**(2): p. 569-583.
167. Barber, I. and J.P. Scharsack, *The three-spined stickleback-Schistocephalus solidus system: an experimental model for investigating host-parasite interactions in fish.* Parasitology, 2010. **137**(3): p. 411-24.
168. Weber, J.N., et al., *Recent evolution of extreme cestode growth suppression by a vertebrate host.* Proc Natl Acad Sci U S A, 2017. **114**(25): p. 6575-6580.
169. Sabadel, A.J.M., A.D. Stumbo, and C.D. MacLeod, *Stable-isotope analysis: a neglected tool for placing parasites in food webs.* J Helminthol, 2019. **93**(1): p. 1-7.
170. Hayes, J.M., *Factors controlling 13C contents of sedimentary organic compounds: Principles and evidence.* Marine Geology, 1993. **113**: p. 111-125.
171. France, R.L., *Differentiation between littoral and pelagic food webs in lakes using stable carbon isotopes.* Limnology and Oceanography, 1995. **40**(7): p. 1310-1313.
172. O'Connell, T.C., *'Trophic' and 'source' amino acids in trophic estimation: a likely metabolic explanation.* Oecologia, 2017. **184**(2): p. 317-326.
173. Liu, H.-z., L. Luo, and D.-l. Cai, *Stable carbon isotopic analysis of amino acids in a simplified food chain consisting of the green alga Chlorella spp., the calanoid copepod Calanus sinicus, and the Japanese anchovy (Engraulis japonicus).* Canadian Journal of Zoology, 2018. **96**(1): p. 23-30.
174. Choy, K., et al., *Investigation of amino acid δ13C signatures in bone collagen to reconstruct human palaeodiets using liquid chromatography–isotope ratio mass spectrometry.* Geochimica et Cosmochimica Acta, 2010. **74**(21): p. 6093-6111.
175. Honch, N.V., J.S. McCullagh, and R.E. Hedges, *Variation of bone collagen amino acid delta13C values in archaeological humans and fauna with different dietary regimes: developing frameworks of dietary discrimination.* Am J Phys Anthropol, 2012. **148**(4): p. 495-511.
176. Matos, M.P.V., et al., *Analysis of the (13)C isotope ratios of amino acids in the larvae, pupae and adult stages of Calliphora vicina blow flies and their carrion food sources.* Anal Bioanal Chem, 2018. **410**(30): p. 7943-7954.
177. Bontempo, L., et al., *Bulk and compound-specific stable isotope ratio analysis for authenticity testing of organically grown tomatoes.* Food Chem, 2020. **318**: p. 126426.
178. Hesse, T., et al., *Insights into amino acid fractionation and incorporation by compound-specific carbon isotope analysis of three-spined sticklebacks.* Sci Rep, 2022. **12**(1): p. 11690.
179. Smyth, J.D., *Fertilization of Schistocephalus solidus in vitro.* Exp Parasitol., 1954. **3**(1): p. 64-71.

180. Schärer, L. and C. Wedekind, *Lifetime reproductive output in a hermaphrodite cestode when reproducing alone or in pairs.* Evolutionary Ecology, 1999. **13**: p. 381-194.
181. Boschker, H.T., et al., *A versatile method for stable carbon isotope analysis of carbohydrates by high-performance liquid chromatography/isotope ratio mass spectrometry.* Rapid Commun Mass Spectrom, 2008. **22**(23): p. 3902-8.
182. Carleton, S.A. and C.M. Del Rio, *Growth and catabolism in isotopic incorporation: a new formulation and experimental data.* Functional Ecology, 2010. **24**(4): p. 805-812.
183. Grey, J., *Trophic fractionation and the effects of diet switch on the carbon stable isotopic 'signatures' of pelagic consumers.* SIL Proceedings, 1922-2010, 2000. **27**(5): p. 3187-3191.
184. Danfaer, A., *Nutrient metabolism and utilization in the liver.* Livestock Production Science, 1994. **39**: p. 115-127.
185. Read, C.P. and J.E. Simmons, *Biochemistry and Physiology of Tapeworms.* Physiological Reviews, 1963. **43**(2): p. 263-305.
186. Kanaya, G., et al., *Application of stable isotopic analyses for fish host–parasite systems: an evaluation tool for parasite-mediated material flow in aquatic ecosystems.* Aquatic Ecology, 2019. **53**(2): p. 217-232.
187. Gilbert, B.M., et al., *You are how you eat: differences in trophic position of two parasite species infecting a single host according to stable isotopes.* Parasitol Res, 2020. **119**(4): p. 1393-1400.
188. Gilbert, B.M., et al., *Stable isotope analysis spills the beans about spatial variance in trophic structure in a fish host - parasite system from the Vaal River System, South Africa.* Int J Parasitol Parasites Wildl, 2020. **12**: p. 134-141.
189. Felig, P., *The glucose-alanine cycle.* Metabolism, 1973. **22**(2): p. 179-207.
190. Dale, R.A., *Catabolism of threonine in mammals by coupling of L-threonine 3-dehydrogenase with 2-amino-3-oxobutyrate-CoA ligase.* Biochimica et Biophysica Acta, 1978. **544**(3): p. 496-503.
191. Jordan, P.M. and M. Akhtar, *The Mechanism of Action of Serine Transhydroxymethylase.* Biochem. J., 1970. **116**: p. 277-286.
192. Linstead, D.J., R.A. Klein, and G.A.M. Cross, *Threonine Catabolism in Trypanosoma brucei.* Journal of General Microbiology, 1977. **101**: p. 243-251.
193. Kikuchi, G., et al., *Glycine cleavage system: reaction mechanism, physiological significance, and hyperglycinemia.* Proc. Jpn. Acad., 2008. **84**.
194. Locasale, J.W., *Serine, glycine and one-carbon units: cancer metabolism in full circle.* Nat Rev Cancer, 2013. **13**(8): p. 572-83.
195. Kalhan, S.C. and R.W. Hanson, *Resurgence of serine: an often neglected but indispensable amino Acid.* J Biol Chem, 2012. **287**(24): p. 19786-91.
196. Sweeting, C.J., N.V. Polunin, and S. Jennings, *Effects of chemical lipid extraction and arithmetic lipid correction on stable isotope ratios of fish tissues.* Rapid Commun Mass Spectrom, 2006. **20**(4): p. 595-601.
197. Tarallo, A., et al., *A theoretical evaluation of the respiration rate partition in the Gasterosteus aculeatus-Schistocephalus solidus host-parasite system.* International Aquatic Research, 2021. **13**(3): p. 185.
198. Takizawa, Y., et al., *A new insight into isotopic fractionation associated with decarboxylation in organisms: implications for amino acid isotope approaches in biogeoscience.* Progress in Earth and Planetary Science, 2020. **7**(1).
199. Ron-Harel, N., et al., *T Cell Activation Depends on Extracellular Alanine.* Cell Rep, 2019. **28**(12): p. 3011-3021 e4.

200. Wang, W., et al., *Glycine metabolism in animals and humans: implications for nutrition and health.* Amino Acids, 2013. **45**(3): p. 463-77.
201. Mathis, D. and S.E. Shoelson, *Immunometabolism: an emerging frontier.* Nat Rev Immunol, 2011. **11**(2): p. 81.
202. Guo, C., et al., *Live Edwardsiella tarda vaccine enhances innate immunity by metabolic modulation in zebrafish.* Fish Shellfish Immunol, 2015. **47**(2): p. 664-73.
203. Peuss, R., et al., *Adaptation to low parasite abundance affects immune investment and immunopathological responses of cavefish.* Nat Ecol Evol, 2020. **4**(10): p. 1416-1430.
204. Stein, L.Y. and M.G. Klotz, *The nitrogen cycle.* Curr Biol, 2016. **26**(3): p. R94-8.
205. Benkovitz, C.M., et al., *Global gridded inventories of anthropogenic emissions of sulfur and nitrogen.* Journal of Geophysical Research: Atmospheres, 1996. **101**(D22): p. 29239-29253.
206. Galloway, J.N., *Acid Deposition: Perspectives in Time and Space.* Water, Air, and Soil Pollution, 1995. **85**: p. 15-24.
207. Aber, J., et al., *Nitrogen Saturation in Temperate Forest Ecosystems.* BioScience, 1998. **48**(11): p. 921-934.
208. Khan, M.N. and F. Mohammad, *Eutrophication: Challenges and Solutions*, in *Eutrophication: Causes, Consequences and Control*. 2014. p. 1-15.
209. Lassaletta, L., et al., *Agriculture-induced increase in nitrate concentrations in stream waters of a large Mediterranean catchment over 25 years (1981-2005).* Sci Total Environ, 2009. **407**(23): p. 6034-43.
210. De Girolamo, A.M., et al., *Developing a nitrogen load apportionment tool: Theory and application.* Agricultural Water Management, 2019. **226**.
211. Ward, M.H., et al., *Drinking Water Nitrate and Human Health: An Updated Review.* Int J Environ Res Public Health, 2018. **15**(7).
212. Smil, V., *Nitrogen in crop production: An account of global flows.* Global Biogeochemical Cycles, 1999. **13**(2): p. 647-662.
213. Mayer, B., et al., *Sources of Nitrate in Rivers Draining Sixteen Watersheds in the Northeastern US: Isotopic Constraints.* Biogeochemistry, 2002. **57**(1): p. 171-197.
214. Pardo, L.H., et al., *Evaluating the source of streamwater nitrate using ?15N and ?18O in nitrate in two watersheds in New Hampshire, USA.* Hydrological Processes, 2004. **18**(14): p. 2699-2712.
215. Kellman, L.M., *A study of tile drain nitrate - ?15N values as a tool for assessing nitrate sources in an agricultural region.* Nutrient Cycling in Agroecosystems, 2005. **71**(2): p. 131-137.
216. Panno, S.V., et al., *Isotopic evidence of nitrate sources and denitrification in the Mississippi River, Illinois.* J Environ Qual, 2006. **35**(2): p. 495-504.
217. Xu, S., P. Kang, and Y. Sun, *A stable isotope approach and its application for identifying nitrate source and transformation process in water.* Environ Sci Pollut Res Int, 2016. **23**(2): p. 1133-48.
218. Xue, D., et al., *Present limitations and future prospects of stable isotope methods for nitrate source identification in surface- and groundwater.* Water Res, 2009. **43**(5): p. 1159-70.
219. Wunderlich, A., R. Meckenstock, and F. Einsiedl, *Effect of different carbon substrates on nitrate stable isotope fractionation during microbial denitrification.* Environ Sci Technol, 2012. **46**(9): p. 4861-8.
220. Rohde, M.M., et al., *Coupled nitrate N and O stable isotope fractionation by a natural marine plankton consortium.* Frontiers in Marine Science, 2015. **2**.

221. Marconi, D., M.A. Weigand, and D.M. Sigman, *Nitrate isotopic gradients in the North Atlantic Ocean and the nitrogen isotopic composition of sinking organic matter.* Deep Sea Research Part I: Oceanographic Research Papers, 2019. **145**: p. 109-124.
222. Fripiat, F., et al., *The isotope effect of nitrate assimilation in the Antarctic Zone: Improved estimates and paleoceanographic implications.* Geochimica et Cosmochimica Acta, 2019. **247**: p. 261-279.
223. Peng, X., et al., *Nitrogen uptake and nitrification in the subarctic North Atlantic Ocean.* Limnology and Oceanography, 2018. **63**(4): p. 1462-1487.
224. Dähnke, K., et al., *Stable isotope composition and turnover of nitrate in the German Bight.* Marine Ecology Progress Series, 2010. **408**: p. 7-18.
225. Sherwood, O.A., et al., *Stable isotope ratios in seawater nitrate reflect the influence of Pacific water along the northwest Atlantic margin.* Biogeosciences, 2021. **18**(15): p. 4491-4510.
226. Tamelander, T., et al., *Base-line variations in stable isotope values in an Arctic marine ecosystem: effects of carbon and nitrogen uptake by phytoplankton.* Hydrobiologia, 2009. **630**(1): p. 63-73.
227. Silva, S.R., et al., *A new method for collection of nitrate from fresh water and the analysis of nitrogen and oxygen isotope ratios.* Journal of Hydrology, 2000. **228**: p. 22-36.
228. Sigman, D.M., et al., *A Bacterial Method for the Nitrogen Isotopic Analysis of Nitrate in Seawater and Freshwater.* Anal Chem, 2001. **73**(17): p. 4145-4153.
229. McIlvin, M.R. and M.A. Altabet, *Chemical Conversion of Nitrate and Nitrite to Nitrous Oxide for Nitrogen and Oxygen Isotopic Analysis in Freshwater and Seawater.* Anal Chem, 2005. **77**: p. 5589-5595.
230. Stange, C.F., et al., *Automated and rapid online determination of 15N abundance and concentration of ammonium, nitrite, or nitrate in aqueous samples by the SPINMAS technique.* Isotopes Environ Health Stud, 2007. **43**(3): p. 227-36.
231. Russow, R., *Determination of 15N in 15N-Enriched Nitrite and Nitrate in Aqueous Samples by Reaction Continuous-flow Quadrupole Mass Spectrometry.* Rapid Commun Mass Spectrom, 1999. **13**: p. 1334-1338.
232. Eschenbach, W., et al., *Measuring (15)N Abundance and Concentration of Aqueous Nitrate, Nitrite, and Ammonium by Membrane Inlet Quadrupole Mass Spectrometry.* Anal Chem, 2017. **89**(11): p. 6076-6081.
233. Eschenbach, W., R. Well, and J. Dyckmans, *NO Reduction to N2O Improves Nitrate (15)N Abundance Analysis by Membrane Inlet Quadrupole Mass Spectrometry.* Anal Chem, 2018. **90**(19): p. 11216-11218.
234. Dyckmans, J., et al., *Nitrogen isotope analysis of aqueous ammonium and nitrate by membrane inlet isotope ratio mass spectrometry (MIRMS) at natural abundance levels.* Rapid Commun Mass Spectrom, 2021. **35**(10): p. e9077.
235. Braman, R.S. and S.A. Hendrix, *Nanogram nitrite and nitrate determination in environmental and biological materials by vanadium (III) reduction with chemiluminescence detection.* Analytical chemistry, 1989. **61**(24): p. 2715-2718.
236. Centi, G. and S. Perathoner, *Nature of active species in copper-based catalysts and their chemistry of transformation of nitrogen oxides.* Applied Catalysis A: General, 1995. **132**(2): p. 179-259.
237. Merritt, S.A. and J.M. Hayes, *Nitrogen Isotopic Analyses by Isotope-RatioMonitoring Gas Chromatography/ Mass Spectrometry.* J Am Soc Mass Spectrom, 1994. **5**: p. 387-397.

238. Takeuchi, T., T. Kojima, and T. Miwa, *Ion chromatography of inorganic anions on graphitic carbon as the stationary phase.* Journal of High Resolution Chromatography, 2000. **23**(10): p. 590-594.
239. Mercier, J.P., et al., *Liquid chromatography analysis of phosphonic acids on porous graphitic carbon stationary phase with evaporative light-scattering and mass spectrometry detection.* Journal of Chromatography A, 1999. **849**(1): p. 197-207.
240. Brand, W.A., A.R. Tegtmeyer, and A. Hilkert, *Compound-specific isotope analysis: extending toward 15N/14N and 18O/16O.* Org. Geochem., 1994. **21**(6/7): p. 585-594.
241. Godin, J.P. and J.S. McCullagh, *Review: Current applications and challenges for liquid chromatography coupled to isotope ratio mass spectrometry (LC/IRMS).* Rapid Commun Mass Spectrom, 2011. **25**(20): p. 3019-28.
242. He, B., et al., *Assessment of global nitrogen pollution in rivers using an integrated biogeochemical modeling framework.* Water Res, 2011. **45**(8): p. 2573-86.
243. Galloway, J.N., *The global nitrogen cycle: changes and consequences.* Environmental pollution, 1998. **102**(1): p. 15-24.
244. Galloway, J.N., et al., *Transformation of the nitrogen cycle: recent trends, questions, and potential solutions.* Science, 2008. **320**(5878): p. 889-92.
245. Xia, X., et al., *The cycle of nitrogen in river systems: sources, transformation, and flux.* Environ Sci Process Impacts, 2018. **20**(6): p. 863-891.
246. Li, Y., et al., *N2 fixation in urbanization area rivers: spatial-temporal variations and influencing factors.* Environ Sci Pollut Res Int, 2020. **27**(7): p. 7211-7221.
247. Peterson, B.J., et al., *Control of nitrogen export from watersheds by headwater streams.* Science, 2001. **292**(5514): p. 86-90.
248. Laursen, A.E. and S.P. Seitzinger, *Diurnal patterns of denitrification, oxygen consumption and nitrous oxide production in rivers measured at the whole-reach scale.* Freshwater Biology, 2004. **49**(11): p. 1448-1458.
249. Kartal, B., et al., *How to make a living from anaerobic ammonium oxidation.* FEMS Microbiol Rev, 2013. **37**(3): p. 428-61.
250. Xia, X.H., et al., *Nitrification in natural waters with high suspended-solid content--a study for the Yellow River.* Chemosphere, 2004. **57**(8): p. 1017-29.
251. Bateman, A.S. and S.D. Kelly, *Fertilizer nitrogen isotope signatures.* Isotopes Environ Health Stud, 2007. **43**(3): p. 237-47.
252. Singleton, M.J., et al., *Saturated zone denitrification: potential for natural attenuation of nitrate contamination in shallow groundwater under dairy operations.* Environmental science & technology, 2007. **41**(3): p. 759-765.
253. Choi, W.-J., et al., *Impact of land-use types on nitrate concentration and δ15N in unconfined groundwater in rural areas of Korea.* Agriculture, Ecosystems & Environment, 2007. **120**(2-4): p. 259-268.
254. Williard, K.W., DeWalle, D. R., Edwards, P. J., & Sharpe, W. E. , *18O isotopic separation of stream nitrate sources in mid-Appalachian forested watersheds.* Journal of Hydrology, 2001. **252**(1-4): p. 174-188.
255. Spoelstra, J., et al., *Tracing the Sources of Exported Nitrate in the Turkey Lakes Watershed Using 15 N/ 14 N and 18 O/ 16 O isotopic ratios.* Ecosystems, 2001. **4**(6): p. 536-544.
256. Zhang, Y., et al., *Nitrogen inputs and isotopes in precipitation in the North China Plain.* Atmospheric Environment, 2008. **42**(7): p. 1436-1448.

257. Sigman, D.M., et al., *Natural abundance-level measurement of the nitrogen isotopic composition of oceanic nitrate: an adaptation of the ammonia diffusion method.* Marine chemistry, 1997. **57**(3-4): p. 227-242.
258. Peterson, B.J., M. Bahr, and G.W. Kling, *A tracer investigation of nitrogen cycling in a pristine tundra river.* Canadian Journal of Fisheries and Aquatic Sciences, 1997. **54**(10): p. 2361-2367
259. Hamilton, S.K., et al., *Nitrogen uptake and transformation in a midwestern US stream: a stable isotope enrichment study.* Biogeochemistry, 2001. **54**(3): p. 297-340.
260. Ashkenas, L.R., et al., *A stable isotope tracer study of nitrogen uptake and transformation in an old-growth forest stream.* Ecology, 2004. **85**(6): p. 1725-1739.
261. Nicol, G.W. and C. Schleper, *Ammonia-oxidising Crenarchaeota: important players in the nitrogen cycle?* Trends Microbiol, 2006. **14**(5): p. 207-12.
262. Erguder, T.H., et al., *Environmental factors shaping the ecological niches of ammonia-oxidizing archaea.* FEMS Microbiol Rev, 2009. **33**(5): p. 855-69.
263. Stahl, D.A. and J.R. de la Torre, *Physiology and diversity of ammonia-oxidizing archaea.* Annu Rev Microbiol, 2012. **66**: p. 83-101.
264. Daims, H., et al., *Complete nitrification by Nitrospira bacteria.* Nature, 2015. **528**(7583): p. 504-9.
265. Lucker, S., et al., *Nitrotoga-like bacteria are previously unrecognized key nitrite oxidizers in full-scale wastewater treatment plants.* ISME J, 2015. **9**(3): p. 708-20.
266. van Kessel, M.A., et al., *Complete nitrification by a single microorganism.* Nature, 2015. **528**(7583): p. 555-9.
267. Lam, P. and M.M. Kuypers, *Microbial nitrogen cycling processes in oxygen minimum zones.* Ann Rev Mar Sci, 2011. **3**: p. 317-45.
268. Woods, D.D., *The reduction of nitrate to ammonia by Clostridium welchii.* Biochemical Journal, 1938. **32**(11): p. 2000.
269. Galloway, J.N., et al., *Nitrogen cycles: past, present, and future.* Biogeochemistry, 2004. **70**(2): p. 153-226.
270. Hu, B.L., et al., *Distribution and diversity of anaerobic ammonium-oxidizing bacteria in the sediments of the Qiantang River.* Environ Microbiol Rep, 2012. **4**(5): p. 540-7.
271. Zhang, S., et al., *Potential roles of anaerobic ammonium oxidation (anammox) in overlying water of rivers with suspended sediments.* Biogeochemistry, 2017. **132**(3): p. 237-249.
272. Cheng, L., et al., *Dissimilatory nitrate reduction processes in sediments of urban river networks: Spatiotemporal variations and environmental implications.* Environ Pollut, 2016. **219**: p. 545-554.
273. Le, T.T.H., J. Fettig, and G. Meon, *Kinetics and simulation of nitrification at various pH values of a polluted river in the tropics.* Ecohydrology & Hydrobiology, 2019. **19**(1): p. 54-65.
274. Gribsholt, B., et al., *Nitrogen processing in a tidal freshwater marsh: A whole-ecosystem 15N labeling study.* Limnology and Oceanography, 2005. **50**(6): p. 1945-1959.
275. Godin, J.P., G. Hopfgartner, and L. Fay, *Temperature-Programmed High-Performance Liquid Chromatography Coupled to Isotope Ratio Mass Spectrometry.* Anal. Chem., 2008. **80**: p. 7144‑7152.
276. Suto, M., H. Kawashima, and N. Suto, *Heart-cutting two-dimensional liquid chromatography combined with isotope ratio mass spectrometry for the determination*

of stable carbon isotope ratios of gluconic acid in honey. J Chromatogr A, 2019. **1608**: p. 460421.

277. Sures, B., et al., *The monogenean Paradiplozoon ichthyoxanthon behaves like a micropredator on two of its hosts, as indicated by stable isotopes.* J Helminthol, 2019. **93**(1): p. 71-75.
278. Köster, D., *Applications for liquid chromatography coupled to isotope ratio mass spectrometry and evaluation of the oxidation processes towards compound specific δ 15N analysis*, in *Faculty of Chemistry*. 2020, University of Duisburg-Essen.

Chapter 9: Appendix

9.1 List of figures

Figure 6.3: Chromatogram of evaporated river water (left) and $NaNO_3$ standard solution at 50 mgL^{-1} N (right) showing separation of nitrate from the injection peak. Lines in the bottom section represent signal intensities (mV) of m/z 28 (black) and 29 (red) for the determination of $\delta^{15}N$ values by the IRMS. The upper sections show the ratio of mass 29/28 intensities and reveal an unusual swing in the injection peak for the river water sample, which is not observed in standard samples. 112

9.2 List of tables

9.3 List of abbreviations and symbols

AA	Amino acid
Asp	Asparagine
Arg	Arginine
Ala	Alanine
Asx	Aspartic acid and asparagine
ANOVA	Analysis of variance
ASCA	Anova simultaneous component analysis
Avg	Average
Anammox	Anaerobic ammonium oxidation
BSIA	Bulk stable isotope analysis
CSIA	Compound-specific isotope analysis
Cys	Cysteine
Dpi	days post infection
EA	Elemental analyzer
EIE	Equilibrium isotope effect
EI	Electron impact ionization
EAA	Essential amino acid
GC-IRMS	Gas-chromatography isotope ratio mass spectrometry
GIRMS	Gas isotope ratio mass spectrometer
Gln	Glutamine
Glx	Glutamic acid and glutamine
Gly	Glycine
His	Histidine
HPLC	High performance liquid chromatography
HRMS	High resolution mass spectrometry
ICP-MS	Inductively coupled plasma mass spectrometer
IRMS	Isotope ratio mass spectrometer
Iso	Isoleucine
KIE	Kinetic isotope effect
LC-IRMS	Liquid chromatography isotope ratio mass spectrometry
Leu	Leucine
LOD	Level of detection
Met	Methionine

MIMS	Membrane inlet quadrupole MS
NEAA	Non-essential amino acid
PGC	Porous graphitic carbon
Phe	Phenylalanine
Pro	Proline
SD	Standard deviation
Ser	Serine
SIA	Stable isotope analysis
TCD	Thermal conductivity detector
Thr	Threonine
TIMS	Thermal ionization mass spectrometer
Tyr	Tyrosine
Val	Valine
VPDB	Vienna Pee Dee Belemnite

9.4 List of publications

2022	Hesse, T., Nachev, M., Khaliq, S., Jochmann, M. A., Franke, F., Scharsack, J. P., Kurtz, J., Sures, B., Schmidt, T. C. (2022). Insights into amino acid fractionation and incorporation by compound-specific carbon isotope analysis of three-spined sticklebacks. *Scientific reports*, *12*(1), 1-11.
2022 (submitted)	Hesse, T., Nachev, M., Khaliq, S., Jochmann, M. A., Franke, F., Scharsack, J. P., Kurtz, J., Sures, B., Schmidt, T. C. (2022). Carbon stable isotope analysis of amino acids and glucose: A new technique to study nutrient flow and conversion in host-parasite systems. *Scientific reports*

9.5 Poster presentations

2020	Hesse, T., Nachev, M., Jochmann, M. A., Schmidt, T. C.: Nutrient flow in a host-parasite system revealed by compound-specific stable isotope analysis of amino acids, *30. Doktorandenseminar*, Hohenroda
2019	Hesse, T., Nachev, M., Franke, F., Scharsack, J. P., Jochmann, M. A., Sures, B., Schmidt, T. C.: Nutrient flow in a host-parasite system by compound-specific stable isotope analysis of amino acids via LC-IRMS, *Isotopes 2019*, Raitenhaslach

9.6 Declaration of scientific contributions

This thesis includes work that was published in cooperation with co-authors. My own contributions are declared in the following:

Chapter 3:

Hesse, T., Nachev, M., Khaliq, S., Jochmann, M. A., Franke, F., Scharsack, J. P., Kurtz, J., Sures, B., Schmidt, T. C. (2022). Insights into amino acid fractionation and incorporation by compound-specific carbon isotope analysis of three-spined sticklebacks. *Scientific reports*, *12*(1), 1-11.

Declaration of own contributions: The experiments were conducted by T. Hesse and S. Khaliq. Data evaluation was performed by T. Hesse and the draft, including corrections to the manuscript, were written by T. Hesse. The manuscript was revised by T. Hesse, M. Nachev, M. A. Jochmann, F. Franke, J. P. Scharsack, J. Kurtz, B. Sures and T. C. Schmidt.

Chapter 4:

Hesse, T., Nachev, M., Khaliq, S., Jochmann, M. A., Franke, F., Scharsack, J. P., Kurtz, J., Sures, B., Schmidt, T. C. (2022). Carbon stable isotope analysis of amino acids and glucose: A new technique to study nutrient flow and conversion in host-parasite systems, Submitted to *Scientific Reports*, 2022.

Declaration of own contributions: The experiments were conducted by T. Hesse and S. Khaliq. Data evaluation was performed by T. Hesse and the draft, including corrections to the manuscript, were written by T. Hesse. The manuscript was revised by T. Hesse, M. Nachev, M. A. Jochmann, F. Franke, J. P. Scharsack, J. Kurtz, B. Sures and T. C. Schmidt.

9.7 Curriculum vitae

Der Lebenslauf wurde in der Online-Fassung aus Datenschutzgründen entfernt.

9.7 Curriculum vitae

Der Lebenslauf wurde in der Online-Fassung ausDatenschutzgründen entfernt.

9.8 Erklärung

Hiermit versichere ich, dass ich die vorliegende Arbeit mit dem Titel:

„The Potential of LC-IRMS: Carbon stable isotope analysis of amino acids in a host-parasite system and a proof-of-principle study for $\delta^{15}N$ measurements of nitrate"

selbst verfasst, keine außer den angegebenen Hilfsmitteln und Quellen benutzt habe, alle wörtlich oder inhaltlich übernommenen Stellen als solche gekennzeichnet sind und die Arbeit in dieser oder ähnlicher Form noch bei keiner anderen Universität eingereicht wurde.

Essen, 23. September 2022

_____

Tobias Hesse

9.9 Danksagung

Mein großer Dank gilt Professor Torsten C. Schmidt für die langjährige Betreuung meiner Promotion, inklusive regelmäßiger Begutachtungen der Teilkapitel, Besprechungen and Anregungen.

Für die Übernahme des Zweitgutachtens sowie die enge Zusammenarbeit möchte ich außerdem Professor Bernd Sures danken.

Besonderer Dank gilt ebenso Dr. Maik A. Jochmann für die fachliche, moralische und praktische Unterstützung bei allen Arbeiten im Labor und am Schreibtisch, sowie der thematischen Erarbeitung meines Promotionsthemas von Anfang bis Ende.

Für die vielen anregenden Diskussionen sowie Hilfestellungen im Labor möchte ich mich bei Daniel, Milen, Klaus, Shaista, Felix, Robert, Lotta, Valentina, Sajjad, Nenad bedanken, sowie bei allen Mitarbeitern der Instrumentellen Analytischen Chemie der Universität Duisburg-Essen für die jahrelange gute Zusammenarbeit vor und während meiner Promotion.

Meiner Lebensgefährtin Elena sowie meiner ganzen Familie und meinen Freunden danke ich herzlichst für die Unterstützung und das Vertrauen während meines kompletten Studiums.